Ultra high vacuum fabrication of metallic contacts for molecular devices on an insulating surface

Shawn Fostner
Department of Physics
McGill University, Montreal
July, 2010

A thesis submitted to McGill University in partial fulfillment of the requirements of the degree of Doctor of Philosophy

© Shawn Fostner 2010

Contents

Abstract xix

Résumé xxi

Statement of originality xxiii

Acknowledgements xxv

1 Introduction 1

1.1 Motivation 1

1.2 Atomic Force Microscopy 3

1.2.1 Cantilever oscillation 4

1.3 Experimental Setup 12

1.3.1 Preparation Chamber 14

1.3.2 Main Chamber 17

1.4 Substrate 19

1.5 Surface pit creation 21

1.6 Sample holder and electrical contacts 22

1.7 Electronics setup 26

1.8 Q-control 27

1.9 Transport 28
1.10 UHV approach mechanism 31

2 Silicon Nanostencils 37
2.1 Background 37
2.2 Design and Fabrication 39
2.3 Heating effects 45
2.4 Stress analysis 48
2.4.1 Staircase structure 53
2.5 Multiple mask alignment and macroscopic electrodes 56
2.6 Wire deposition 60

3 Electromigration 65
3.1 Introduction 65
3.2 Sample preparation and handling 71
3.3 Gold wires 74
3.4 Pd Wires 78
3.5 Tantalum wires 80
3.6 Discussion 84

4 Tip based lithography 89
4.1 Introduction 89
4.2 Electrostatic Modeling 94
4.3 Tip forces during deposition 101
4.4 Tip Fabrication 104
4.4.1 Coated tips 105

4.4.2 FIB tips 107

4.4.3 Electrochemically etched tips 111

4.5 Deposition procedure 115

4.5.1 Gold cluster Deposition 119

4.5.2 KBr surface 131

4.5.3 Metal electrodes 133

4.6 Discussion 135

5 Conclusions and outlook 139

List of Figures

1.1 Schematic image: nanoscale wire deposited by stencil masking, gap created using electromigration and metal-molecule contacts created using field induced tip based deposition. 3

1.2 AFM imaging using a beam bounce detection method 4

1.3 Typical forces during AFM imaging. The net force is shown, with electrostatic, van der waals, and short range chemical components. For plotting, a bond energy of 2.35 eV and a bond length of 3.3 Å is used with the Lennard-Jones chemical potential and a 30 nm radius tip with 1 V applied voltage. 6

1.4 Measured resonant curve for a gold coated Nanosensors NCLR cantilever, 2 nm Ti/100 nm Au. Damped and undamped resonance curves are shown, damped using active Q-control. Q=8100 decreased to 330 after damping, with a shift in resonance frequency of 86 Hz. 8

1.5 Reduced amplitude a vs reduced distance d for multiple tip bias voltages, $Q = 250$, $u = 0.9988$, $k_{Waals} = 6.57 \times 10^{-5}$, $k_{elec} = 3.42 \times 10^{-5}\mathrm{V}^{-2}$, $A_0 = 14nm$ 12

1.6 JEOL 4500A UHV AFM/STM/SEM. The preparation chamber also includes the quartz crystal microbalance, molecule evaporator, cleaving station, and metal evaporator (Oxford Applied Research mini-ebeam evaporator), opposite side not shown. 13

1.7 AFM cantilever holder. The tip contact both holds the cantilever and provides electric contact to the front fact of the cantilever chip, the tip position and piezo element are also indicated. 15

1.8 Sample cleaving sequence for a crystal block in the modified contact holder. (a) The cleaving arm (not shown) applies pressure to the front of the sample, close to but not touching the front of the sample holder, (b) The sample cleaves along a pre-scribed mark, (c-d) Metal contacts are add after the evaporation process, the front face of the sample is unobstructed at this point. 16

1.9 KBr substrate examples, (a,b) Bad and good cleaves, imaged by SEM, (c) FM image of flat cleaved substrate after short SEM exposure, (d) KBr surface after 210s SEM exposure with typical imaging conditions (2kV, low resolution, 80 μA current), (e) Atomic resolution of KBr surface and small atomic pits 20

1.10 SEM deposited pits, in combination with gold clusters nucleated before and after. (a) Atomic resolution of pits on the bare surface, (b) Gold nucleated at pit corners. The pits are either overshadowed by the gold, or simply removed, which case is true is not clear despite multiple attempts to image them. (c) Further pits nucleated after the gold deposition, the gold density is visible lower, and the pairs or triples of gold are almost entirely removed, suggesting the pits nucleated but were pinned by only one cluster, desorbing the other. 23

1.11 (Left: Exploded view of the sample holder, contact electrodes, and contacts, Right: Sample with contacts attached and touching the contacted film 23

1.12 Phase locked loop for cantilever oscillation. (a) FM self oscillation setup, the frequency shift from the PLL detector is sent directly to the JEOL control box and used as the feedback signal (b) AM with Q-control, the detector is used as a signal generator to create the fixed frequency oscillation signal. The drive signal from the controller is used as a phase shifted version of the oscillation signal, which acts as an active damping term, reducing the cantilever Q-factor. 25

1.13 Calculated gold thin film and wire resistivity from surface and grain boundary scattering, mean free path = 40 nm,(a)thin film, (solid) p = 0.008, R = 0.23, (dotted) p = 0.6, R = 0.3 (b) wire, different wire parameters given, $D50$ the mean grain size, adapted from C. Durkan [1] 30

1.14 Original mask approach mechanism. The mask is mounted on a metal piece guided by two stainless steel pins and pressed from behind by a hollow screw. The front of the stencil mount is pressed against a retaining foil, in a recessed hole under the level of the mask, allowing the mask to retract as soon as pressure from the screw is released . . 32

1.15 (a) Piezo walker without sample or mask holder, the two piezo elements and spheres are shown. The magnet is mounted on a set screw, adjusted from below. (b) Similar, but with a mask holder (non-rotating head) and sample holder shown. The indicated electrical contact is one of two, the other opposite and attached to the body for ground return. 33

1.16 Silicon stencil mounted on a vertically rotating front piece. 34

2.1 (a) Schematic of the stencil alignment with a sample possessing two macroscopic contact pads. (b) Broadening of the deposited features due to the geometric limitations of the setup. The thinned membrane (t) is spaced from the sample position by up to a micron typically. (c) Simplified process flow of the stencil fabrication process (d) A sample membrane with 85 nm critical dimension 40

2.2 Damaged silicon stencil. The membrane was damaged during an approach procedure, but the low surface stress prevents it from spontaneously breaking further. (Inset) Schematic, 2 60x5 μm electrodes bridged by a 50-500 nm x 5 μm wire 44

2.3 Heat damaged stencil. (a) Damaged stencil (b) Similar stencil heated under low vacuum for 2.5h at 150 ° C, no observable effects, (Inset) Back side of the stencil, this side faces the evaporant material, but is opposite the side used to FIB the structure 46

2.4 Damaged silicon membrane with spherical nodes shown 47

2.5 Compressive vs tensile surface stress for a deposited film (dark) on a thin substrate 48

2.6 Single stencil features from two different membranes, before (a,c) and after (b,d) the deposition of thick Ta films: 45 nm for (b) and 27 nm (d). 49

2.7 Sample fit for one membrane feature, (a) SEM data, fit region indicated (b) Fitting region with the corrected height ($\sqrt(2)$ for 45 degree image angle), measured points and the circular fit shown 51

2.8 Illustration of the line of sight problem with high membrane thickness to opening size ratios. Plot for 3 different opening sizes at which the incident beam is totally occluded, it will actually begin to block incoming material well before this point. 54

2.9 Alternative stencil structures, bowtie and with an integrated gap. (a,c) Ion image of the milled structure, dark regions correspond to openings in the membrane. Steps in the structure are as described above (b,d) Angled SEM images of the structures. 57

2.10 Stencil mask to TEM grid alignment, schematic. The position of the gap, indicated by the TEM grid beam, is noted on the the alignment jig and used to position FIB array within the acceptable region indicated 59

2.11 Tantalum vs gold wires, 11.5 vs 30 nm thickness 60

2.12 Typical metallic edge for large gold and tantalum electrodes (a) Tantalum edge near the 5 μm wide wire region masked using the silicon stencil, (b) Gold edge masked by the TEM grid 61

2.13 Calculated stencil-sample spacing for 3 different stencils. As the features are recessed from the surface, a minimum spacing of the membrane thickness (1-2, 1.2 and 2 μm for mask 1, 2 and 3 respectively) is expected. Surface diffusion is not taken into account 62

2.14 Deposited wires, all on KBr (dark areas) except (f), on oxidized silicon (a) Contact pad, electrode, wire, electrode, contact pad shown, (b) The same wire as (a) and also as shown in Fig 2.11(left) (inset) AFM image of the same wire, multiple images stitched to cover the full length of the wire, (c-e) Similar examples on different samples, mask used for (e) has an opening 200-1400 nm wide, edge features due to contrast adjustments for visibility, (f) Bow-tie structure evaporated ex-situ on silicon for electromigration, discussed further in chapter 3 63

3.1 Typical electromigration paths. (a) Bamboo-like wire, migration is often transgranular and a single grain is shown for clarity, [2] (b) Polygranular wire, slits tend to follow the grain boundaries [3] (Right) Schematic structures at typical length scales for the gold wires discussed below. 66

3.2 Active feedback controlled electromigration, (a) Electromigration cycles for gold on silicon, time sequence indicated, (b) Pre-migration joule heating of the wire, several cycles shown. Slight increases at the start of each cycle are residual temperature effects that typically relax with a full cycle. (all electromigration data for gold and palladium measured with D. Stoeffler) 70

3.3 Gold wire evaporated on oxidized silicon ex-situ (in a high vacuum evaporator) with no adhesion layer, using a bowtie stencil, (a,b) Images taken using tapping mode AFM in UHV, before and after the first migration cycles, 41 to 105 Ω. Visible mounding on the downstream side of the electronic current is indicated (upper electrode). (c) Histogram of multiple migration curves, with the corrected resistance shown. Peaks in conductance near multiples of the fundamental conductance quantum are smeared out or shifted due to heating and other effects. (d,e) Resistance jumps for migration cycles close to the wire fully breaking, clear jumps between conductance regimes are indicated. 73

3.4 E-beam patterned gold on oxidized silicon, 31 nm thick, (a,b) Before and after migration images by tapping mode AFM, (c,d) Two of the migration cycle sets at with very different resistances are shown (same wire), large fluctuations observed are thought to be variations in the position of metallic clusters. Doubling of features in the vertical direction are a result of a clear double tip, a result of tip changes due to picking up metallic cluster which is a common problem while imaging small metallic features. 76

3.5 Pd wire electromigration (a) Unbroken wire, 35 nm tall, with ridges adjacent to the wire due to the patterning process, (b,c) Broken wire, with the near contact region shown right, arrows indicate the assumed junction points. (d) Final electromigration curves (truncated), with discrete steps showing but well above the quantum limit. 79

3.6 Ta electromigration curves, both show a similar decrease in resistance, (a) UHV deposited sample, high initial resistance leads to larger than usual fluctuations in the resistance (b) Ex-situ Ta wire, resistance spike is not the breaking point, but occurs at a similar voltage to the next break, and is likely the breaking of the first of two parallel wires (not shown) 81

3.7 Ta electromigration samples, (a,b) Before and after SEM images, broad Ta wire broken from the center, width reduced as shown, (c) Wire with perpendicular stress lines, optical image, (d) Double Ta wire imaged at an angle, (e,f) UHV deposited wire before (e) and after complete failure (f) 83

3.8 Freely rotating Ta wire lifted from the substrate but pinned by an AFM tip crash, shown left. 84

4.1 Binding energy curves, (a) Atomic binding energy curves, (b) Ionic and atomic curves for positive ions created at the surface of the tip in the charge exchange model, the cross-over point giving the effective potential barrier to desorption. 91

4.2 (a)Schematic geometry, (b) Model geometry in gmsh, full scale size is 1000 nm with a tip size of 30 or 50 nm. The rectangular void on the left forms the bounds of the electrode pad. (c) Sample 2D mesh near the tip and electrode edge. Three levels of mesh refinement shown (max element size, some are smaller), 100 nm, 5 nm, 0.5 nm (0.25 nm not shown, directly below tip) 97

4.3 Contour plot of the electric field lines for a 2D model of the potential around a circular tip and 10 nm tall electrode (zoom near the tip, simulation area 1 μm across in both directions), -40 V applied to the tip. 98

4.4 Projected electric field magnitudes calculated from a 2D slice of the original potential solution. Maxima are shown at both the edge of the electrode, and the tip apex, which is typical of the geometry. 99

4.5 Barrier heights calculated for 30 or 50 nm diameter tips, 1, 3, 5 or 10 nm from the surface of the edge, 25 nm laterally from the edge. Similar calculations for a 30 nm tip, 20 nm laterally show similar characteristics but with a slightly reduced barrier (0.06-0.15 eV lower). The Au^{1-},Au^{2-},Au^{1+},Au^{2+} states are shown (1m,2m,1p,2p respectively). Lines shown only to readily differentiate the cases, not actual fits. . . 100

4.6 Electrostatic force vs tip sample distance for 30 V applied potential, (a) 10 μm tall tip, with different force contributions shown, (b) force gradient for comparison, with the spring constants and effect tip height at which snap in may occur indicated 102

4.7 (a) Electrostatic forces vs voltage, 6nm lift height, 10 μm tip, (b) Electrostatic forces vs tip height for a 30V potential, apex force is constant at 78 nN and not shown 103

4.8 Gold coated tips with a 100 nm Au coating, all 2 nm Ti adhesion layer, barring (a) (10 nm Ti), tip diameters (nm)(a) 66$\pm$2, (b) 53$\pm$3,(c) 57$\pm$3,(d) 61$\pm$4 105

4.9 Faceted gold coated tips, uncertain (though small) Ti adhesion layer thickness and 100 nm gold layer 106

4.10 Gold coated tips with no titanium layer, 100 nm Au coating 107

4.11 Tip gluing setup. (a) Manganin heating wires (left), cement epoxy setup coating, and cantilever chip shown above the scored glass slide with an attached wire (b) Close up, wire and cantilever lifted off the surface with the original wire orientation shown (dashed line) 108

4.12 Tip milling process for gold wires attached to silicon cantilevers. Trimming stage is not shown, as well as subsequent narrowing stages. . . 109

4.13 Tip etching setup above the perchloric acid solution. The reflection shown appears within 100-200 μm of the surface. 113

4.14 Etched gold wires (a) Optical image of bare etched wire, (b) Etched gold tip attached to commercial silicon cantilever using H20E silver epoxy 115

4.15 Voltage response for 3 typical tips over an InP substrate, estimated tip radii of $<$25 nm, $\approx$ 25-50 nm, or $>$50 nm (after a significant crash or pulse event). The amplitude set point is maintained at 0.95 A_0 and the tip retracted. The fits are a simple quadratic fit to demonstrate the dependence which does deviate from this simple model. 117

4.16 Recorded tip oscillation and pulse voltage for two pulse events, (a) 0.5 nm lift height, 5 ms pulse, (b) 5nm lift, 50 ms pulse. The oscillation amplitude in both cases is approximately 6 nm, with a resonant frequency of 150 983 Hz. The decrease in amplitude during the pulse is typical, though some features are difficult to quantify, such as the random tip amplitude changes after the initial decrease. 118

4.17 Electronics setup for the pulsing process. Pulse events are controlled using labview, with feedback during positioning from the cantilever deflection from the deflection sensor, using the amplitude measurement taken by the PLL. 120

4.18 Sample deposition geometries: (a) InP heterostructure, with a 2D electron gas as the back electrode, (b) KBr substrate, depositing over the KBr surface near the metallic film electrode, (c) over the metallic electrode 121

4.19 Initial tip event (top), with several subsequent depositions. The large hole is 230 nm in diameter and 11 nm deep, with the smaller clusters varying from 19-33 nm wide and 6-7 nm tall. The inital event occurred at a lift bias of 5V, as well as 2 of the subsequent clusters, the second followed at 6V and showed a more symmetric dot. 122

4.20 Dots deposited with a variety of pulse lengths, number of pulses, and voltages (profile direction is indicated by the adjacent arrow). (a) 10 and 15 ms pulses (x25 in each case), (b) 5,4,2,1 ms pulses (x25), (c) column of closely space pulses, 20-22 nm apart, the taller initial pulse is sometimes observed for multiple pulses (d) Pair of depositions at different tip voltages. The central diagonal series of pulses varies the pulse number (5,10,15,25 pulses). 124

4.21 Au clusters deposited using +6V lift, -30V pulse, 25 pulses (profile direction is indicated by the adjacent arrow). Intended spacings of 10 or 20 nm, though there are variations depending on the tip placement (manual placed at each point). Again, some lines show significantly enhanced deposition at the endpoints at the expense of the middle of the line. 126

4.22 Deposition results for the same tip in a series of depositions over several areas (error estimates based on the afm measurements), (a) Cluster size as a function of the pulse length, (b) Cluster size as a function of the number of pulses over the same location 127

4.23 Gold clusters deposited on the same sample using an FM operating mode (same tip as previously), with the lift height based on the z-piezo voltage, pulse number, or pulse length are given. 128

4.24 Subsequent depositions on the same sample after removal to air and reintroduction (new coated tip) with a lifting bias of 3V, which is typically very close to the surface and the threshold for a catastrophic tip failure. 129

4.25 Deposited structures imaged used two strong multi-tips, arrows give the actual direction of deposition (for multiple dots). The post deposition tip images are shown to the right in each case. 130

4.26 Deposited clusters and pits over 2 different KBr samples. Arrows indicate either pit, cluster, or direction of the pulse sequence (rows of 4 or 5 horizontal pulse sequences) where indicated. (top) KBr120, initial deposits, 3 in total, and the subsequent attempts are shown, the tip lift bias was 2V for the initial clusters and as low as 1.5 V for the pits, (bottom) similar uncontrolled pits on KBr118 with no deposition apparent 131

4.27 Gold clusters deposited near the metal film edge or directly over the metal itself (a) 3 depositions near the Tantalum edge, (b) Large deposition over the gold edge, (c) Small deposition on the edge of the gold film, gold also to the right but in a disconnected film, (d) Two separate depositions over a Tantalum film edge, after both the first and second deposition there is a noticeable change in the tip quality, initially improved as demonstrated by the increased stability (reduced streaks) and then worsened with a clear double tip 133

4.28 Major pulse events visible by SEM, (a-f) events over tantalum wires, (g-i) events over the gold film edge, in both (g) and (e) there is visible damage to the tip apex itself with the gold fully peeled away. In both metals the pulse event can range from sharpening the tip to fully destroying it. 136

5.1 Gold and tantalum films (a and b respectively) indented using the lithography mode, JEOL WinSPM software. Inset: line profile, deposited gold film 35 nm thick 140

List of Tables

2.1 B1082 Membrane: Measured radii, corrected film stress (using Eqn 2.4). M08 represents an outlier, while bent these particular beams are nearly straight, flexing instead at a weak point and hence have a large radius of curvature 52

3.1 Summarized electromigration data, temperature given from bulk measurements, expected temperature changes are 5-10 times smaller as the thin film resistivity increases significantly, preparation given as e-beam (lithography), stencil (UHV or ex-situ), $\rho_{bulk} = 2.214$ (Au), 10.54 Pd, 12.2 Ta [4] 85

4.1 Potential drop within one atomic radii of the tip for 30 and 50 nm diameter tips, estimate of the electric field at the tip, both calculated for a -40V potential at the tip. Directions given with respect to electrode edge laterally and surface vertically. 101

Abstract

The preparation and characterization of metallic wires on insulating substrates by a variety of mechanisms has been explored. A multi-scale approach utilizing microfabricated silicon stencil masks, feedback controlled electromigration, and field induced metal cluster deposition in a novel geometry has been explored on potassium bromide (KBr), indium phosphide (InP), and silicon oxide substrates in an ultra-high vacuum environment (UHV).

The initial deposition of gold, and tantalum wires between one hundred nanometers and micrometers in size was performed using reinforced silicon nanostencils. The stencil fabrication was discussed, and an examination of the deformation of the integrated structures under the deposition of highly stressed tantalum films was shown to be significantly smaller than typical structures.

Metallic wires deposited using these stencils as well as electron beam lithography were electrically stressed and the breaking characteristics analyzed. Typical nanometer scale gaps were observed, as well as larger features more commonly found in the breaking of bamboo-like structures in gold wires 100 nm in size or less, particularly with a significant series resistance. These larger gaps are expected to be more applicable for the deposition of subsequent metallic clusters and preparation of molecular devices.

As a step towards connecting the initially deposited wires as well as localized molecules in an a fashion allowing atomic scale imaging by AFM, modelling and experiments of field induced deposition of gold clusters on KBr and InP substrates was carried out. Deposition on InP substrates with a backside 2D electron gas as a counter-electrode demonstrated the feability of this deposition technique in UHV. Subsequent deposi-

tions on or adjacent to metallic pads on the bulk insulating KBr provided a proof of principle of the technique, though some experimental limitations such as large current pulses with the tip in close proximity to the surface are discussed.

Résumé

La préparation et la caractérisation de fils métalliques sur des substrats isolants par une variété de mécanismes a été explorée. Une approche multi-échelle utilisant des masques-stencils microfabriqués de silicium, lélectromigration contrlée par rétroaction, et le dépôt induit par champ en nouvelle géométrie dagrégats métalliques, a été explorée sur des substrats de bromure de potassium (KBr), de phosphure d'indium (InP) et d'oxyde de silicium sous Ultra Haut Vide (UHV).

Le dépôt initial de fils d'or et de tantale entre cent nanomtres et quelques micromtres a été réalisé en utilisant des nanostencils au silicium renforcé. La fabrication des stencils a été discutée, et un examen de la déformation des structures intégrées dans le cas du dépt de couches de tantale sous hautes contraintes a montré quelle était significativement plus petite que pour les structures typiques.

Les fils métalliques déposés l'aide de ces stencils, ainsi que la lithographie par faisceau électronique ont été mis sous contrainte électriquement et les caractéristiques de rupture analysées. Des vides typiques ` léchelle du nanomtre ont été observés, ainsi que des structures communément retrouvées dans la rupture de structure de type bambou dans les fils dor de 100nm et moins, en particulier avec une résistance en série importante. Ces vides plus grands devraient tre plus applicables pour le dépôt par la suite dagrégats métalliques et la préparation de dispositifs moléculaires.

Une étape a été franchie vers la connexion des fils déposés initialement ainsi que de molécules localisées de faon d'une manière permettant d'imagerie atomique échelle par l'AFM, en réalisant un modle et des expériences de dépôt induit par champ dagrégats d'or sur KBr et InP. Le dépôt sur des substrats InP avec derrière un gaz d'électrons 2D comme contre-électrode a démontré la faisabilité de cette technique

de dépôt sous UHV. Des dépôts ultérieurs sur ou à proximité de blocs métalliques sur KBr, isolant de volume, a démontré le principe de la technique, mme si certaines limitations expérimentales telles que de grandes impulsions de courant avec la pointe proximité de la surface sont discutées.

Statement of originality

The author claims the following aspects of the thesis constitute original scholarship and an advancement of knowledge.

The focus of this work is in the fabrication of metallic wires and structures with appropriate size gaps for the preparation of molecular devices. To this end, the research described herein is divided into three areas: stencil fabrication and wire deposition, electromigration to break metallic nanowires, and the deposition of metallic clusters in a variety of geometries for the extension of the aforementioned gaps.

Specific contributions include:

- Fabrication and design of an adjustable mask alignment system using a slip-stick piezo approach mechanism for the JEOL 4500 UHV AFM/STM system. This system allows for the reproducible approach of an arbitrary mask to a sample face with micrometer precision.
- Preparation of reinforced silicon stencil mask. Unlike typical masks fabricated through silicon nitride or silicon-on-insulator (SOI) methods, the membranes possess low residual stress and are protected from stress induced deformation by a stepped reinforcing structure. [5]
- In-situ electromigration of metallic wires with AFM imaging at intervals to monitor the structure (in conjunctions with D. Stoeffler, University of Karlesruhe). This allows a greater picture of the electromigration process as it occurs. Results on tantalum (separately), gold, and palladium wires are presented.
- Electrostatic modeling of a model tip deposition system over a bulk insulator

with a side contact by finite element modeling, used to calculate the deposition thresholds in this new geometry.

- Preparation of sharp gold atomic force microscopy tips using a wet chemical etch process. The etch process is adapted from STM tip process for this geometry, for thin gold wires attached directly to the cantilever using silver epoxy.
- Ultra high vacuum deposition of metallic clusters from atomic force microscope tips on the edge of metallic conducting pads, and over a bulk insulator. Previous experiments have been exclusively over a rear contacted InP sample or silicon oxide surface.

Acknowledgements

I would like to thank the support, encouragement, and technical assistance of the entire group, especially my supervisor Peter Grutter. Without your guidance and encouragement over the years I would never have made it this far.

In particular I have to thank the JEOL subgroup, members past and present. Jeff Mativetsky and Sarah for your suggestions, assistance, and help, even long after you thought you had moved on! Jessica Topple for the fun you bring to the lab and all the help, especially with thesis corrections and comments. Antoni Tekiel for taking over this work from me, and making things happen whether we want to or not!

From the group at large there are too many to acknowledge over the years, for their support, encouragement, suggestions, and equipment help. I must especially thank Mehdi el Ouali and Till Hagedorn for their assistance over the years in all things AFM, especially in the tip etching setup. Most of all though, I have to thank Yoichi Miyahara for numerous suggestions and assistance on the AFM, repairs, the deposition work, electronics setup, and ever other thing which you've done to help keep this system running for us even when we were ready to give up.

Invaluable technical support in sample preparation was given by Robert Gagnon, in both SEM, sample sputtering, and system repairs. Jean Beeren at the University of Sherbrooke was invaluable in the machining and preparation of multiple generations of the silicon nanostencils at the FIB, showing enormous patience over the years.

Of course I can't forget the suppport of my parents and family, always there with encouragement, and support no matter how things were going, and always willing to come to Montreal for any reason! I couldn't have gotten this far without you.

Chapter 1

Introduction

1.1 Motivation

Modern electronics is based almost entirely on the power and flexibility of silicon transistors, developed over the past sixty years into a complex combination of doped silicon channels and metallic interconnects lain down in traces a million times finer than the most detailed spider web. Despite this complexity the silicon based technology on which these transistors are based is rapidly approaching its technical limits. As the critical device dimensions approach the theoretical limits forced upon the system by quantum mechanics, researchers are forced to look for alternatives to silicon transistors. As a result research groups are searching for viable alternatives which can minimize the size and power requirements for the modern transistor and potentially give rise to new applications and ways of thinking.

Molecular electronics offers an alternative to conventional silicon electronics where individual molecules or clusters of molecules are positioned between electrodes to act as individual transistors. This offers a possible solution to many of the difficulties in miniaturizing conventional silicon junctions as single molecules are nanometers in size, with a multitude of possible electronic configurations and nearly endless possibilities in terms of devices. Beyond simple electronic devices, molecular junctions offer the possibility of other applications such as optoelectronic devices [6], and molecular gating of conventional electronic devices for biosensing applications [7].

Over the last decade, prototype devices have been constructed by various research groups that contact either single molecules or groups of molecules and exhibit non-linear current voltage characteristics, much like a modern transistor [8, 9]. The difficulty in these experiments is a lack of reproducibility and poor agreement with theory. Relatively minor changes in the metal molecule contacts can lead to order of magnitude changes in the current voltage characteristics as the molecule to metal distance changes dramatically on an atomic scale [10]. Recent experiments using microfabricated metallic wires and break junctions have begun to close this gap with theory [9], but significantly more work needs to be done in order to understand the nature of current flow in molecular devices and their interplay with the surroundings and contacts.

In order to avoid these problems, a knowledge of the atomic structure of the metallic contacts as well as a chemically pure surface are necessary. The focus of the work in this thesis will be the creation of metallic wires with gaps of variable sizes on insulating surfaces using a combination of techniques such as silicon stencil masks, electromigration of metallic wires, and field-assisted deposition of metallic particles from gold tips. The majority of these experiments have been carried out on potassium bromide (KBr) substrates though indium phosphide and silicon substrates will also be discussed. The goal is to create a gap of sufficiently small size for single molecule measurements in a configuration which is accessible to a variety of imaging techniques in a fully vacuum prepared process.

A description of the techniques involved such as atomic force microscopy (AFM) as well as the experimental apparatus will be followed by a description of the silicon stencils fabricated and used to create in-situ submicron wires. The microfabrication process has been previously described [11] but significant modifications of the silicon stencils will be described which reduce stress induced deformation to maintain the deposited pattern integrity. Following this, electromigration experiments on both stencil fabricated structures and bulk microfabricated wires will be discussed. Finally, the deposition of metallic clusters using field induced desorption from gold coated and solid gold tips will be discussed. The deposition of small metallic clusters onto bulk insulators from a metallic tip has not been demonstrated previously, and modeling results on the electric potential geometry and the desorption barriers will be discussed along with experimental results.

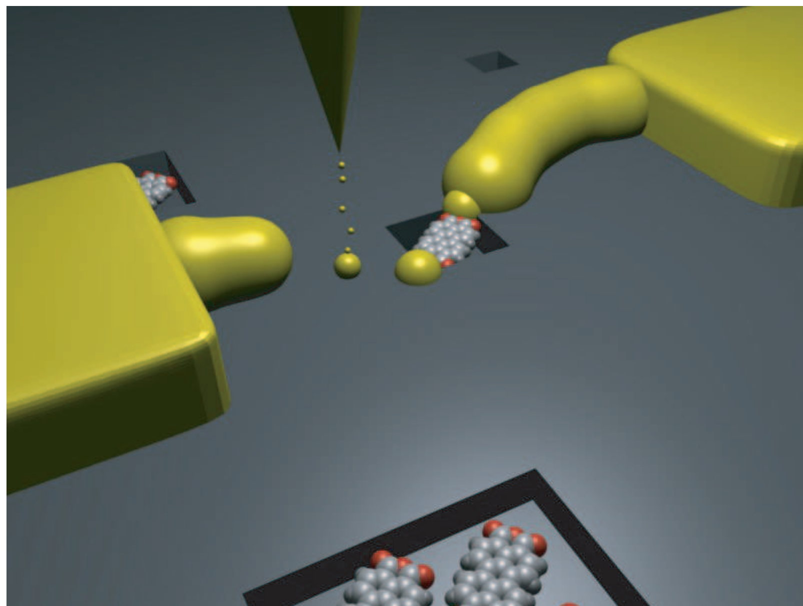

Figure 1.1: Schematic image: nanoscale wire deposited by stencil masking, gap created using electromigration and metal-molecule contacts created using field induced tip based deposition.

1.2 Atomic Force Microscopy

In order to examine metal electrodes in a largely insulating system, one must to be able to obtain atomic resolution on a non-conducting surface, which precludes the use of scanning tunneling microscopy. Atomic force microscopy provides a highly flexible alternative, capable of measuring individual atomic positions or the macroscopic structure of electrodes on a size scale spanning nanometers and hundreds of micrometers. Different imaging modes are possible, and AFM has been demonstrated to work in diverse environments, from liquid to vacuum, and from direct contact with a surface to a tip hundreds of nanometers away.

The technique was first introduced by Binnig, Quate, and Gerber in 1986 [12] and employs a flexible cantilever acting as a force sensor to obtain a map of a surface via the interaction of the tip atoms with the surface. The cantilever is rastered across the surface and the motion of the cantilever is typically observed through optical or piezoelectric methods to give a map of the height of the surface as a function of position as shown in Fig 1.2.

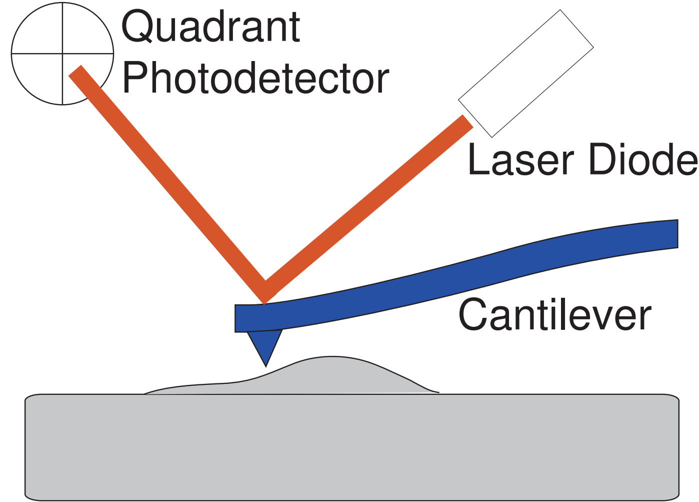

Figure 1.2: AFM imaging using a beam bounce detection method

Direct imaging of a surface can be accomplished by moving the tip over the surface in contact mode and monitoring the cantilever deflection to measure the sample topography. This direct imaging mode suffers from significant noise limitations as well as wear on the cantilever tip. To circumvent these problems, AFM cantilevers are typically lifted off the sample surface and oscillated using a piezoelectric element mounted under the cantilever chip at a small amplitudes, 0.1-100 nm. This dynamic mode can still in fact make contact with the surface during a small part of the oscillation cycle but with minimal wear and significantly increased stability and reduced noise. Non-contact AFM is typically divided into amplitude modulation (AM-AFM) and frequency shift modulation (FM-AFM), the two will be discussed separately as both are used in the measurements given in the following chapters.

1.2.1 Cantilever oscillation

The cantilever oscillation can be described as a driven damped oscillator with additional external forces

$$m\ddot{z} + kz + \gamma_0 \dot{z} = F_{ts} + F \tag{1.1}$$

where the undamped resonant frequency is $w_0 = \sqrt{\frac{k}{m}}$, the Q factor is given by $Q = \frac{\sqrt{mk}}{\gamma_0} = f_0/\Delta f$, Δf is the difference between the free oscillation frequency and current frequency with an applied force F_{ts}, F is the driving force, and m the effective mass of the cantilever. The spring constant of each cantilever differs slightly but is relatively similar for given wafer and batch, and is given by $k = \frac{Ewt^3}{4L^3}$, where E is Youngs modulus for the cantilever and the rest are the physical dimensions. An estimate of these dimensions for a given cantilever can be found by using the SEM to physically measure the dimensions of the cantilever but in practice this is only necessary for force calibrations. The spring constant will vary strongly depending on Youngs modulus.

While retracted from the surface, the tip is driven at its free oscillation frequency with an amplitude of 5-10 nm and re-approached using mechanical step motors. When the tip is close to the surface, within a few nanometers at the lowest point of its oscillation, the various tip sample forces are first felt by the cantilever and tip. As the forces involved cause a change in the cantilever feedback parameter, either the frequency shift or amplitude depending on the mode, the approach is halted. From this point, the tip sample position is controlled by a piezo tube mounted behind the sample position and modified by the feedback loop to maintain the tip height, frequency shift, or amplitude.

Regardless of which dynamic method of AFM is used, there are similar imaging forces involved. The forces responsible for the tip sample interaction have both long and short-range components. The forces relevant for these experiments can be summarized as van der Waals, electrostatic, and chemical. At long range these forces are attractive, with the short range chemical repulsive forces acting only at very small tip sample separation, less than a nm.

Long range dipole interactions give rise to van der Waals forces which are always attractive and are long range. These forces are typically approximated by a sphere and plane approximation and given as

$$F_{vdW} = -\frac{A_H R}{6z^2} \tag{1.2}$$

where R is the tip radius, z the tip sample separation, and A_H is the Hamaker

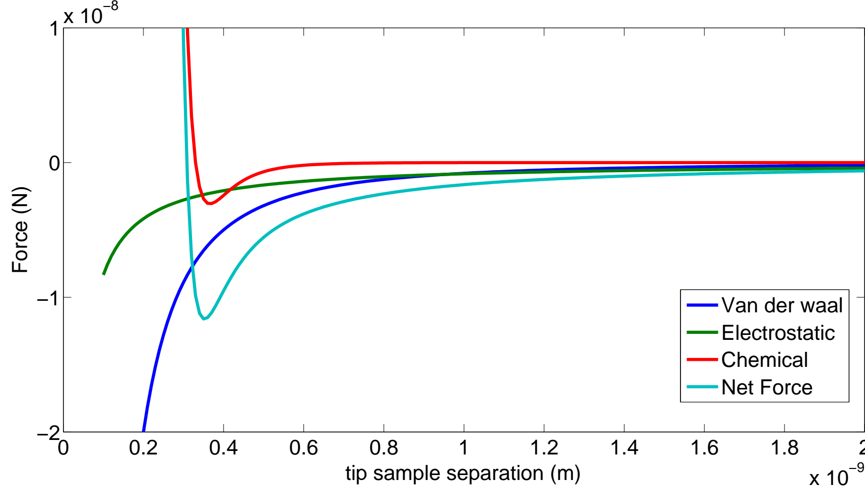

Figure 1.3: Typical forces during AFM imaging. The net force is shown, with electrostatic, van der waals, and short range chemical components. For plotting, a bond energy of 2.35 eV and a bond length of 3.3 Å is used with the Lennard-Jones chemical potential and a 30 nm radius tip with 1 V applied voltage.

constant, a material specific parameter depending on the tip sample geometry and polarizability, typically on the order of 1eV [13]. In situations where the tip sample distance separation is similar to the radius of the tip, contributions from the cone of the tip similar or greater in magnitude to the apex contribution, these have been calculated by Garcia [14].

Electrostatic interactions between the tip and sample are also long range and attractive, and are typically given by

$$F_{el} = -\frac{1}{2}\frac{\partial C}{\partial z}V_{net}^2 \tag{1.3}$$

where C is the tip sample capacitance and $V_{net} = V - \Delta\phi/e$, V the applied potential to the tip, and $\Delta\phi/e$ the contact potential difference (CPD) given by the work function difference between tip and sample. The CPD is typically small, on the order of one volt, it is minimized during imaging by an applied potential between tip and sample. The sphere and plane approximation to this term reduces to

$$F_{el} = -\frac{\pi\epsilon_0 R V_{net}^2}{z} \tag{1.4}$$

in the limit that $R \gg z$ as before. A better approximation of this term will be discussed later in the context of large tip sample biases at moderate distance with metallic coated tips where the contribution from the cantilever and cone become large.

The final tip sample contribution to the forces comes from chemical interactions between the tip and sample and are more difficult to describe. These forces are empirically modeled using either Lennard-Jones or Morse potentials,

$$F_{lennard-jones} = -12\frac{E_{bond}}{\sigma}\left(2\left(\frac{\sigma^7}{z^7}\right) - \left(\frac{\sigma^{13}}{z^{13}}\right)\right) \quad (1.5)$$

$$F_{morse} = -E_{bond}(2\kappa e^{-\kappa(z-\sigma)} - 2\kappa e^{-2\kappa(z-\sigma)}) \quad (1.6)$$

where E_{bond} is the bond energy, κ a decay length, and σ the equilibrium distance. Chemical forces become large and positive at small distances, less than two angstroms roughly, and are attractive at larger distances [13]. It should be noted that unlike macroscopic length scales, the notion of contact is not well defined in this regime. The onset of short range repulsive chemical forces are typically taken as the defining point of tip and surface contact. Surfaces in NC-AFM are generally imaged in the attractive regime, with a tip sample separation greater than distance, 0.5-1 nm or more. If the tip enters the repulsive regime, permanent deformation of the tip or surface may occur.

One limitation of scanning probe microscopy using microcantilevers is the risk of suddenly snapping into contact with the surface. As all but the short range chemical forces above are attractive the cantilever will naturally bend towards the surface in the absence of a restoring force. If the tip sample force, or effective spring constant, exceeds that of the cantilever, $\max|\frac{\partial^2 V_{ts}}{\partial z^2}| > k$, then the tip will snap into contact with the surface. Imaging in the dynamic mode creates a restoring force due to the cantilever oscillation such that stable oscillation is possible if $\max|F_{ts}| < kA_0$ where A_0 is the free oscillation amplitude [13]. For typical oscillation amplitudes of 6 nm and $k = 100N/m$, the maximum dynamic restoring force is 600 nN, much larger than typical imaging forces. However, in the presence of large applied electric fields the maximum force for a tip within nanometers of the surface can be large enough that this assumption is no longer necessarily true, as described in section 4.3.

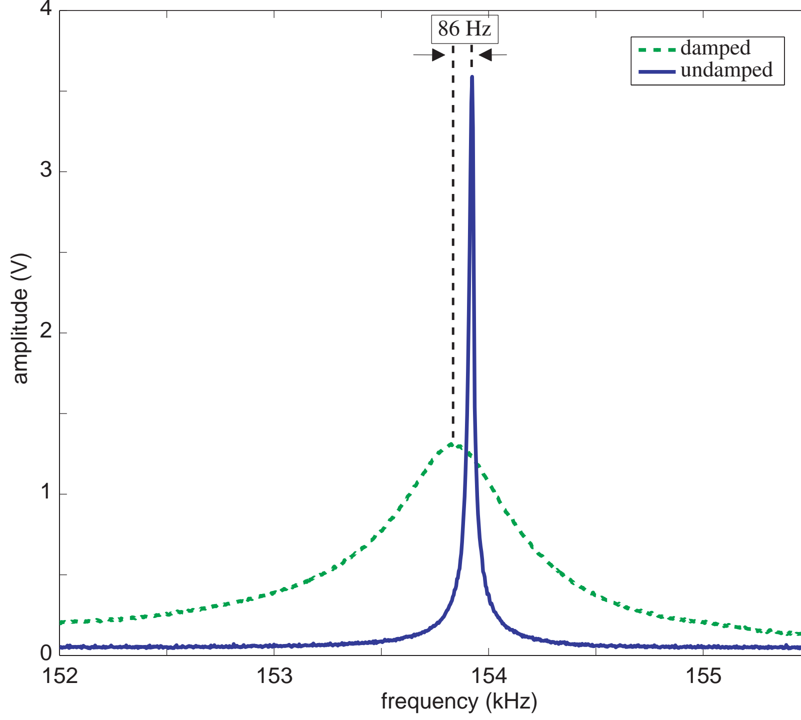

Figure 1.4: Measured resonant curve for a gold coated Nanosensors NCLR cantilever, 2 nm Ti/100 nm Au. Damped and undamped resonance curves are shown, damped using active Q-control. Q=8100 decreased to 330 after damping, with a shift in resonance frequency of 86 Hz.

Frequency modulation, a particular implementation of dynamic mode imaging, was introduced by Albrect and co-workers in 1991 [15] and involves driving the cantilever on its resonant frequency and measuring the shift in resonant frequency from its free oscillation frequency observed as a result of the forces acting on the cantilever. If f_0 is the natural resonant frequency, then $f = f_0 + \Delta f$ is the frequency with an added tip sample force. If the force gradient is constant over the oscillation amplitude, for example under the effect of small amplitudes or weakly varying forces, it can be simply shown that $\Delta f = \frac{f_0}{2k} k_{ts}$ by linearizing the interaction force where k is the cantilever stiffness, and k_{ts} the gradient of the tip sample interaction [13]. For more complicated force gradients or large amplitudes it is necessary to solve the differential equation over the full oscillation period. It has been demonstrated that this can be calculated using

$$\Delta f = \frac{f_0}{2k} \int_{-A}^{A} k_{ts}(z - q') \frac{\sqrt{A^2 - q'^2}}{\pi/2A^2} dq' \tag{1.7}$$

[16] with A the oscillation amplitude.

The zero of the frequency shift is set as the fundamental resonance frequency of the cantilever by self exciting it while far from the surface. The oscillation controller part of phase locked loop (PLL), described in section 1.7, is used to maintain a $\pi/2$ phase shift between the excitation signal to the cantilever and the measured signal from the driving circuit. In practice, with the cantilever close to the substrate surface there are slight temperature changes and creep of the piezo tube. The laser diode can heat the cantilever and surface resulting in thermal expansion. As well, the cantilever can shift in its holder slightly during the approach or measurement, all of which will shift the resonance frequency. In order to have an accurate measurement of the frequency shift it is necessary to retract the cantilever from the surface slightly and re-zero the frequency shift on a periodic basis, however during measurements this can contribute to errors in the frequency shift on the order of 1 Hz.

During scanning, the oscillation amplitude is maintained by the feedback electronics at a set level, known as constant amplitude mode. While this is not strictly necessary for FM-AFM, it allows the measurement of dissipative forces and simplifies the calculation of forces from the measured frequency shift. By monitoring the energy required to maintain the cantilever oscillation per cycle it is also possible to measure non-conservative forces, such as energy lost to molecular motion while imaging molecular clusters loosely bound on a surface, or the deformation of soft surfaces. The origin of dissipative forces is often poorly understood, and it is difficult to distinguish the separate effects due to tip structure changes versus tip surface interactions [17]. Both often appear as instabilities in the tip image or changes in the imaging signal over step edges and mobile surface features.

Frequency shift imaging is highly sensitive and typically non-destructive for both tip and surface, however even under these conditions there is a gradual degradation of the imaging quality over time as the tip apex picks up adsorbates from the surface or the as fine structure of the tip apex is gradually worn down. This is often observed as the development of double tips (doubling of structures in the image as a result of additional humps in the tip), instabilities in the image (streaks or jumps where the tip is incapable of following the surface structure), or greater than usual tip convolution (as the features on the surface appear larger with increasing tip radius). Assuming

long range interactions are properly minimized by eliminating electrostatic forces, it is possible to obtain high resolution images of atomic or molecular structures by taking advantage of the close range chemical forces and operating at small amplitudes and large frequency shifts. Changes in the F_{ts} cause a change in the resonant frequency of the oscillation with a settling time $\tau \approx 1/f_0$ [13]. For the high frequency cantilevers used, 150-300 kHz, this means the effective change in the frequency shift is extremely fast. Operated in vacuum, cantilevers can also achieve extremely high Q-factors, several thousand or higher, which limits the noise of the cantilever and allows for extremely precise measurements, with sensitivities as high as 10 fm/$\sqrt{Hz}$ if thermally limited or closer to 1 pm/$\sqrt{Hz}$ for typical cantilever based systems [13]. A typical resonance curve is shown in Fig 1.4.

Amplitude modulation AFM is the other primary method of non-contact measurement. Instead of maintaining a constant amplitude and tracking the oscillation frequency, the cantilever is oscillated with a constant frequency on or near the natural resonance of the cantilever and the amplitude changes as a result of tip sample forces are monitored. As in FM-AFM, the center of the resonant frequency curve shifts with the applied force, with the amplitude decreasing depending on the magnitude of the shift. The feedback loop attempts to maintain a constant amplitude set point by changing the tip sample distance, and the height gives a measure of surface topography. Amplitude modulation was historically used before the invention of FM-AFM, but it suffers from a significant drawback that makes it much more difficult to use in UHV. The change in amplitude of the cantilever does not respond as quickly as FM-AFM, but rather settles with a time scale $\tau \approx 2Q/f_0$ [13]. As the Q-factor of cantilevers increases significantly in vacuum to the order of thousands, this puts significant limitations on the cantilever and scanning speed, for $Q = 10000$ and $f_0 = 150$ kHz the settling time for an amplitude change is greater than 0.1s, meaning an imaging time of almost 2 hours for a single 256x256 pixel image. As the Q-factor is decreased to several hundred or less, readily possible in liquids or air but more difficult in vacuum, settling times as low as 5 ms or less are readily achieved. Mechanical changes to the cantilever Q-factor are the most direct method for achieving this, but these place severe limitations on the design of the cantilever. A more general approach recently developed [18] is to use electronic Q-control to add an additional damping term to reduce the cantilever Q-factor dynamically. This will be discussed in the experimental methods below.

As with other dynamic imaging modes, it is possible to image using amplitude modulation in either non-contact mode, or contact mode close to the surface. The complex dynamical system created by the tip and interaction forces has regions of stable operation and some with significantly unstable operation. While tip jumps and instabilities are often taken to be contaminants or mobile surface objects, it has been shown that operating either in contact with the surface or certain non-contact ranges are the most stable imaging regimes [19]. Intermittent contact mode imaging, or Tapping Mode ^{TM}(Veeco), is the most common imaging mode, with the tip briefly in repulsive contact with the surface for a very small part of the oscillation cycle. The disadvantage of this approach is there can be large forces on the imaging object, capable of irreversibly destroying small surface features entirely.

The other complication which arises in AM mode imaging is the fact that both the amplitude and phase are coupled to each other and therefore knowledge of both is necessary to extract tip sample forces. This is in contrast to FM mode in which the phase contrast is a measure of non-conservative forces but conservative forces are largely represented by the frequency shift alone [14]. Amplitude modulation imaging can still give a measure of the sample surface but the separation of forces is no longer as clear and must be recovered during post processing.

With the use of sufficiently large amplitudes, stable AM imaging of very tall structures (tens of nanometers or more) can be possible, in a range where FM imaging develops serious stability problems. The theoretical reason for this difference in stability is not understood in general, but has been observed by both this and other groups during FM mode imaging. The principle difficulty is in imaging edge structures with a dramatic change in height, for example the edge of a deposited film, which in FM imaging is often accompanied by a loss of frequency lock in the PLL, tip jumps, and other instabilities, which worsen at smaller tip-sample distances (and hence larger frequency shifts). Amplitude modulation seems less sensitive to these effects, with fewer jumps and has the ability to stably image structures as tall as hundreds of nanometers with a tip amplitude of 5-10 nm.

The amplitude dependence as a function of the applied force has been calculated by Aime and coworkers[20, 21]. In particular, the force as a function of voltage and

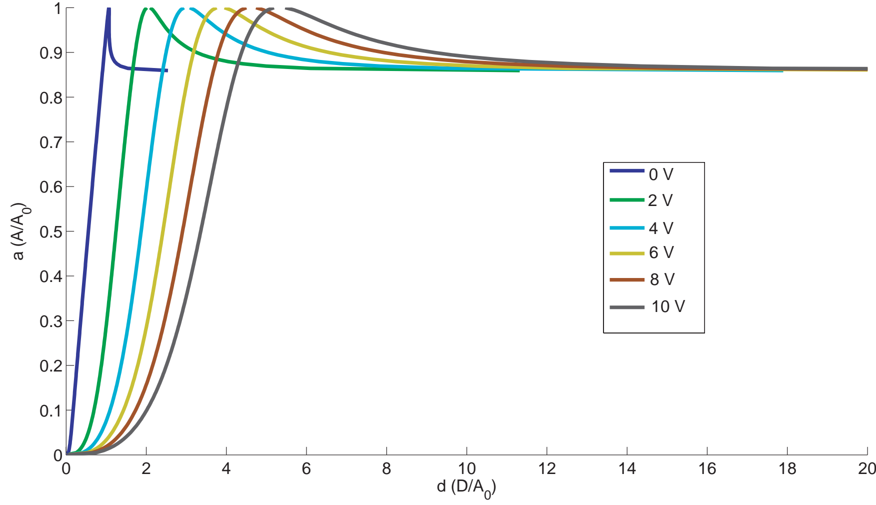

Figure 1.5: Reduced amplitude a vs reduced distance d for multiple tip bias voltages, $Q = 250$, $u = 0.9988$, $k_{Waals} = 6.57 \times 10^{-5}$, $k_{elec} = 3.42 \times 10^{-5}\mathrm{V}^{-2}$, $A_0 = 14nm$

distance is given by Dianoux and colleagues [22] using a variational method to give

$$d_{A\pm} = \sqrt{a^2 + \left(2\frac{k_{Waals} + k_{elec}V_{net}^2}{(1-u^2) \mp \frac{1}{Q}\sqrt{\frac{1}{a^2} - u^2}}\right)^{2/3}} \tag{1.8}$$

$$\phi_{A\pm} = atan\left(\frac{u}{Q(u^2-1) + 2Q\frac{k_{Waals}+k_{elec}V_{net}^2}{(d_{A\pm}^2 - a^2)^{3/2}}}\right) \tag{1.9}$$

[22] where $d_{A\pm} = D/A_0$, D is the tip sample distance, $a = A/A_0$ is the reduced amplitude, $\phi_{A\pm}$ the phase, $u = f/f_0$ is the reduced oscillation frequency, $k_{Waals} = HR/6kA_0^3$ is related to the van der Waals force, $k_{elec}V_{net}^2 = (\epsilon_0 S/2kA_0^3)V_{net}^2$ is related to the electrostatic force, S the effective area of the tip in a parallel plate approximation. An example of the amplitude dependence is given in Fig 1.5.

1.3 Experimental Setup

The system in use for these experiments is a JEOL UHV 4500A AFM-STM-SEM. Experiments have also been carried out to understand the growth characteristics of molecules and small metal clusters on NaCl and KBr in preparation for depositing

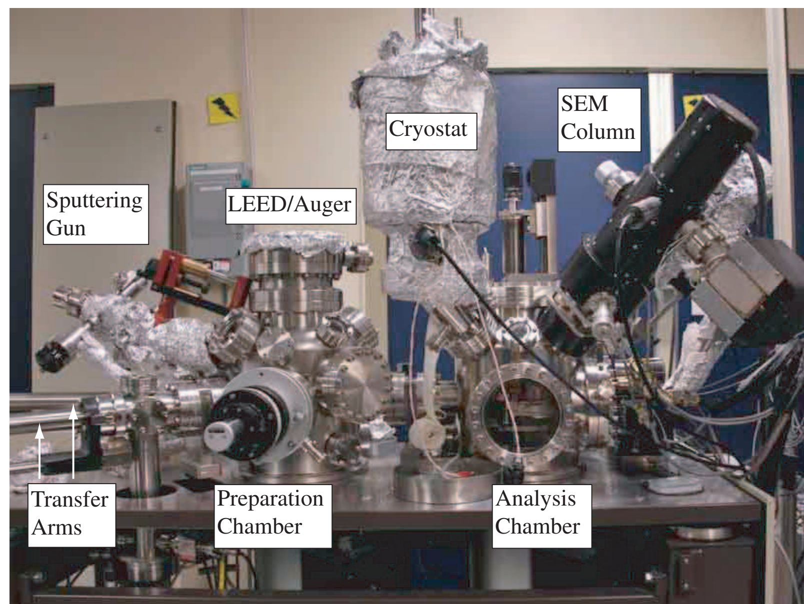

Figure 1.6: JEOL 4500A UHV AFM/STM/SEM. The preparation chamber also includes the quartz crystal microbalance, molecule evaporator, cleaving station, and metal evaporator (Oxford Applied Research mini-ebeam evaporator), opposite side not shown.

electrodes [23, 24, 25].

The system has a series of two chambers, shown in Fig 1.6, as well as a loadlock for quickly introducing samples and tips to vacuum, typical pumping times are 15-30 minutes. Both chambers are pumped using a separate combined ion pump and titanium sublimation pump with a turbo and roughing pump backing the loadlock and used for pumping the entire system after venting. The base pressure of the main chamber is 2-3 x 10^{-8} Pa, and 1-2 x 10^{-8} Pa for the preparation chamber, measured using hot filament ion gauges. Samples are introduced by venting the loadlock to atmosphere, and pumping down with the turbo pump for at least 30 minutes or longer to reach a pressure of 5 x 10^{-6} Pa at most. Pumping times of one to two hours can produce pressures in the low 10^{-7} Pa range when open to the prep chamber if the absolute pressure is critical. The chambers are separated by a series of pneumatic valves between the loadlock and preparation chamber, and between the preparation chamber and main chamber. Internal access to either chamber is controlled by means of a magnetically coupled rotating linear transfer arm with a spring clip and pin to mate with the parent holders for samples and tips or for customized tools, as discussed

later. The transfer arms intersect at the turntable in the preparation chamber which has four positions for holding sample or tips, three of which have electrical contacts. The AFM cantilever holder is shown in Fig 1.7. The tip is held at a 16° angle relative to the sample face and driven by a piezo element located under the chip. The STM tip holder differs in that the tip is held normal to the sample with no oscillation capability. The AFM tip holder is capable of applying a voltage to the tip through a clip isolated from the rest of the stage, separate from the voltage applied to oscillate the tip piezo element.

Samples and tips are transferred between chambers using the internal transfer arm, then moved into position on the front of the piezotube via an elevator mechanism. The elevator uses a small pin to lift the sample or tip holder and linearly position it in front of the piezo or on the stage respectively, mating with the hole shown on the top of the tip holder.

In order to image objects on an atomic scale it is necessary to have excellent vibrational stability. To this end, the microscope is located in the midst of a low vibration area housing the SEM cluster in the basement of the Wong building. The microscope itself is mounted on a vibration damping air table, with the stage mounted on a series of springs inside the system as well.

1.3.1 Preparation Chamber

The preparation chamber contains a number of deposition, characterization, and other sample preparation tools. The available tools are: Ar sputtering gun, LEED/Auger, quartz crystal microbalance, molecule evaporator, metal evaporator, and sample cleaving station. The Ar sputtering gun allows for sample cleaning and material removal though is not used for KBr samples which are soft and susceptible to both ionic and physical sputtering damage.

The LEED/Auger is a low energy electron diffraction and auger electron spectroscopy device (SPECS) which can be used for looking at crystal structure and elemental composition over a small area. As this work deals primarily with insulating materials it is difficult to accurately use LEED as the electron beam can cause significant charging and damage which obscures the crystal structure analysis.

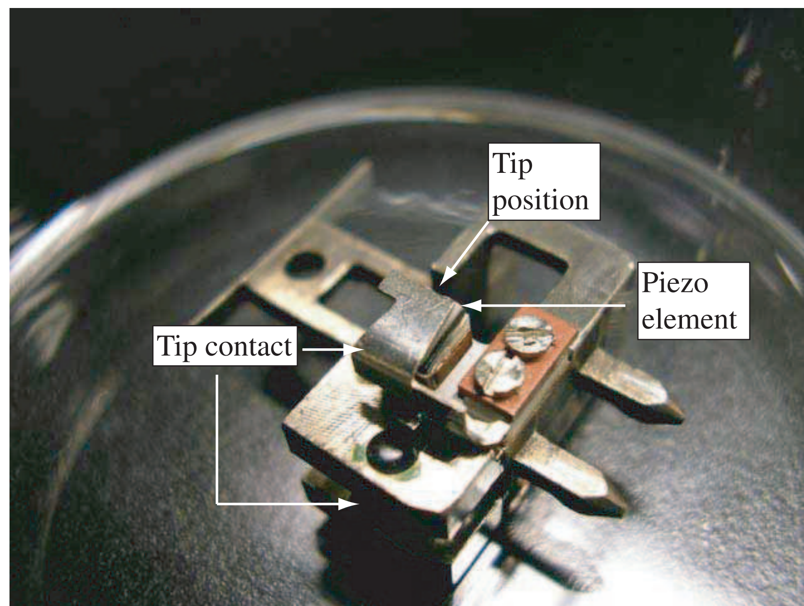

Figure 1.7: AFM cantilever holder. The tip contact both holds the cantilever and provides electric contact to the front fact of the cantilever chip, the tip position and piezo element are also indicated.

The quartz crystal microbalance (Inficon) is positioned on a movable bellows and can be placed in front of the sample position at an angle to calibrate the deposition rate of either the molecule or metal evaporators based on the mass deposited on the surface and the input density. As the crystal blocks the evaporation of material to the sample position, it is necessary to retract the sample in order to measure the rate during deposition. During evaporation of metals, the rate is measured immediately prior to starting evaporation, and then repeated at several hour intervals during evaporation.

The two evaporators installed on the system both possess active water cooling during evaporation. The molecule evaporator (Kentax TCE-BSC) contains three separately cooled quartz pockets each capable of thermally evaporating different molecules at a fixed temperature. The evaporator possesses a shutter such that any individual pocket or combination of pockets can be opened or closed as desired. The rate is set by the evaporation temperature which is controlled by an electronic feedback unit as well as the source to sample separation.

The metal evaporator is a mini electron beam evaporator (Oxford Applied Research).

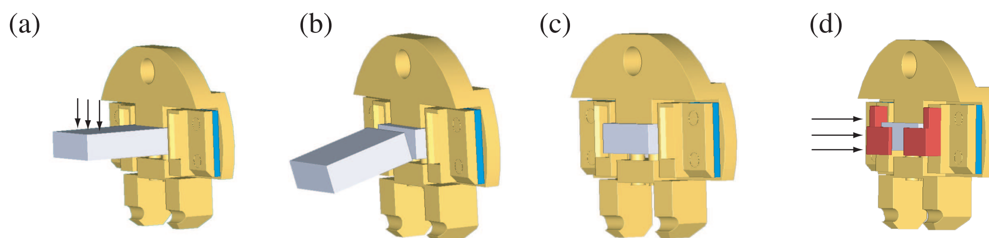

Figure 1.8: Sample cleaving sequence for a crystal block in the modified contact holder. (a) The cleaving arm (not shown) applies pressure to the front of the sample, close to but not touching the front of the sample holder, (b) The sample cleaves along a pre-scribed mark, (c-d) Metal contacts are add after the evaporation process, the front face of the sample is unobstructed at this point.

There are 4 separate pockets, but each pocket contains a single metal rod or crucible with a nearby tungsten filament. The filament accelerates thermal electrons to the target through a 2 keV bias voltage, causing significantly heating the target and increasing the vapor pressure and causing evaporation from the tip of the rod, or crucible. The evaporated material passes through a collimating opening, a collection grid for ion current measurement, and a charge suppression grid also held at 2kV which focuses and filters the beam of residual charged ions and electrons, ideally allowing only neutral species to reach the sample. The rate is controlled by the applied current to the filament and monitored by the ion current at the grids in conjunction with the quartz microbalance. High melting point materials like Ta and Pt can be used in rod form, lower melting point metals such as gold are placed in a crucible to avoid flowing out of the crucible as melting occurs. For the experiments described below, gold in a molybdenum crucible or tantalum rods were used as evaporation sources. A complication during the evaporation of tantalum was that the filaments had a limited lifespan, typically on the order of several evaporation cycles. It is thought that some of the tantalum material is deposited onto the tungsten filament itself and due to the extremely high melting point, remains there. This reduced the filament resistance over time, thus requiring higher and higher currents to reach the same evaporation temperature and power. As the current supply to the evaporator is limited to 5.5 A, this eventually results in filament ceasing to function. Some success was had by directly heating the filaments at up to 6 A without the high voltage, thereby thinning them and allowing evaporation again but this also shortens the lifespan of the filaments, causing them to break completely after several attempts.

The sample cleaving station is a simple block which can apply force to the top of a protruding sample. This allows one to create a clean surface in UHV from an externally prepared sample. For samples prepared ex-situ, it is possible to cleave the KBr block in air using a razor. The sample is first scribed in air using a razor blade to define the breaking plane, then snapped off by applying force to the top of the sample (in UHV or air) or directly cleaved using the razor and a hammer. The sample quality depends on how well the original block is oriented and secured, the quality of the initial scribe, and the presence of any cracks or imperfections in the block. Following cleaving the sample is heated by a custom heating holder at 1.6 A for 1 hour, reaching a temperature of 150° C to remove any residual charge due to the cleaving process as well as adsorbed water. The samples are radiatively heated by a tungsten filament located directly behind the sample position in a modified holder[1].

1.3.2 Main Chamber

The main chamber is used for imaging with AFM, STM, and SEM. Samples are transferred to clips in front of the piezo scanner where they can be accessed by scanning probe tips, a low power optical telescope, or scanning electron microscopy (SEM). As well, the main chamber contains a low temperature cryostat for cooling samples to 30 K using liquid helium or 90-100 K using liquid nitrogen.

The SPM tips are mounted in front of the sample on a retractable stage with the laser diode and quadrant photodetector also located inside the vacuum chamber. The stage is mechanically controlled with a motorized approach mechanism and is capable of up to 400 μm travel in each direction, whereas the laser diode and mirror are positioned by hand using mechanical feed throughs. Only the AFM capabilities will be discussed here, though in principle the STM mode is implemented similarly.

The piezo tube on which the sample is mounted controls the tip sample separation as well as the lateral position of the tip during scanning motion, with a maximum 1.4 μm Z range normal to the sample face and 5 μm X and Y motion in plane, limited in practice to 4 μm in each direction. The piezo element on the tip holder oscillates the cantilever at its resonant frequency as described above. To approach the

[1]Designed by R. Hoffman and fabricated at the University of Basel

sample the mechanical step motors move the cantilever to within the z-piezo range of the surface, stopping when the feedback set point is reached. If approaching in FM mode, as the tip sample interaction increases close to the sample the frequency shift will become negative, decreasing until the approach set point at which point the mechanical approach stops. All further motion is controlled by the piezo tube by adjusting the frequency shift or amplitude set point in software. Oscillation of the cantilever is monitored by the reflection of the laser off the back of the cantilever onto a quadrant photodetector. The motion of the cantilever, vertically or torsionally, registers as differing signals in the detector, A-B for normal motion with C-D for lateral motion. In order to reduce back reflection induced noise into the cantilever diode, a common problem leading to mode-hopping noise in the laser signal, the system was modified in October 2009 to drive the laser directly using a Thorlabs LDC 201C ultra low noise laser diode controller coupled to an RF modulator (VCO Mini-Circuits POS-400) through a bias-T (PBTC-1GW) to the laser diode in the system. The RF modulation of the laser power prevents the laser from lasing in a single mode, and hence eliminates noise due to mode hopping from back reflections on the cantilever. This is particularly important in the case of metal coated films where large reflections can be possible from the sample surface and significantly increased noise was visible. The controller is operated in constant current mode, with 1-2 mW output power, which can cause temperature drift issues with the laser power changing by a factor of two as it warms up. It also prevents the system from overly stressing the diode while maintaining constant power in the event of a failure in the laser feedback loop.

Commercially available cantilevers, Nanosensors NCLR PPP, are used with resonant frequencies from 150 - 300 kHz and tip radii of 10 nm or less. Further discussion of the tips used, both conventional and metal coated can be found in Chapter 4.

The main chamber also houses the SEM column. The SEM scans a focused beam of electrons across the sample and collects the secondary electrons at a fixed position detector. The SEM is focused on the sample position and is capable of 50-200000X magnification, with a resolution down to 10 nm under optimal conditions. The accelerating voltage is 0.5 - 12 kV, though typically an accelerating voltage of 10 kV is used for most applications with conducting samples and 2kV for insulators such as KBr, with a current of less than 100 uA. The principle usage of the SEM in-situ is to

examine cantilevers tips, position the tips relative to the surface, check the position of the sample contacts, and monitor the electrical connectivity of the sample. In this work, it is also used to examine metal films on KBr. Like the LEED, while in principle it is necessary to look at conducting surfaces with the SEM, in practice one can examine even insulating surfaces with minimal charging effects. The SEM column is isolated from the the main chamber when not in use by a valve and pumped by a separate ion pump at the rear of the chamber. The buildup of charge on insulating samples is potentially avoidable if the accelerating voltage is appropriately controlled. Most surfaces possess a lower voltage range between which the build up of charge is significantly suppressed as the surface develops a small positive charge and then reaches equilibrium. This voltage is typically on the order of several kV and imaging of insulating materials is readily possible at these points, with the upper voltage increasing significantly for angled samples such as that observed in our system (45 degrees with respect to the sample normal both vertically and horizontally) [26]. While this lower limit is not known for KBr, the lower limit is often on the order of several hundred volts, and little charging to no charging is experimentally observed on KBr for accelerating voltages of 2 kV with reasonable imaging resolution.

1.4 Substrate

Potassium Bromide (KBr) is an ionic crystal with a lattice constant of 6.60 Å and a cubic crystal structure like that of Sodium Chloride (NaCl) (5.64 Å). Samples are prepared from a transparent single crystal block, which is cleaved in air to form a sample of the appropriate size along the (100) direction.

Pre-cleaved pieces of KBr are scribed in air then cleaved in UHV using the in-situ cleaving station described previously [11, 24]. This provides a pristine substrate surface with a well controlled position, given by the initial scribe mark.

The alignment of the scribe on the surface which helps guide the cleave is critical, if the cleave is significantly misaligned with the (100) direction then the surface will cleave with a large number of micrometer size steps in a jagged staircase across the surface, shown in Fig 1.9(a). For typical molecular measurements one only requires small areas, a few micrometers across at a time, to be flat and free of steps. However, for

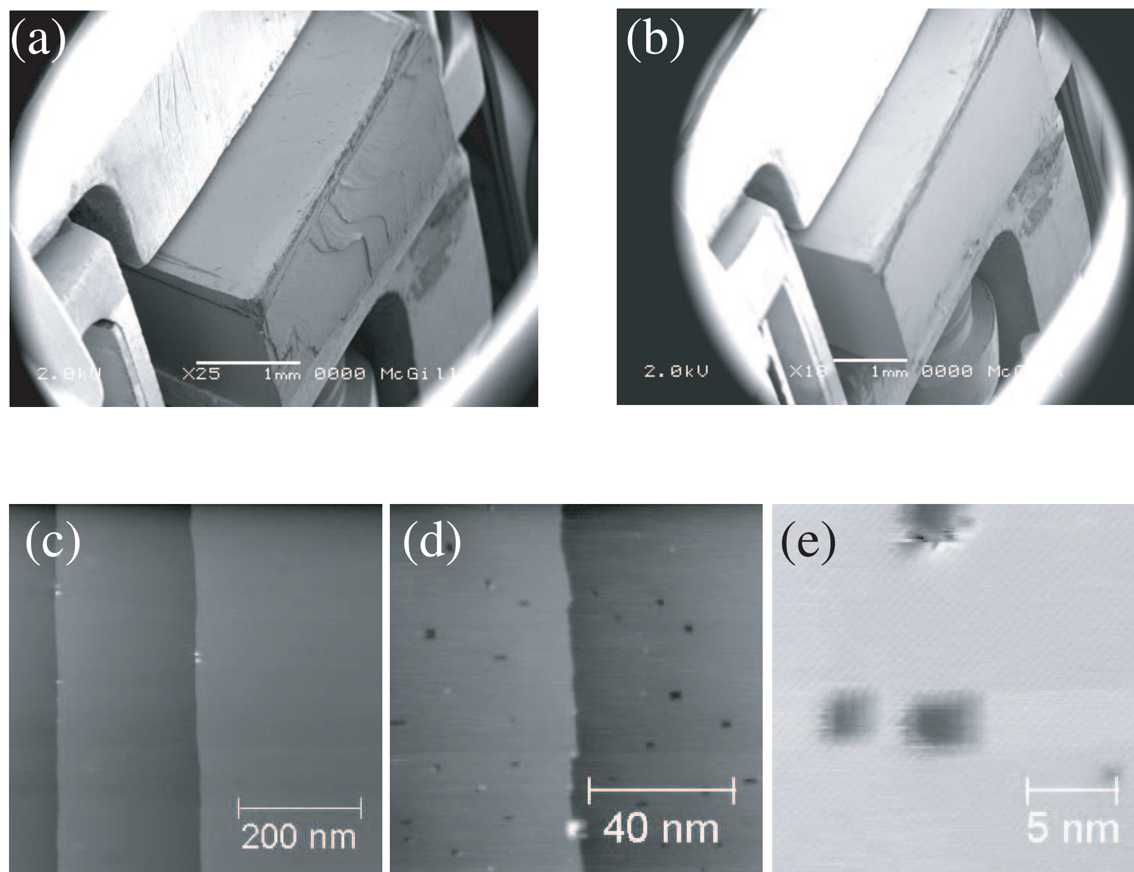

Figure 1.9: KBr substrate examples, (a,b) Bad and good cleaves, imaged by SEM, (c) FM image of flat cleaved substrate after short SEM exposure, (d) KBr surface after 210s SEM exposure with typical imaging conditions (2kV, low resolution, 80 μA current), (e) Atomic resolution of KBr surface and small atomic pits

the deposition of metallic films and wires it is necessary to have a sample surface which is flat (free of significant global rather than local steps) on the order of millimeters. To achieve this, samples are cleaved, examined by eye for gross imperfections, then observed using the SEM for steps which are typically invisible by eye due to the transparent nature of the substrate, an example of the typical surfaces is shown in Fig 1.9. The deposition of charge on the KBr surface while imaging with the SEM, even at lower accelerating voltages, is similar to the charge induced creation of atomic scale pits using the e-beam evaporator described in [27, 23]. Pits created at room temperature by the SEM are more irregular and have a larger size distribution, but are similar in size and depth to those created by e-beam. With sufficiently short exposure to the SEM the surface remains relatively free of defects and no observable pits are created, similar to the 30s exposure in Fig 1.9(c). As the dose or imaging time are increased, larger pits are observed over the surface, shown in (d). High resolution AFM images reveal the pits to be single atomic layer deep in all cases with a <100> orientation as expected.

When properly prepared the sample surface can have atomically flat terraces which extend for micrometers and are separated by atomic steps 3.3 Å tall. Both atomic and molecular resolution have also been demonstrated simultaneously on the KBr substrate [24]. This gives an ideal surface to prepare electrodes and wires with minimal thickness that remain electrically continuous. A simple method to check this continuity after attaching the sample electrodes is to apply a moderate bias to each side of the sample and observe the SEM contrast. The contrast will vary from light to dark depending on the applied bias if properly connected. This method is not usable if there are deposited and fully connected wires, as the applied bias can be sufficient to electromigrate the wires as described in Chapter 3 and destroy them prematurely.

1.5 Surface pit creation

A necessary intermediate step between the formation of gaps in metallic wires and the measurement of single molecule transport is the ability to trap the molecules between the metallic leads. The typical approach for planar configurations is to deposit large numbers of molecules which possess end groups with a strong affinity

to the metal electrodes and hope that only a single molecule bridges the gap [9]. The difficulty in this approach is that the molecular positions are impossible to image, sometimes falling as they do deep into a trench less than an nanometer wide between two electrodes tens of nanometers tall.

As an alternative, localizing deposited molecules in a pit on the surface, with metal clusters self assembled at the pit corners was previously demonstrated [28]. Given that the pit size is tunable [27], the number of molecules and the electrode spacing can be controlled, and more importantly it allows both the electrodes and molecule to be imaged by AFM.

This same technique can be used to potentially create similar pits using the SEM in arbitrary locations on the surface of the sample, but more importantly these pits will tend to nucleate near the positions of deposited metal clusters if the metal clusters are deposited first, shown in Fig 1.10. This gives tremendous flexibility in terms of the order of deposition. One complication however, as shown in Fig 1.10(c) is that some of the gold clusters appear to have been removed, the density of gold clusters changed from $0.0026 \pm 0.0003/\mathrm{nm}^2$ to $0.0016 \pm 0.0004/\mathrm{nm}^2$. For pinned gold clusters, such as those deposited in an anchored line this should not be a significant problem. The pits shown are also relatively mobile, imaging at frequency shifts as low as 8-10 Hz was sufficient to significantly destroy or badly deform pits, particularly those smaller than 10 nm square.

As the SEM is frequently used to examine the sample during cluster deposition, described in Chapter 4, to align the tip or look for sample connectivity, a number of small pits are typically created all over the surface. The only ones of interest however are those nucleated between metallic electrodes and as described above they are often pinned by the local metal structures.

1.6 Sample holder and electrical contacts

There are several different sample holder types available within the UHV system, designed for either flat samples approximately 7 mm long and less than one mm thick, or crystalline blocks up to 2 mm thick which are cleaved in situ. The cleaving

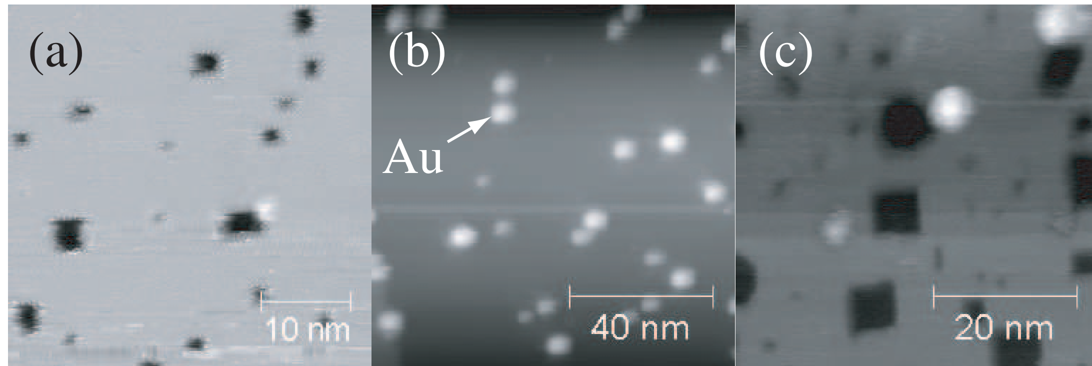

Figure 1.10: SEM deposited pits, in combination with gold clusters nucleated before and after. (a) Atomic resolution of pits on the bare surface, (b) Gold nucleated at pit corners. The pits are either overshadowed by the gold, or simply removed, which case is true is not clear despite multiple attempts to image them. (c) Further pits nucleated after the gold deposition, the gold density is visible lower, and the pairs or triples of gold are almost entirely removed, suggesting the pits nucleated but were pinned by only one cluster, desorbing the other.

holder designed to mount the latter is entirely metal, with two set screws below the sample. The holder allows vacuum cleaving of the KBr blocks as described above. The disadvantage with this holder is that it is impossible to make any form of electrical connection through the clips that hold the sample holder to the system. An adapted sample holder was designed and machined as described previously [11], with an exploded view of the holder and an SEM image of clips on a metal coated sample are shown in Fig 1.11.

As conductance measurements of the deposited wires are required, the metallic clips

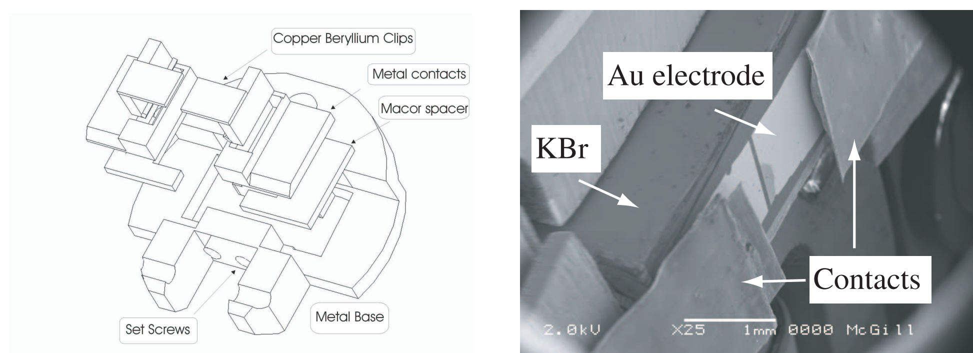

Figure 1.11: (Left: Exploded view of the sample holder, contact electrodes, and contacts, Right: Sample with contacts attached and touching the contacted film

must be insulated from the body of the holder unless the bulk of the sample holder is constructed out of a non-conducting material. Since a significant amount of force is applied to the sample during cleaving a metal base is required, with an insulating layer between the clips and body. The assembly is held together using H77, a vacuum compatible, insulating, high temperature epoxy (Epotek). The glue is used to bond the base piece to the metallic clip holders. The metal clips used to connect the sample holder and deposited electrodes are machined of either copper beryllium or stainless steel foils. These provide the contact between both the sample face and the metallic side contacts, and are then connected to the external feedthroughs via thin coaxial cables.

As the sample is cleaved in vacuum the clips must be attached without removing the sample holder to prevent contamination. The clips are locked into the sample holder from the front and apply a small amount of force to the metallic film. The contact foils are mounted on stainless steel plates which are pressed between two bent foils to apply a retaining force which is perpendicular to the face of the sample. This prevents the need for excessive force in attaching the sample contacts as the electrode and underlying substrate are readily damaged.

An alternative form of contacting the sample face was also used prior to the contacts described above. Prior to putting the uncleaved KBr sample into the vacuum system, a metal spring clip was gently pressed into both sides of the sample using a one millimeter set screw and coated with silver epoxy up to just below the level of the sample scribe. When evaporating the electrode pads, the sample was rotated $\approx 30°$ to the normal such that the edge and side of the sample were also contacted, forming a continuous film up and over the $90°$ corner edge of the cleave and across the sample face. The difficulty with this method is that the angled deposition exaggerates any gap between sample and stencil, the contact over the edge of the sample was often poor, and line of sight issues make the process much more difficult to achieve a fully connected electrode without significantly thicker depositions.

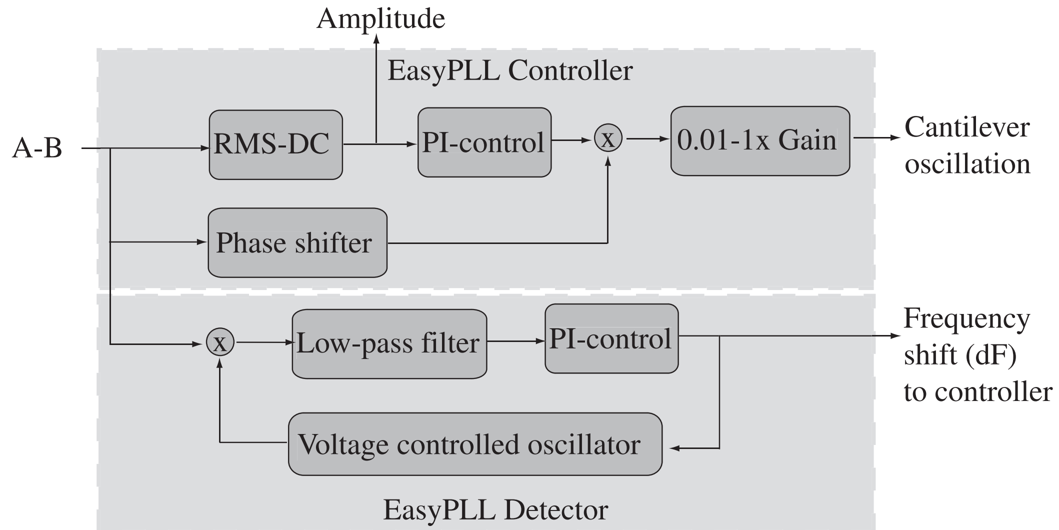

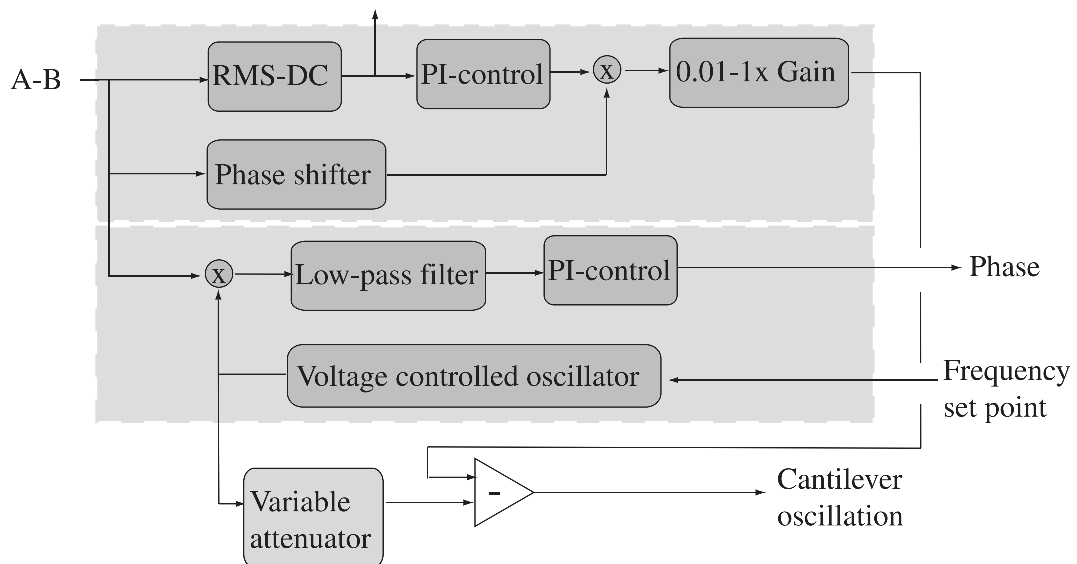

Figure 1.12: Phase locked loop for cantilever oscillation. (a) FM self oscillation setup, the frequency shift from the PLL detector is sent directly to the JEOL control box and used as the feedback signal (b) AM with Q-control, the detector is used as a signal generator to create the fixed frequency oscillation signal. The drive signal from the controller is used as a phase shifted version of the oscillation signal, which acts as an active damping term, reducing the cantilever Q-factor.

1.7 Electronics setup

Frequency modulation imaging is performed in a self-excitation mode, with the deflection signal from the cantilever monitored and fed back into the excitation piezo amplified and phase shifted.

Feedback is controlled using a NanoSurf EasyPLL to monitor the frequency shift and output a proportional voltage, as well as maintain a constant amplitude and phase shift with respect to the detection signal as shown in Fig 1.12. To measure the frequency shift an internal oscillation is multiplied with measured oscillation, the resulting sum component of the oscillation is filtered out by the low pass filter, leaving only a signal $V \propto \sin((\omega_{in} - \omega_{ref})t + \phi_{in} - Phaseshift)/K$ where K is the sensitivity, and ϕ_{in} the phase shift of the input signal relative to some reference, and in and ref refer to the measured and internal oscillations respectively. The PLL will adjust the frequency of the internal oscillator until the output voltage is zero, assuming the phases are the same as would be the case for the self excitation scenario. It is also possible to use the voltage controlled oscillator as the driving signal to the cantilever (not shown), but this will not be discussed here. The JEOL electronics receive the output of the PLL as a feedback voltage and adjust the z-piezo extension to maintain a constant frequency shift while imaging.

All images are saved as 16 bit TIFF files with the header information containing the data parameters such as scan size, position, feedback parameters, and z-scale in a JEOL specific format.

Control of the measurement process is primarily determined through setting of the gain, feedback filters, scan speed, and frequency shift set point, all controlled in software and communicated to the JEOL electronics (the black box). Additional voltages can be added to the piezo tube through the black box via an internal 15x gain amplifier, with an input range of $\pm 10V$. The tip voltage can be accessed through a shielded coaxial cable internal to the system which passes through a feed through. Outside of the system the tip connection is either used for current measurement, as in the STM case through a linear and log preamplifier, or for voltage measurements through an unshielded cable which will be discussed further in section 4.5.

For external control of the various voltages a computer running Labview 6 with 2

National Instruments 6036E DAQ cards and associated breakout boxes are used. Each card has two 16 bit analog outputs and 16 analog inputs, with the analog outputs used to control the X, Y, and Z voltages on the piezo as well as the tip voltage.

1.8 Q-control

To implement amplitude modulation as discussed previously, it is necessary to damp the cantilever Q-factor electronically. This approach was first suggested by Sulchek and colleagues [18] and has been implemented in this group previously to use in this system in situations where FM mode imaging is too unstable, typically for imaging tall molecular crystals [25], or tall metal films such as those deposited here.

The basis of the approach is easily understood in the context of the basic driving equation 1.1, and specifically the damping term $\gamma_0 \dot{z}$. This damping is typically a complex mixture of both internal loss mechanisms in the cantilever and damping forces experienced by the tip close to the surface. The addition of another velocity dependent term to the equation will result in a modified damping of the cantilever, and an effective decrease in the Q-factor. As the tip oscillation is usually a relatively clean sinusoidal oscillation, it is clear that the addition of a simple $\pi/2$ phase shifted version of the measured signal to the cantilever oscillation is equivalent to this velocity dependence, corrected for additional phase shift due to the electronics.

In practice, as shown in Fig 1.12(b), the two terms are comprised of the measured oscillation from the cantilever, used as the damping term, and the direct constant frequency oscillation from the internal voltage controlled oscillator. An example of a damped oscillation is shown in Fig 1.4, with the Q-factor decreased from 8100 to 330. As the cantilevers are clamped using foil spring clip, Fig 1.11, in some cases the resonance curve is not as clear with occasional small side-bands on the main peak. This can cause a problem, as the original resonant peak sharply decreases in amplitude while other nearby peaks are not affected by the damping process. In many cases this limits the effective Q-factor to between 500-1000.

The signals are subtracted from one another, with the appropriate inversion to ac-

count for any additional phase shifts, using a Stanford Research Systems low noise preamplifier (SR560) with an integrated 1-300 kHz bandpass filter. Control over the damping of the signal is achieved by gain on the preamplifier and the amplitude of the damping term set by the controller gain and set point. The overall amplitude of the oscillation is controlled independent of the damping using a resistive variable attenuator to control the output of the set frequency component used to drive the signal.

1.9 Transport

In preparing and manipulating nanoscale wires and contacts it becomes necessary to deal with a number of distinct conductance regimes, macrocopic, mesoscopic, and nanoscale, each of which can have very different behaviors. These regimes have been discussed by a number of different authors [29, 1, 30] and only the basic considerations will be dealt with here as they pertain to the experiments described below.

At macroscopic length scales, where all dimensions are on the order of several micrometers or more, transport in wires and films is well described by Ohm's law in most cases. Ohm's law states that the applied voltage is proportional to the current with a proportionality constant $R = \rho l/A$ where l and A are the length and cross-section of the wire and ρ a material specific resistivity. The origin of this resistivity requires more thought, clearly electrons do not accelerate indefinitely under the applied field. The simple classical Drude model suggests that electrons will accelerate for some characteristic time τ before scattering events, resetting velocity and direction with each collision. This then suggests a current density $\vec{J} = \sigma\vec{E}$, $\sigma = ne^2\tau/m$ where n is the electrons per unit volume, m the effective mass, and $\sigma = 1/\rho$ is the conductivity [30]. As the temperature increases the number of collisions will increase, increasing the resistivity of the material. The collisions are a result of two primary effects, collisions of the conduction electrons with defects or impurities, or scattering off lattice vibrations (phonon scattering). The former is roughly constant at all temperatures, and the latter roughly linear above 100K, the temperatures of interest here, giving a resistivity (or resistance) change of $\frac{\Delta R}{R_0} = \alpha\Delta T$, where R_0 is the reference resistance, α the constant of proportionality which is material dependent but typically about

0.003 K^{-1} for the metals used herein [4]. As the voltage is increased over a small wire, the increase in power dissipation causes an increase of the temperature and hence the local resistance. For most macroscopic wires the effect is minimal but for wires with length scales on the order of micrometer or less the effect can become significant.

As one or more of the dimensions of a wire or film are reduced to the scale of the mean free path, the simple Drude model begins to break down, and scattering effects from grain boundaries and surfaces dominate over defect or phonon scattering. For metals such as gold, these effects begin to be noticeable with sizes on the order of 100 nm or less. The increase in resistivity as the film thickness decreases is partly attributed to surface scattering effects and was calculated by Fuchs [31] and later Sondheimer [32] for thin films and wires of various cross-sections using Boltzmanns transport equation (Fuchs-Sondheimer model or F-S). As the film dimensions approach that of the grain size there is additional scattering due to electron reflection at grain boundaries, which was explained by Mayadas and Shatzkes (M-S theory) [33]. The presence of a grain boundary can be thought of as a missing layer of atoms, with the tunneling barrier between the two regions significantly decreased by image potentials between the two, this will be further discussed in a similar context in Chapter 4. Grain sizes tend to decrease with film thickness, leading to larger film resistivity due to grain boundary scattering. Gold in particular has a large reflection coefficient at both grain boundaries (R = 0.4-0.9), and surfaces (p = 0.5) which magnifies this effect as the constrained dimension decreases in size[1].

Further decreasing the lateral dimensions of wires or films below 100 nm, resistivity begins to deviates slightly from both these models. This was explained by Durkan [34] by using a log-normal distribution of the grain size rather than the typical gaussian distribution assumed previously. Calculations of resistivity vs film thickness and width are given in Fig 1.13 for comparison [1], in rough agreement with typical thin film measured values [35].

This resistance regime is still largely classical, even grain boundaries are essentially scattering centers though the effect on the electron path is estimated quantum mechanically with WKB scattering calculations. Down to this level it is still relatively clear what is meant by a concept of resistance but as the contact areas shrink even

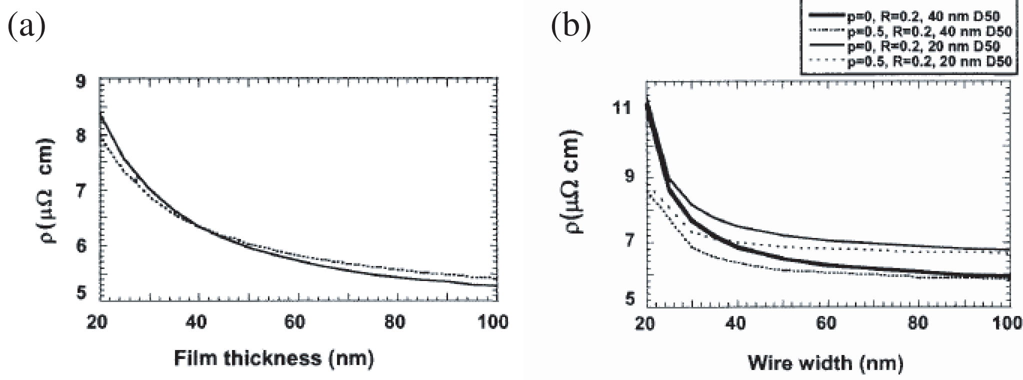

Figure 1.13: Calculated gold thin film and wire resistivity from surface and grain boundary scattering, mean free path = 40 nm,(a)thin film, (solid) p = 0.008, R = 0.23, (dotted) p = 0.6, R = 0.3 (b) wire, different wire parameters given, $D50$ the mean grain size, adapted from C. Durkan [1]

further, to the level of a few atom contacts, it becomes less clear. Electrons traveling through the solid can be described in terms of plane wave states and the transport becomes ballistic in nature.

Unlike macroscopic solids, as the physical dimensions of wires decrease a particle in a box-like confinement leads to a quantization of the energy levels instead of a continuous band structure. This means that there are only particular channels through which the electronic transmission is possible, though even these are smeared out at higher temperatures. Transmission through the conductor can be calculated using a Landauer-Buttiker formalism [29], where the conductor is assumed to be a 1D wire with a number of transmission channels (M) is given by the physical width. Only electrons between the chemical potential of the input and output leads, μ_1 to μ_2 are considered. The conductance and current is calculated by considering the flow of electrons from one lead to the next, assuming a transmission probability T by

$$I_1^+ = (2e/h)M[\mu_1 - \mu_2] \tag{1.10}$$

$$I_2^+ = (2e/h)MT[\mu_1 - \mu_2] \tag{1.11}$$

$$I_1^- = (2e/h)M(1-T)[\mu_1 - \mu_2] \tag{1.12}$$

$$I = I_1^+ - I_1^- = I_2^+ \tag{1.13}$$

$$G = \frac{2e^2}{h}MT \tag{1.14}$$

[29] where 1 and 2 refer to the left and right lead, assuming a current flow from left to right, and $\pm$ refer to right and left currents respectively. The prefactor $\frac{2e^2}{h} = 12.9k\Omega^{-1}$ is known as the conductance quantum (G_0). Despite the simplicity of this model and the potential complications in calculating the transmission matrix T, a wealth of physical systems have been found that demonstrate discrete conductance quanta, from point contacts in metals [36], 2D semiconductor channels pinched off electronically [37], to electromigrated wires imaged in real time by TEM [38]. Mechanical break junctions using gold tips retracted from metal surfaces have clearly demonstrated conductance quantization as low as 1 G_0 with real time TEM images of single gold atom chains [39]. The presence of a single ballistic conductance channel has been shown to demonstrate quantized conductance, but the complex geometry of atomic scale contacts can give rise to a wide variety of observed conductances both higher and lower than this as will be discussed.

1.10 UHV approach mechanism

In this section the creation of a flexible mask holder with a linear translation mechanism and a removable sample and mask will be described. The stencil alignment and attachment is performed ex-situ on the mask holder, between depositions the sample can be removed and stored elsewhere in the system as the mask is exchanged. Alignment to the sample is ensured by two degrees of rotational freedom in the mask translation stage and a pre-alignment of the stencil features with respect to the sample.

In order to achieve an accurate representation of the stencil openings with the deposited features, the stencil and surface must be consistently brought into close proximity to avoid a geometric broadening of the structures described in Chapter 2. In general the simplest approach is to perform a direct mechanical contact, but the need to couple this mechanical approach mechanism into the UHV system complicates the situation. A variety of approach mechanisms were attempted: direct mechanical approach using the linear transfer arm that makes up the sample transfer system into the chamber, using a screw in combination with two retaining guides to push the sample into place with a spring loaded foil to retract the sample afterwards (Fig

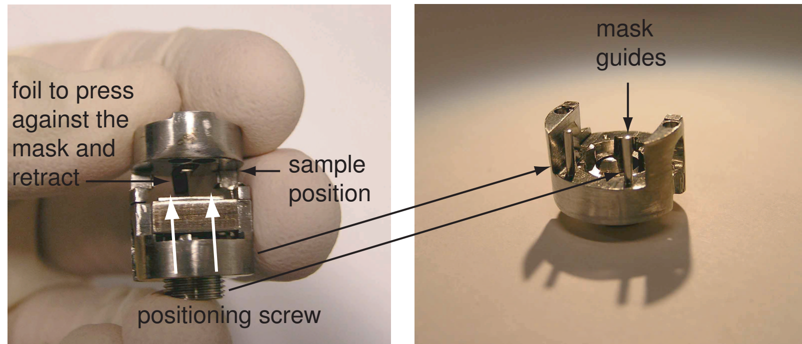

Figure 1.14: Original mask approach mechanism. The mask is mounted on a metal piece guided by two stainless steel pins and pressed from behind by a hollow screw. The front of the stencil mount is pressed against a retaining foil, in a recessed hole under the level of the mask, allowing the mask to retract as soon as pressure from the screw is released

1.14), and a slip-stick piezo walker system resting under the mask holder (Fig 1.15). The direct mechanical approaches suffer from a lack of repeatability and occasionally severe damage to the mask. While physically more robust than thin silicon nitride membranes, the silicon membranes are still several micrometers thick and hard contact with the sample is sufficient to crack the membrane or put large holes in it. The poor force sensitivity of this approach also makes it very difficult to judge the exact approach distance of the sample and mask.

To circumvent these problems, a system using thin piezo elements was used. The piezo stack is glued directly to the body of the holder using a conducting epoxy, with the top surface connected directly to the external contact. On top of the piezo stacks are 1.41 mm tall truncated 2 mm sapphire spheres held in place using Torr-seal high vacuum epoxy. These act as the contact point to the moveable holder. A high voltage, typically 160 V, is applied to the top of the piezo stack with a 10 kHz sawtooth voltage. The piezo elements extend simultaneously in one direction, longitudinally along the surface, carrying the top movable element with it. Upon reaching the sharp step function of the voltage pulse the piezo elements retract, but at sufficiently high speeds such that there is insufficient kinetic friction and the top element remains roughly in place due to inertia. The piezo elements used are 1mm thick Lead Zirconate Titanate EBL2 from EBL Products, with a shear constant of 584 pm/V. For a single layer stack as used here, with 160 V, the piezo extension is roughly 93 nm/cycle. In practice this is not typically achieved as friction between the

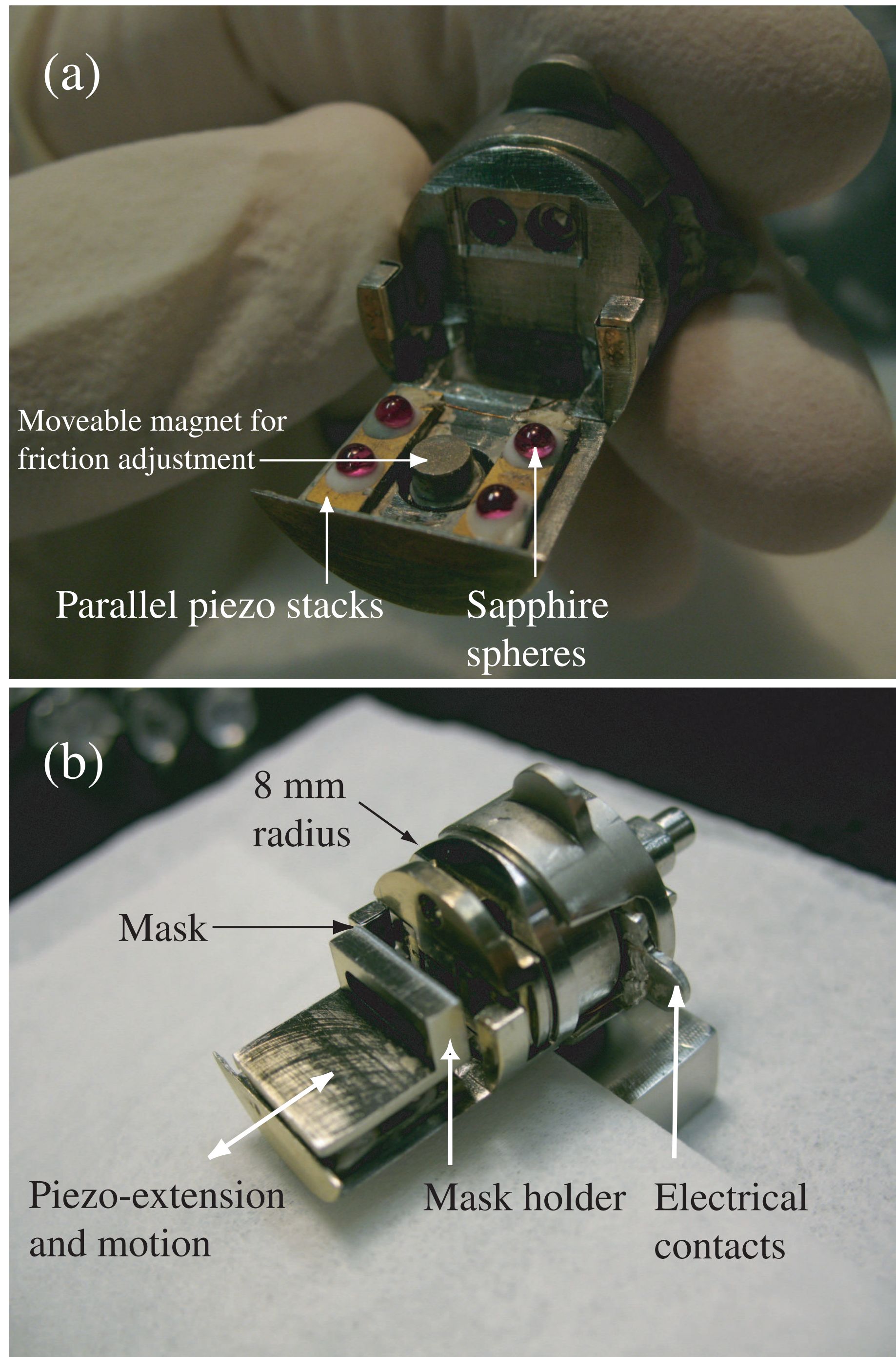

Figure 1.15: (a) Piezo walker without sample or mask holder, the two piezo elements and spheres are shown. The magnet is mounted on a set screw, adjusted from below. (b) Similar, but with a mask holder (non-rotating head) and sample holder shown. The indicated electrical contact is one of two, the other opposite and attached to the body for ground return.

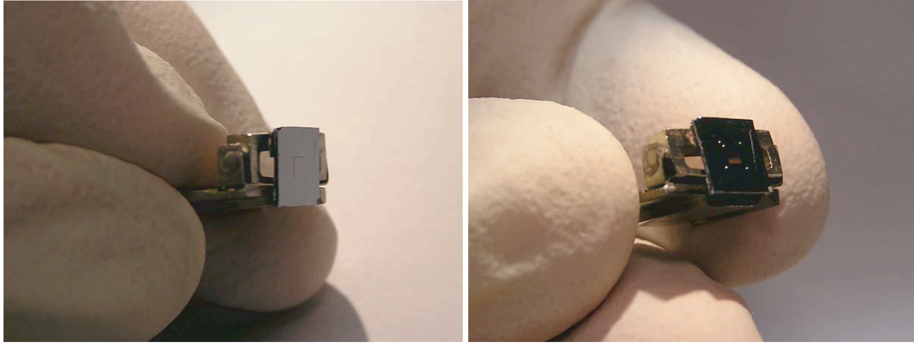

Figure 1.16: Silicon stencil mounted on a vertically rotating front piece.

holder and sapphire spheres varies. Assuming the maximum motion, this translates into approximately 0.93 mm/s, which is a similar order of magnitude to that observed, as typical approach times are on the order of two seconds for a few millimeters travel.

In order to control the frictional force between the sphere and the mask holding piece, the mask holder is constructed from magnetic stainless steel, 17-4, and a small magnet is mounted on the apex of a screw between and underneath the piezo elements as shown in Fig 1.15. The spheres are used rather than a flat surface to constrain the motion of the system and to reduce the contact area to facilitate the slip stick motion of the system. One pair of the spheres are confined in a V-groove, with the other 2 contacting a simple plane. It should be noted that this arrangement was chosen to maximize stability, the length of the range of motion is otherwise limited by the fact that the magnet pulls down on the system in the center and if there is only one sphere plane contact also in the center then at the limit of the forward motion the piece tends to tip forward. This means that the system is overconstrained, in the ideal case only 2 spheres should lie in the groove plus one under the plane giving 5 constraints but leaving the motion free along one direction. As a result it is actually possible to have some rotation in the plane which is advantageous, giving freedom for the mask to align with the sample face more freely.

In order to ensure the mask comes into good contact over the entire surface area of the sample face, it is necessary to allow the mask to rotate both horizontally, as mentioned above, and vertically. To accommodate this the mask holder is coupled to the mask using a small metallic piece held by two dowel pins, with a weak contact between them, shown in Fig 1.16. This allows the mask to self align with the sample

face, which may not be perfectly vertical depending on the position of the sample before the initial cleave, the motivation for this method is loosely based on previous work by Linklater [40] in which the authors approached stencils to a surface using a rotating maskholder with a spring contact, both aligned by hand prior to placing samples in vacuum.

Chapter 2

Silicon Nanostencils

2.1 Background

In order to make nanoscale contacts to molecular devices, a method is needed to be able to prepare submicron metallic contacts on an insulating surface. As these experiments are conducted under UHV conditions, this provides additional constraints samples, the mechanism of preparing samples, and measuring the deposited contacts and wires.

Maintaining an uncontaminated surface is significantly simpler in UHV, with a typical base pressure of $3 \cdot 10^{-8}$ Pa surfaces can remain uncontaminated for more than a week, however this requires all preparation, manipulation and deposition to occur in UHV without removing the sample. This constraint thus necessitates the use of techniques at a combination of length scales, bridging the microscopic position of the individual molecule to the macroscopic external contacts and feedthroughs by which the system is monitored. The mask approach mechanism and sample contacts described in Chapter 1 form the basis for this approach, from external spring clips, to thin metal films with a 60 μm gap, to stencil deposited features with submicrometer wires, to nanometer leads to individual molecules. The description of the stencils used to fabricate the submicron scale wires and the integration of stress relief mechanisms to maintain these structures is described in this chapter.

A secondary consideration is which potential metals can be used as electrodes for growth on the KBr substrate. The monolayer growth of various metals was previously established by J. Mativetsky for this system [23, 41], which looked at the growth of gold, palladium, and tantalum on the surface of KBr. All three were chosen for different reasons, gold as it is easily contacted in molecular measurements through the use of thiolated endgroups on molecules [8] and has been well studied theoretically, palladium for its ability to form good ohmic contacts and potentially have a tunable work function through hydrogen adsorption [42], and tantalum for its similarity in lattice constant to that of KBr (3.3 Å for Ta, vs 6.6 Å for the unit cell) in the hopes of epitaxial growth. While tantalum forms clearly flatter films than either other case, there are other difficulties which will be discussed with reference to electromigration in Chapter 3. Palladium has the unusual effect that it diffuses into the KBr surface, forming substrate islands, making it unacceptable for wire or contact growth [41]. Gold forms relatively large grains, and is highly mobile on the surface, yet has been the most readily deposited and has been well studied theoretically in transport theory. The deposition characteristics of both tantalum and gold will be discussed below.

Typical approaches to depositing wires with cross-sections near or under 100 nm are lithographically based, which of necessity requires the use of dry and wet multi-stage patterning and etchants. Silicon samples prepared in this fashion can be transferred to UHV for characterization though there is a risk of residual contamination. The alkali halide substrates which are described in this thesis are prepared in vacuum, both to avoid this contamination and due to an incompatibility with wet chemical processing.

There are several other deposition based approaches that are compatible with entirely UHV prepared samples, such as self assembled nanowires, and electric field deposition from metallic tips. The latter approach, using metallic tips for wire and cluster deposition will be discussed in chapter 4. Self assembled nanowire growth can also be a powerful method for the creation of crystallographically aligned nanowires, but for the KBr substrates discussed here, there are no known metallic nanowire growth methods, the substrate interaction with most metals is too weak to act as a significant catalyst or guide for directed nanowire growth.

Deposition techniques using micromachined nanostencils have been in development

for over 10 years. Parallel efforts have been undertaken in the electronics industry to develop large area stencils for lithography, in particular ion projection lithography [43], but these will not be discussed here as the requirements are significantly different. In the research community the majority of the focus has been on developing nanostencils to smaller sizes for use in depositing electrical contacts and wires, quantum dots, and molecular clusters. For these purposes a wide variety of techniques and systems have been developed, primarily to control the size and position of features on surfaces in vacuum. Stencils have been constructed from thin silicon nitride, silicon, silicon on oxide, and bulk silicon membranes. These techniques can be divided into two broad categories in general: static and dynamic. Static stencil depositions typically use a mask system in contact or close proximity with the substrate, relying on the initial placement of the stencil to ensure the pattern match with previous or subsequent features on the surface. Several examples of this technique use silicon nitride membranes [44, 45, 46, 47, 48] or silicon on insulator [49]. Some of the concerns related to this technique will be discussed in the following sections, but the primary issues are achieving close proximity to the surface, alignment of the features, and pattern clogging over the lifespan of the stencil. Dynamic stencil depositions are more varied, but typically rely on mechanical or piezoelectric motion of either the substrate or stencil, in order to raster a fixed pattern across the surface. As a result, all patterns on the surface will be exposed simultaneously, but the mobility of the stencil allows for even very simple openings such as a circular aperture in the membrane to be turned into very complex structures. It also allows for the parallel deposition of multiple structures, a key requirement if stencil deposition is to have any use beyond the research laboratory. Stencils constructed in the backs or tips of conventional afm cantilevers [50, 51] also allow for imaging of the deposited structures with no significant movement of the substrate. Dynamic stencil masks have also been demonstrated with the ability to move the entire membrane or substrate rather than a cantilever [52, 53].

2.2 Design and Fabrication

The basic design and microfabrication of the silicon membranes used in these silicon stencils was described previously [11], but the essential features will be reviewed here,

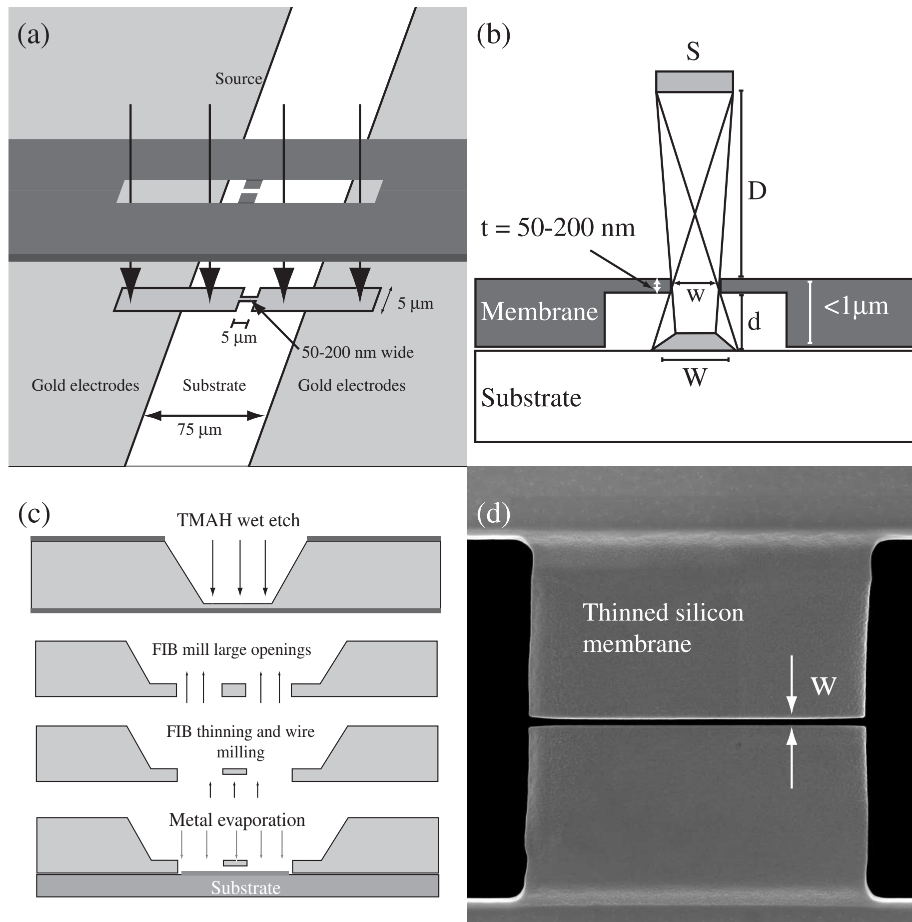

Figure 2.1: (a) Schematic of the stencil alignment with a sample possessing two macroscopic contact pads. (b) Broadening of the deposited features due to the geometric limitations of the setup. The thinned membrane (t) is spaced from the sample position by up to a micron typically. (c) Simplified process flow of the stencil fabrication process (d) A sample membrane with 85 nm critical dimension

and changes from the original design discussed. The previous work dealt primarily with the membrane fabrication process, some preliminary work using the focused ion beam, and other silicon structures which are not mentioned in this thesis.

The membranes are fabricated from N type, 1-10 Ω-cm, double side polished 6 inch silicon wafers with a thickness of 610-640 μm. The wafers are first thermally oxidized in a wet ambient to 5000 Å. An EVG 620 aligner and SiteCoat Spin-Coater are used for patterning and exposure. The wafers are etched in 25% tetramethylammonium hydroxide (TMAH) at 85° C to create the back side openings for the membranes using either 1.5 mm or 2 mm openings along the (110) wafer directions, which give membranes 750 μm or 1.25 mm wide, with slight variations depending on the precise ratio of (111) to (100) etch rates for a given solution. In order to control the membrane thickness, a simple timed etch is used. It should be noted that various etch stop techniques are viable methods of halting the silicon etch and controlling the membrane thickness more accurately but in practice are either unnecessary or undesirable here, often requiring heavy doping of the silicon surface resulting an increased residual stress introduced into the membrane. As well, the thickness control of direct wet etching is sufficient to within several micrometers, with subsequent thinning as described below. The wafers are initially dipped in 10% HF for 30 s to remove any environmental oxide, then etched immediately in TMAH for 2.5 hours. The etch depth is then carefully measured using a profilometer in multiple points across each wafer to assess the exact solution etch rate. A final etch time is calculated based on the measured wafer thickness. Wafers are removed at that point and checked by eye, and if neccessary re-etched for short periods.

As the surface area of the KBr surface is considerably larger than that of the membrane, typically 3.5 mm by 1.5 mm, one concern during approach is that the maximum contact area between the sample and membrane be achieved. If for example the sample face is tilted slightly or contains several large steps far away from the region of interest, potentially on the order of tens of micrometers, then it is possible for the stencil chip to make contact on different areas in a tilted fashion such that the actual membrane is differentially spaced from the surface by a large distance. In order to avoid this, the surface of the wafer segment on which the membrane is etched is etched back by 10-15 μm, leaving a frame around the membrane as the contact area, included 4 small support stubs, as shown in Fig 2.2.

The membrane thickness, which is typically 1-10 μm after the initial silicon etch, is fine tuned by placing it in a reactive ion etcher to reduce the overall thickness to less than 2 μm. Optical observation is typically sufficient to estimate the thickness to within one micrometer by noting the transmitted color and intensity of light through the membrane by eye. Membranes thicker than $\approx$50μm appear almost or fully opaque and silver colored, changing towards a dark red between 20-50 μm and towards a lighter orange and then yellow and nearly transparent as the thickness decreases below 10 μm . This is a quick check, possible even when the membrane is still oxide coated on one side during the etch process or covered with a thin film of etching solution or water. It is also possible to determine the membrane thickness using the Nanospec 2100 film thickness measurement tool in the McGill microfabrication facility, though the lower limit of the thickness determination is approximately 1.5 μm. The tool sweeps through a series of optical wavelengths and compares the reflected intensity while taking into account the given indices of refraction. Placing the silicon membrane in the FIB, both micrometer and nanometer size features are then milled as shown in Fig 2.1(c). A dual beam FIB, Zeiss 1540 XB at the Université de Sherbrooke, is used to create openings in the membrane, which are then measured using the SEM at a tilt angle of 54 degrees. In order to perform electrical measurements using the wires deposited using these stencils, 2 large openings are created in the membrane 50 to 100 μm in length which are separated by 5 μm as shown in Fig 2.1(a). To bridge these two openings, the region between them is thinned to the order of 50-200 nm and an opening from 50-200 nm is milled, with an aspect ratio of local membrane thickness to line width of less than 2. The thickness of this region is designed to be similar to the width of the slit, such that shadowing effects due to the aspect ratio of the mask do not dominate during deposition [47]. Typical FIB beam currents for the micron sized openings are on the order of 2-5 nA, 100-500 pA for the thinning process, and 10-50 pA for the final 50 nm slot. The problem with high aspect ratios is that the incident beam from the source is neither perfectly collimated, nor necessarily perpendicular to the sample, thus large thickness deviations will result in the beam primarily depositing on the interior sidewall of the mask slit itself. Milling of the large openings and the thinning process both take place at 2 nA beam currents, while the final narrow line is created using a beam from 5 - 50 pA depending on the precise width required. This has the effect of creating two macroscopic openings with a single thin opening for depositing both contact pads and an integrated wire in a single step.

A further refinement of the structure is possible by creating a gradient of thickness rather than a single thinned central region. The advantage in this case, as will be discussed further in the following sections, is that it reinforces the membrane, increasing the effective bending moment of the entire structure in order to allow for the deposition of highly stressed films onto the surface. Without this reinforcement the stencil opening acts much like a large cantilever and can deflect by as much as micrometers, causing significant broadening of the slot. In order to create this staircase the FIB is used at intermediate currents, typically several hundred pico-amperes to thin the membrane, starting from the thickest part and moving inwards. The only significant constraint on the length vs height of the thinned sections is the possibility of occluding the incident evaporant beam. As shown in Fig 2.1, for a nearly parallel beam it is a fairly loose constraint. The difficulty primarily arises with incident beams which are at slight angles to the normal, if for example the sample is rotated with respect to the source. If we assume a misalignment of 10 degrees with respect to the source then the length of the final segment can be a minimum of 100 nm for a 500 nm thick first step before line of sight is impaired and evaporated material will be physically blocked from reaching the surface. This does not provide a significant constraint on the step design as the final segment is typically at least 200 - 300 nm long.

Deposition in UHV takes advantage of the long scattering length associated with particles in a low pressure environment, typically kilometers in UHV. As a result, evaporated materials are considered ballistic, with the evaporated source nearly a point or collimated source, of material. Stencil masks take advantage of this property, physically occluding the evaporant source to sample line of sight.

Producing features on the sample which accurately reproduce the stencil dimensions relies critically on the spacing between the sample and stencil mask. Given the dimensions shown in Fig 2.1(b), it is apparent that from geometric considerations that the width of the deposited features is

$$W = w + \frac{d}{D}S \tag{2.1}$$

where w is the stencil opening size, d the spacing between sample and mask, D the source to mask spacing, and S the size of the source. This assumes of course that

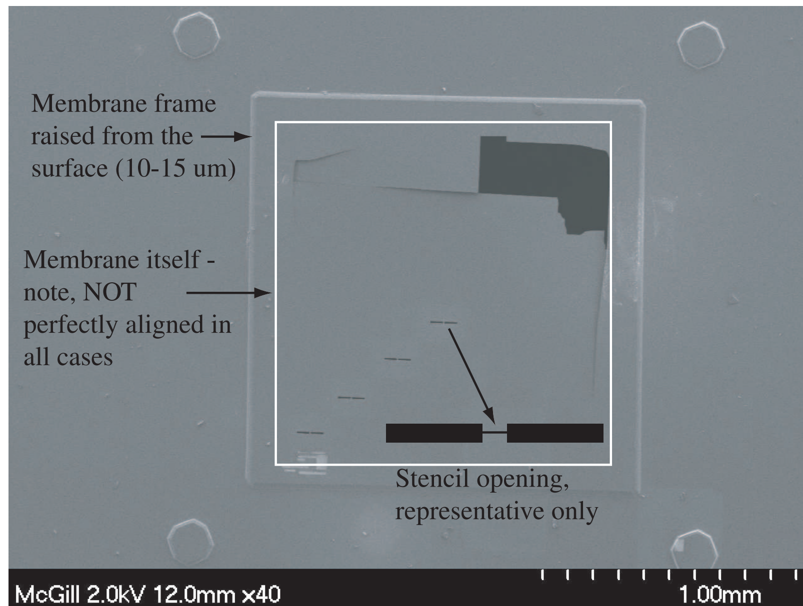

Figure 2.2: Damaged silicon stencil. The membrane was damaged during an approach procedure, but the low surface stress prevents it from spontaneously breaking further. (Inset) Schematic, 2 60x5 μm electrodes bridged by a 50-500 nm x 5 μm wire

$D >> d$, $S >> w$. In the geometry used in this study, because the nanoscale features are recessed from the sample surface, there is unavoidable spreading in the deposited features. For a 2 mm source at a distance of 10 cm with a spacing of 1 μm, the spreading should be limited to 20 nm, if surface diffusion of the adsorbates is not a significant factor. Similarly, there is a reduction in the feature size at the top of the deposited structure by the same fraction. This results in a diffuse edge to the deposited wires [40]. A side effect of this reduced coverage near the edge, for materials such as gold which have relatively large grains, is that there is a significant region near the edge of the mask where the wire is composed of electrically distinct islands which gradually evolve into the bulk film. The advantage of this procedure is that the mask itself can be in contact with the sample, but have a known spacing d to the critical 100 nm section which is protected from damaging contact with the sample itself. To avoid this feature enlargement, it is possible to perform the milling process from the back side of the wafer, thereby allowing better contact with the sample but with a consequently greater risk to the stencil.

In order to achieve nanometer scale features on the surface the stencil mask must be sufficiently close to the surface. Any elevation from the surface will create a cor-

responding increase in the feature size on the surface, the broadening shown in Fig 2.1(b). In order to achieve this necessary feature size the membrane must be as thin as possible, while still retaining sufficient structural stability. The general microfabrication steps involved are: creation of the silicon membrane using wet chemical etching, thinning of the membrane to less than 2 μm thickness using reactive ion etching (RIE), and milling of the openings on the membrane itself using the focused ion beam (FIB). Silicon membranes have the advantage of negligible residual membrane stress, but significantly poorer thickness control than the comparable silicon nitride membranes, which can be as thin as 50 nm. The increased thickness gives the membranes significantly higher structural stability, membranes have been observed with significant cracks as shown in Fig 2.2, or even openings as large as 20% of the surface area missing without failure. Silicon nitride membranes on the other hand typically have significant rupture problems simply under the native stress with a large openings milled or etched in the membrane, this can be reduced using strengthening coating on the membrane prior to deposition [46]. The effect can also be minimized through the suitable choice of strain relieving openings in a membrane [54], but these will not be discussed.

2.3 Heating effects

The structure of the silicon stencils between manufacture and deposition is normally considered to be a constant, though some care is necessary with such delicate structures to avoid damaging them prior to use. In order to avoid any local clogging, contamination, or damage of the stencils, after the FIB procedure the pieces are not exposed to any wet chemical cleaning. If necessary they are lightly cleaned with compressed nitrogen gas, at an angle, to remove dust or surface contaminants.

In order to attach the stencils, discussed in section 1.10, it is necessary to attach the pieces to the holder for the sample approach. With early stencils, the pieces were attached using a conducting, heat curable epoxy, H20E (Epotek) by heating in air to 150C. During evaporation it was observed that the membranes were significantly clogged, with bubbling and other roughening of the thinned stencil surface and occasionally the nearby regions of the membrane. While it was originally assumed this

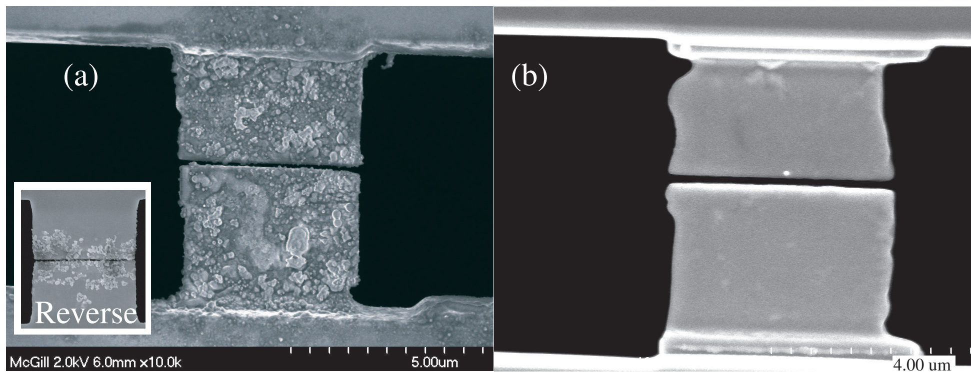

Figure 2.3: Heat damaged stencil. (a) Damaged stencil (b) Similar stencil heated under low vacuum for 2.5h at 150 ° C, no observable effects, (Inset) Back side of the stencil, this side faces the evaporant material, but is opposite the side used to FIB the structure

was a result of the deposition procedure due to local heating by the incident metal atoms, in particular tantalum with its high melting point, it was discovered that the heating process alone was sufficient to cause this distortion. With temperatures as low as 100 ° C it was observed in every case. What was found was that the critical factor was the presence of both atmospheric pressure, presumably oxygen, and elevated temperatures. Similar heating, whether in low or ultra-high vacuum had no effect on the membrane. In addition, the presence of this distortion is also located solely on regions of the membrane which have been exposed directly to, or adjacent to, the gallium beam used for the FIB process. Some small damage is occasionally observed within several hundred nanometers of the opening but only along the edge of the milled region and always greatest adjacent to the thinned region.

The precise mechanism of this process is still not well understood, but some conclusions can be drawn from the data above. First, while the gallium implanted and left behind by the deposition process should have a sufficiently low melting point at these temperatures to be potentially mobile, the same effect would be expected at both atmospheric pressure and under vacuum if it was a simple diffusion process of molten gallium metal. Secondly, previous studies have used gallium metal catalysts in order to cause the growth of silicon oxide nanowires. [55] In that work, small gallium clusters, strikingly similar to the spheres observed on the surface of the damaged stencil, are used as catalysts in a vapor deposition growth process. In this case however the presence of gallium is likely uniform across the surface, it is possible that a combi-

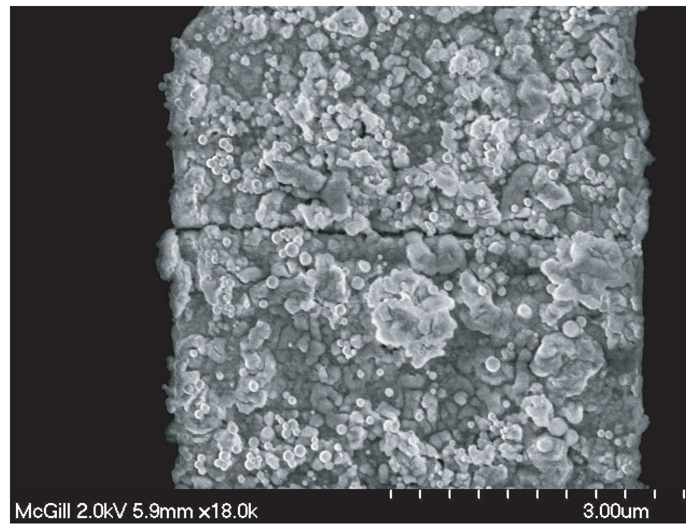

Figure 2.4: Damaged silicon membrane with spherical nodes shown

nation of local growth and relaxation processes are sufficient to cause the movement and aggregation of the gallium metal into individual nanoclusters as shown in Fig 2.4. These spheres are typically 50-150 nm in diameter. Unlike the example from the literature however, the gallium metal while present, does not appear to act as obvious catalysts. While the spheres may have initially guided the deformation of the surface, they do not appear to have a spatial connection to the height or position of the pillars.

It is also possible that the thin regions have sufficiently weaker heat conduction that they act as local cold traps during heating, phonon scattering at surfaces is known to cause decreased thermal conductivity in thin silicon structures [56]. The argument against this possibility is the observation of similar damage in regions of the membrane which have been slightly milled (trenches much less than the thickness of the membrane, at most a few hundred nm, which are milled as test and alignment features on the membrane surface) but not to a significant degree, and the lack of any contamination on the back side of the membrane except close to the FIB openings, even in regions where the silicon was less than 100 nm thick.

Once understood, it is relatively simple to avoid the problem by using epoxy capable of curing at room temperature. Torr-Seal low vacuum epoxy(Varian) is currently used to attach the stencils, curing overnight, typically for 12-14 hours. It is worth noting however that for other applications involving the FIB, this can be a potential

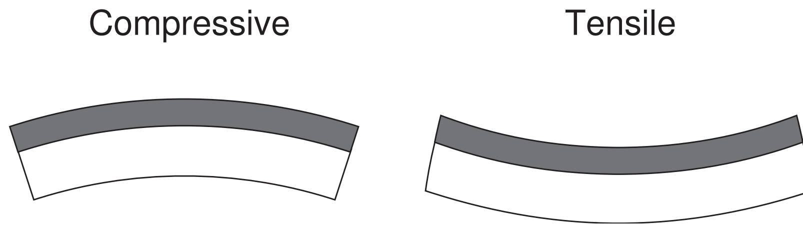

Figure 2.5: Compressive vs tensile surface stress for a deposited film (dark) on a thin substrate

problem, particularly in the case of silicon based structures which may need to be heated.

More work needs to be done to fully understand the local mechanism of the damage and to verify if the theory given above are correct. However in the current situation, given the time involved in creating each stencil mask it was not feasible to do so. Thinned silicon structures would be equally suitable for these tests, as the incident beam need not fully penetrate the silicon membrane to have similar effects, as demonstrated.

2.4 Stress analysis

A known problem in the deposition of any material onto a substrate of a different type is the issue of surface stress in the applied film and substrate. Stress in a multilayer structure can arise in a variety of ways, for example, due to a mismatch of the lattice constants of the surface and adsorbate, differential thermal expansion coefficients, the establishment of strained metastable states at the interface during deposition, or impurities or defects in the crystal structure [57]. Depending on the materials involved, the thin film or substrate may distort or reconstruct at the the interface between the two materials as a result. The precise mechanism of this stress is determined by the interface size and structure, film thickness, adsorbate and substrate combination, and deposition conditions. There will be some degree of surface stress with the deposition of virtually any material, but as long as the stresses involved are sufficiently small, the substrate structures will remain relatively unstrained, and resist deformation. The particular direction of the induced surface stress in the deposited

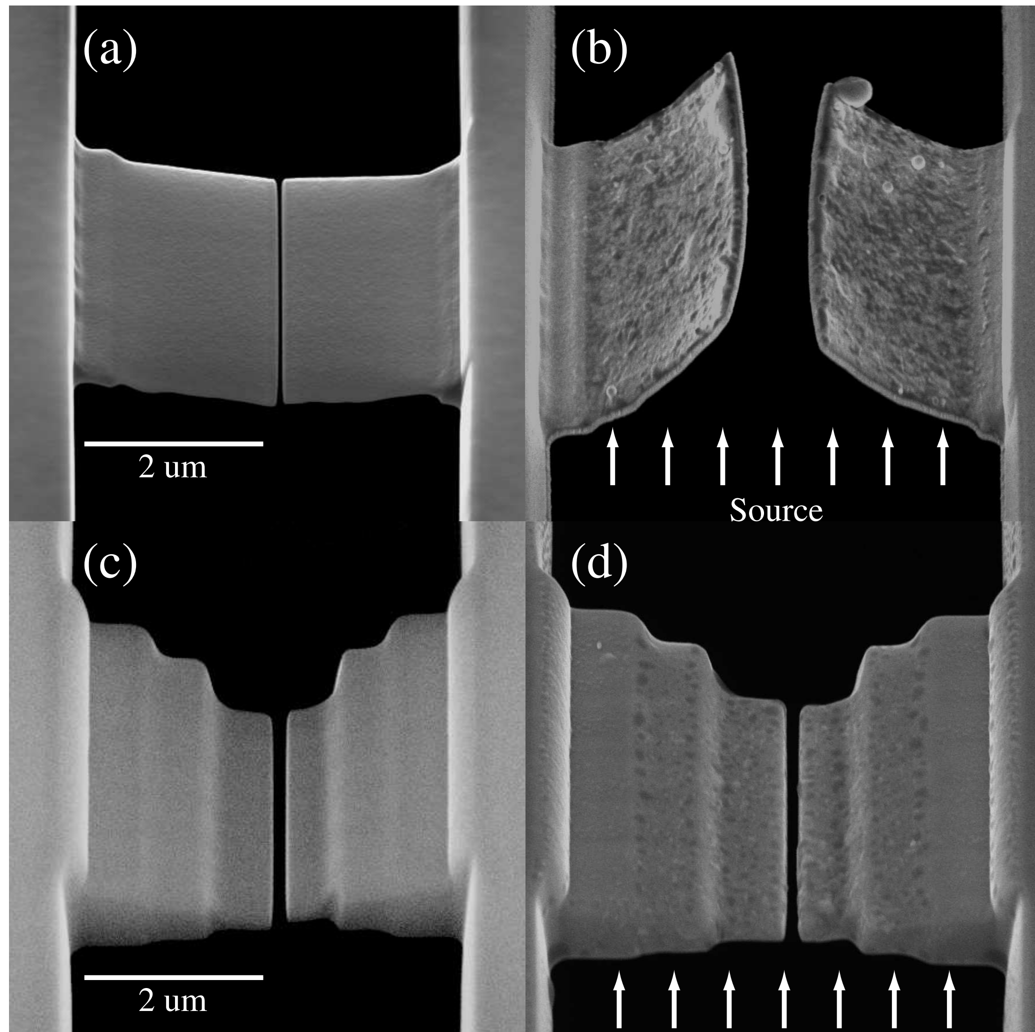

Figure 2.6: Single stencil features from two different membranes, before (a,c) and after (b,d) the deposition of thick Ta films: 45 nm for (b) and 27 nm (d).

film, which is directly translated to the substrate material, is not necessarily known for every case and may be compressive or tensile. In microfabrication and MEM's design, this problem is particularly important as the dimensions of the machined structures are comparable to that of the deposited film and often subject to severe distortions.

For the silicon stencils used in this work, relatively simple structures are created in the silicon membrane which roughly resemble that of two adjacent and oppositely facing cantilevers or beams, albeit of fairly large cross-sectional dimensions (typically 5x2.5x2 μm). As the membrane is created from a single crystal wafer, with minimal

doping, it begins with relatively low initial stress. After FIB, the residual stress is still low enough that the membrane is locally flat in most cases, though this can vary from structure to struture. Typically no noticeable bending is observed. Even after the milling of the membrane and potential damage and implantation by gallium ions there is no observed consistent curvature of the beams, implying very low residual stress.

After repeated depositions of relatively high stress metals such as tantalum, with typical surface stresses on the order of GPa on silicon [58], significant deflections were observed in the stencil beams, with an observed compressive stress as shown in Fig 2.6. From the magnitude of the bending, and a simple model of stress induced deformation in cantilevers discussed below, it was possible to estimate the stress in the tantalum film, which was then used to redesign the structures in order to create a stencil with similar dimensions and openings, but a significantly increased bending moment. Typical tantalum films were then deposited on the improved structures, with a level of membrane distortion less than observable limits based on this technique. The same membrane was then used for as much as 3 times the original tantalum film thickness with no distortion even at this point (100-200 nm Ta film thickness).

In order to measure the membrane deflection, the stencil openings were imaged using the SEM at a 45 degree angle, looking into the gap as shown in Fig 2.6. This necessarily induces a reduction of the observed feature length in the vertical direction, with a scaling factor of $\sqrt{2}$ simply due to the geometrical projection onto the detector. In order to measure the beam deflection, the commercial package ImageJ was used to manually follow the contour of the bottom of the beam with the data points, typically 6-10 points along the beam axis, fit to a circle using Origin^{TM}, Fig 2.7. The fits were quite good and as expected the bending shape under stress is generally well described as circular rather than parabolic or exponential. Of the original 9 wire openings on the sample, with 17 potential beams on this stencil (from 9 openings with at least one with a single beam rather than a pair), 12 were sufficiently free of defects to be quantified. Those which were not were typically deformed by non uniform milling, holes in the membrane, or other problems. The average beam thickness was 160 $\pm$20 nm, 2.46 μm long, and approximately 5 μm wide. Measurements of the beam thickness were complicated by poor edge contrast, rounding at the edge of the structure under FIB, and limited electronic contrast due to the edge in the SEM

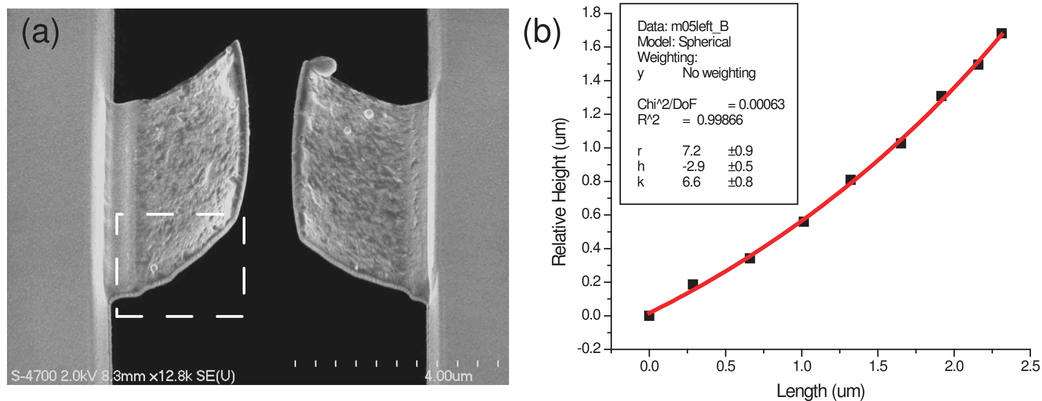

Figure 2.7: Sample fit for one membrane feature, (a) SEM data, fit region indicated (b) Fitting region with the corrected height ($\sqrt(2)$ for 45 degree image angle), measured points and the circular fit shown

image being the major source of this error, with thickness's from 110 nm to 220 nm $\pm$ 5 - 30 %. The average deflection was 1.01 μm, though this is not used directly as discussed below. From the physical dimensions, Ta film thicknesses, and substrate (beam) thickness, it was then possible to approximate the stress of the deposited film at this film thickness. There was a noticeable disparity in the left right deflection data, see Fig 2.7(a), which is not well understood. Deformations over large surface areas of the membrane may lead to a slight local tilt in the measured region, but this should not significantly affect the measurement of the radius, from which the film stress is actually determined. The radii do however differ. This may also be a result of an unequal deposition of evaporated material on the membrane itself, due to the source not being perfectly perpendicular (or in this case, the stage on which the sample rests having a slightly rotation). However, even in the uncoated membranes this effect is often observed, with a slight vertical displacement between the left and right features. This suggests rather a variation in the global stress due to the placement of the structures themselves or the FIB milling process itself. The diagonal shift of the structures across the membrane window, as described earlier, maybe be the driving force for this effect. As well, the measured thickness in each side is slightly different, 8 % larger on average. This is not enough to account for the variation in radius and calculated stress, but it is in the correct direction (thicker membrane structures have a reduced deflection, for example on the right in the figure shown). Where the discrepancy comes from however is unclear, visible mounding due to redeposited material FIB milling process not visible on either side.

The measured values for one stencil are given in Table 2.1, along with the calculated and corrected stress values, as discussed below.

image	R radius(μm)	L radius(μm)	R stress (GPa)	L stress(GPa)
m01	5.9 ± 1.0		1.6± 0.6	
m03	6.5± 0.7	7.9± 0.6	2.0± 0.8	1.0± 0.5
m04		12± 2.5		1.9± 0.4
m05	5.3± 0.5	7.2± 0.9	1.5± 0.5	1.0± 0.2
m07	12± 2	13± 3	1.9± 0.3	1.8± 1.2
m08	71± 66	33± 17	0.4±0.4	0.5± 0.3
m09	6.3± 0.4	6.8± 0.5	2.0± 0.6	1.9± 0.3

Table 2.1: B1082 Membrane: Measured radii, corrected film stress (using Eqn 2.4). M08 represents an outlier, while bent these particular beams are nearly straight, flexing instead at a weak point and hence have a large radius of curvature

The bending moment of this sort of rectangular beam is a common problem in microelectronic devices and surface science. The most common means of quantifying the curvature is based on work first published by Stoney [59], which examined the bending of a film of nickel plated onto a stainless steel foil. As long as the thickness of the deposited foil is thin compared to the substrate, and the substrate itself thin compared to the radius of curvature, a relationship between the various quantities can be derived. A more recent refinement of this model will also be discussed subsequently.

The modified form of Stoney's formula [59] is given by :

$$\sigma = \frac{Et_{sub}^2}{6Rt_{film}(1-\nu)} \tag{2.2}$$

where σ is the film stress, E is Young's modulus of the silicon substrate, t_{sub} is the beam thickness, R is the radius of curvature of the beam, t_{film} is the film thickness, and ν is Poisson's ratio for silicon. A ratio of $\frac{E}{(1-\nu)} = 180.5$ GPa was used [60] for E and ν. One can also write this in terms of the bending moment of the thin rectangular section,

$$\sigma = \frac{2EI}{Rt_{film}t_{sub}b(1-\nu)} \tag{2.3}$$

with b the length of the beam, as in the horizontal direction in Fig 2.1(d), where the moment $I = \frac{bt_s^3}{12}$. For cases of small bending is is also possible to substitute $R = \frac{l^2}{2\delta}$

where l is the beam length, and δ is the deflection at the end of the beam. The beam is considered entirely from a side cross-section, under the assumption that all deflections are in plane, but this not entirely accurate, particularly for widths which are comparable in size to the length of the beam.

The most important assumption which is violated here is the ratio of the film thickness to that of the beam. In the stencil measurements given above, the film thickness can be as much as 40% of the substrate thickness so corrections to the calculated film stress are called for. Klein [61] has shown that the stress value is overestimated by a fraction ϵ given by the thickness and modulus ratio of film to substrate, δ and γ respectively.

$$\epsilon_{st} = \frac{\delta(1 - \gamma\delta^2)}{1 + \gamma\delta^3} \tag{2.4}$$

The modulus for Ta on (100) silicon is taken to be 175 GPa [62], with the other parameters as given above. Taking into account this correction, an average film stress of 1.3 ± 0.1 GPa is calculated based on the measured beam radii, which is consistent with measured stress values for tantalum thin films deposited on bulk silicon wafers [58]. The previous tantalum film measurements were not given for thicknesses this low, but extrapolating the film stress from Guisbier's published data is consistent with our film stress. This deflection is larger than that predicted based on the radial curvature and these stress values but is a result of the non uniform curvature at the corners as well as a zero offset in the deflection as measured from the fixed end. For this reason the measured radii were used over static deflections.

2.4.1 Staircase structure

Preventing this distortion is a significantly more difficult task. The simplest solution, both intuitively and as shown in stoney's equation, is to increase the thickness of the stencil as large as possible, in this case to the thickness of the membrane itself. The difficulty that soon arises is in getting the evaporant material to the substrate effectively. Several techniques have been explored to reinforce stencils and improve the lifespan during deposition including corrugated structures [63], large silicon supports on silicon nitride membranes [64], and strain relieving openings built into the membrane itself (this deals with intrinsic stress in the membrane due to the openings

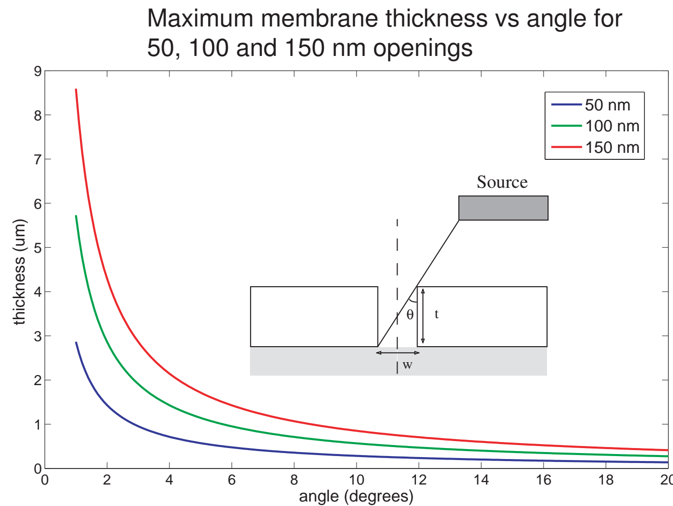

Figure 2.8: Illustration of the line of sight problem with high membrane thickness to opening size ratios. Plot for 3 different opening sizes at which the incident beam is totally occluded, it will actually begin to block incoming material well before this point.

but doesn't provide additional reinforcement during deposition).

There are two issues to consider, the aspect ratio of the membrane thickness to the openings within, and the presence of large nearby structures which can block the material from reaching the surface. The former case is illustrated in Fig 2.8. At some angle and thickness, the beam will be sufficient to totally block incident material from the sample, for a 10 ° angle this will occur at a ratio of 5.67, with a 20 ° misalignment the maximum ratio is 2.75. These however are fairly loose constraints, in practice the source material will be occluded well before this point, but it serves as a reasonable minimal target. Thus, for even a 1 μm membrane, at a 10 ° angle the minimum feature size possible will be 176 nm, or even larger in practice. This is consistent with the limitation on the size of the staircase structure described before, as of course the effect is from an identical geometry, though in this case it is an opening with a single sidewall, rather than an opening with nearby sidewalls from the rising steps. A general rule of thumb used by the stencil deposition community then suggests an aspect ratio of no greater than 2-3 at the outside for successful depositions, which is supported by the simple calculation given above. With these considerations in mind, the magnitude of the bending was calculated in order to find the optimal height of the steps and lengths in the staircase for designing these staircase structures. It is

assumed that each step in the staircase represents a beam in its own right, with a slightly different radius of curvature. By aligning the segments and their slopes at each point to create a continuous structure one can estimate the bending of the aggregate beam.

The calculated radii of each section are assumed to depend strictly on the induced stress as discussed. Using each calculated radius

$$R = \frac{Et_{sub}^2}{6\sigma t_{film}(1-\nu)} \tag{2.5}$$

a circular cross-section is assumed, the arclength for each segment (assumed constant despite the strain), and the slope from the simple circular segments it is simple to create a plot of the deflection of a given beam by simply aligning the slopes and positions of the two endpoints, $x_1 = Rsin(\frac{L}{R})$, $y_1' = x_1(R^2 - x_1^2)^{\frac{1}{2}}$. The position of subsequent points is simply the difference between the start and end with a known arclength, radius, and fixed initial point and calculated x_1 and y_1'.

As the curvature is dependent on the square of the substrate thickness, only the thinnest segments will have a significant effect on the deflection. There is a great deal of flexibility in the choice of final thickness, gap size, number of steps, and the height and length of each step. For the structure shown in Fig 2.6(c) an approximate vertical deflection of 46 and 40 nm for the left and right segments is calculated respectively. This gives more than an order of magnitude less vertical deflection than the unsupported case, and an even smaller increase in the gap size horizontally, on the order of nanometers. By comparison, a single 100 nm beam with a length of 2.5 μm would give a deflection on the order of 400 - 500 nm and an increase in the gap size of tens of nanometers.

Two membrane openings with both the original and staircase structures are shown in Fig 2.6. The width of the final segment in this structure is 100 $\pm$ 20 nm and is the smallest of the beams on the membrane, hence the most susceptible to significant deflections under stress. The deposited film thickness in the two cases are 45 nm and 27 nm for the original (a) and staircase (c) structures respectively. While a significant deflection in the original feature is observed, shown in Fig 2.6(b), the staircase structure (d) shows no visible deflection. Deflections less than several tens

of nm are difficult to detect in the SEM image at zoom levels capable of tracking the entire structure. In comparison to the original structures with a similar final thickness, the distortion is more than an order of magnitude smaller, consistent with the projected deflection above. Repeated use of the same mask for a significant number of evaporations and more than 100 nm of deposited tantalum was found to have no visible effect on the deflection, though at this point clogging of the wire gap begins to become an issue.

With the above considerations in mind, a number of structures were milled using the FIB in various membranes. The basic electrode, wire, electrode structure is the simplest, but it is worth noting that it is also possible to use the popular bowtie structure, or other variations such as a wire with a predefined gap in the center. Examples of stencils with both structures are given in Fig 2.9. Relatively modest opening or gap sizes are used, 180 nm and 200 nm respectively, but the lower size limit is given by the size and alignment of the ion beam and secondary milling effects only, structures as small as 50 nm are possible with this FIB.

2.5 Multiple mask alignment and macroscopic electrodes

The masks previously described were all based on the silicon microfabricated stencils introduced above. In order to effectively use these stencils to make contacts on the sample face in UHV without lithographically defined electrodes requires some form of macroscopic deposition which is pre-aligned to the silicon stencils used subsequently. A copper TEM grid (SPI supplies, 50 to 100 mesh parallel bars with 65-84 μm thick beams) is used as a mask to form two large and easily contacted electrodes with a gap, as described by Gartner [46]. The grid is glued to the face of the mask holder using a high vacuum epoxy, and all but one of the parallel bars removed with a razor blade under the stereo microscope. The approach and retraction method is otherwise identical to that described for the stencil masks in the previous section.

There are a wide variety of suitable metals for the deposition of wires for molecular studies, noble metals such as gold are typical for the their lack of chemical reac-

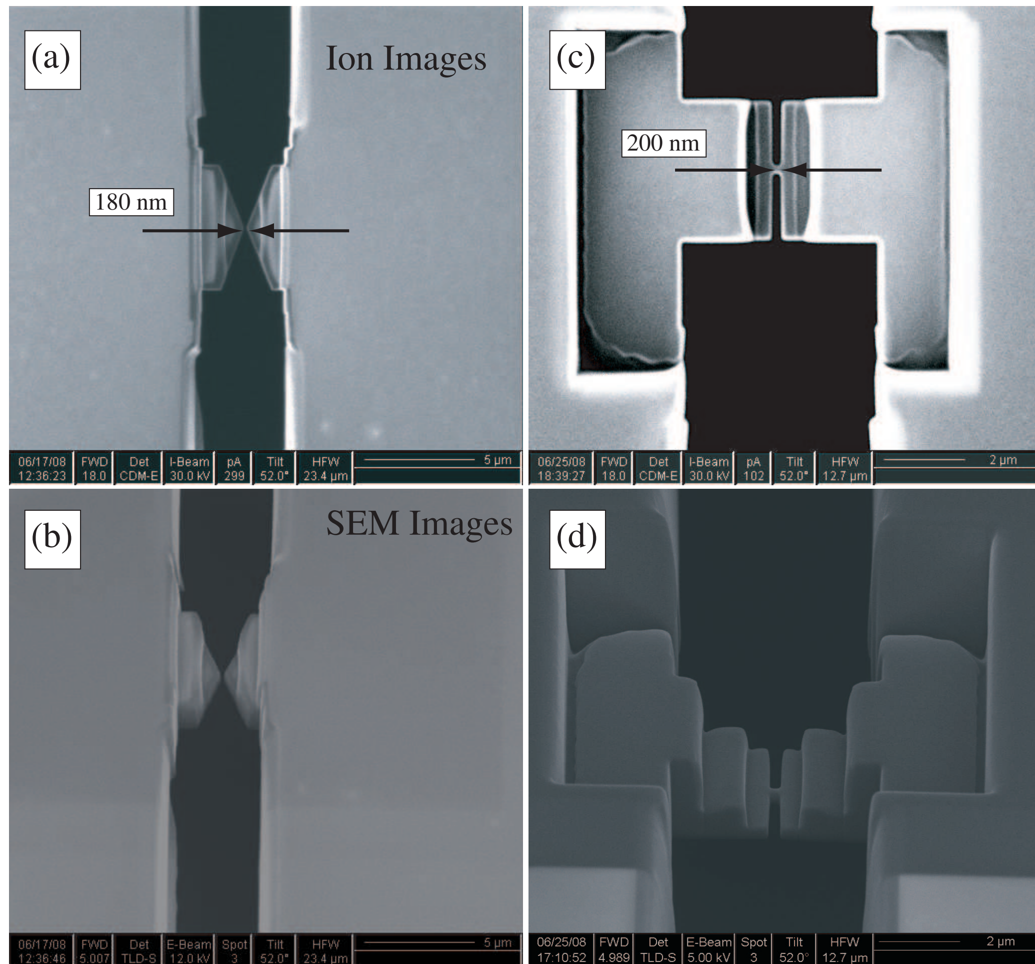

Figure 2.9: Alternative stencil structures, bowtie and with an integrated gap. (a,c) Ion image of the milled structure, dark regions correspond to openings in the membrane. Steps in the structure are as described above (b,d) Angled SEM images of the structures.

tivity and relative ease of deposition. Matching the metals to the substrate is not entirely trivial, particular in the case of the alkali halides. Every metal examined on this substrate, gold, tantalum, and palladium have dramatically different deposition characteristics as described above but universally poor epitaxial growth [23, 41]. This results in very large island heights at a small coverage, and the need for significantly thicker films, typically 20-25 nm for gold and between 5 and 10 nm for tantalum, in order to achieve a continuous film. There are a number of factors in determining the optimum growth of metals on surfaces, but one parameter is the relative lattice constants of substrate and overlayer, in addition to the surface energies [41]. In the case of KBr the lattice mismatch is usually quite large, 38% for gold, 45 % for copper, 40 % for platinum and 30-50% for other typical metals. The surface energies may actually play a more significant role, the difference in surface energies can lead to the creation of islands, subsurface structures, or wetting layers [41]. In the end it was initially decided to use gold to form the macroscopic electrodes and for the final contacts (pit nucleation clusters) despite its large grain size, but to use tantalum as a wire material. Tantalum growth gives connected geometries at significantly lower coverages than gold, with less edge and surface corrugation. This may be of less importance than the electrical and thermal characteristics of the material as discussed later.

The contact electrodes are constructed with 30-35 nm gold films. Attempts were made to create similar contacts with tantalum but the films while locally contacted were typically not electrically continuous over the whole of the sample. It is likely that surface steps in the KBr surface, on the order of tens of nanometers or higher, were more likely to cause disconnects in the tantalum film but not in the more forgiving gold film, likely as a result of the thicker gold layer.

Alignment of the gap created using the TEM grid and the subsequent evaporation of the stencil mask is extremely important. There are two stages of alignment used in order to ensure the alignment of the two different mask stages. First, an alignment jig is used ex-situ to note the position of the TEM grid which was used to create the gap on the sample and the macroscopic contact electrodes. The mask is removed after evaporation of these electrodes, and the copper grid replaced by the silicon stencil chip. The position of the center of the array of FIB openings on the stencil stencil is aligned with that of the location of the electrode gap as noted prior to evaporation

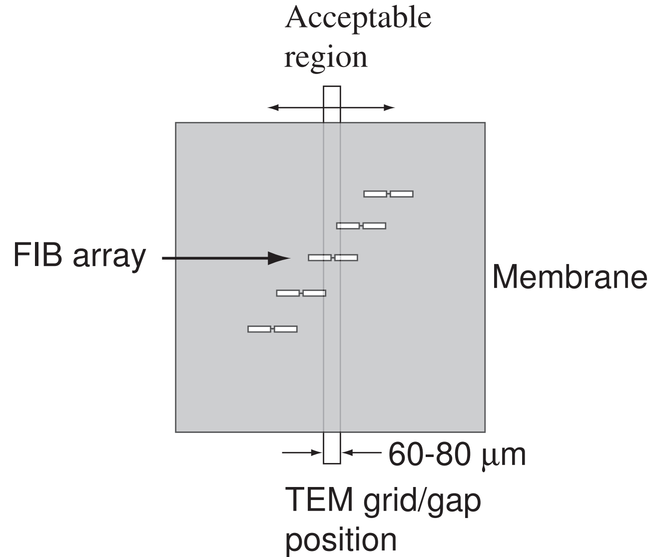

Figure 2.10: Stencil mask to TEM grid alignment, schematic. The position of the gap, indicated by the TEM grid beam, is noted on the the alignment jig and used to position FIB array within the acceptable region indicated

to within ± 50 μm , Fig 2.10. The jig uses a triangular cross-section (the inverse of the v-groove on the mask holders), that keeps the mask holding piece firmly in place similar to the sapphire sphere shown previously. The mask is then glued into place using Torr-seal and cured overnight. After curing, the mask is then moved into the chamber and baked for 7 hours to remove adsorbed water and reduce outgassing and potential sample contamination.

The center of the FIB features on the mask are aligned with the position of the gap under an optical microscope, but there is some play in the precise position due to inaccuracies in the holder, and variations in the position of the sample itself due to the positioning of the elevator and sample in the UHV chamber. In order to attempt to guarantee the alignment, the features on the stencil mask are lain out in a diagonal array, with the spacing between the center wire of adjacent openings approximately the same as that of the mask itself. For example, a 75 mesh grid, with a beam width of 70 μm , will have a wire near the center of the membrane, another 70 μm away, the next a similar amount and so on. In this way, as long as the gap on the sample overlaps this region, it should always have a minimum of a single opening in the center of the membrane. In practice this has not always worked, the gap size on the sample can be slightly reduced by imperfect contact with the sample face, and the

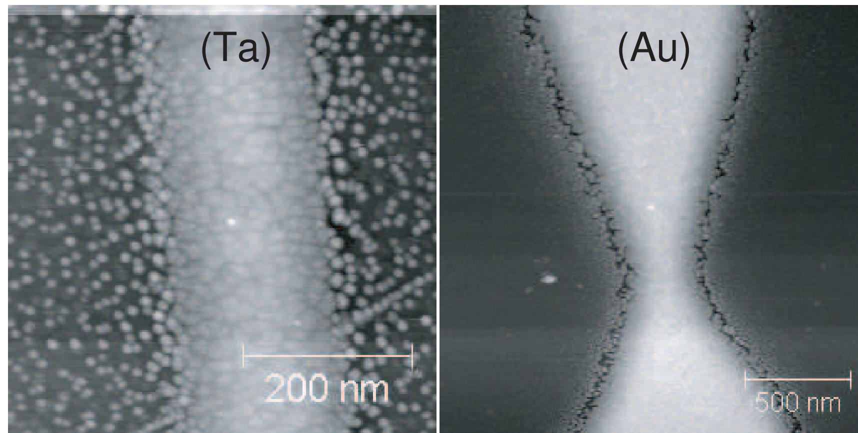

Figure 2.11: Tantalum vs gold wires, 11.5 vs 30 nm thickness

original stencil positions were not always the ideal spacing.

2.6 Wire deposition

A number of wires have been deposited using the stencils described above, in combination with a narrow gap given by a TEM grid or in earlier attempts by a prefabricated silicon stencil structure, described previously [11]. Using the piezo walker the silicon stencil is approached into direct contact with the surface face for deposition. As the alignment is determined by both the lateral external alignment of the two mask stages and the internal movement of sample and stencil, it is sometimes observed that the gap is only partially bridged, or bridged more than one feature.

The majority of the deposited wires are tantalum though in some cases gold was also used, an example of each is shown in Fig 2.11. Even in a relatively thick tantalum film such as shown, 11.5 nm, the dendritic growth of the tantalum grains is obvious, while gold forms relatively spherical tall clusters, in agreement with previous measurements [23, 41]. The gold islands appear to initial nucleate from the edge inward, with a sudden shift to a connected grain structure with a larger length scale than the grains themselves. Tantalum on the other hand has a significantly sharper transition at the edge, the sample shown has an unusually large amount of diffuse nearby tantalum particles, but once the grains transition to the connected pad there is little or not visible cracks or voids near the edge. A typical image of this is given in Fig 2.12,

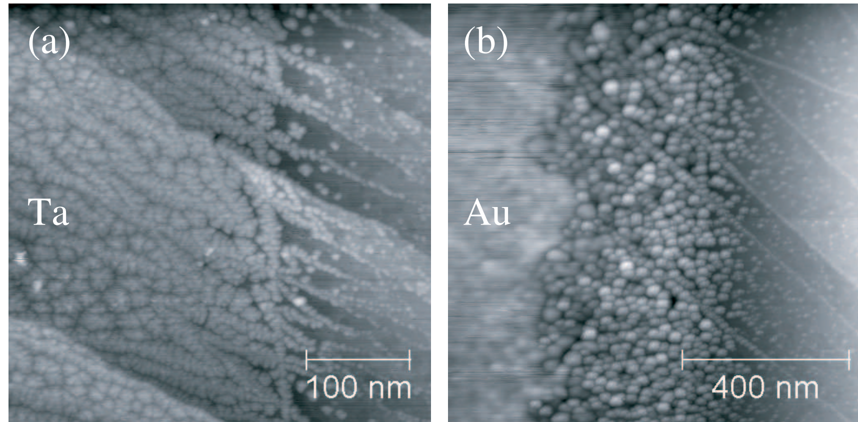

Figure 2.12: Typical metallic edge for large gold and tantalum electrodes (a) Tantalum edge near the 5 μm wide wire region masked using the silicon stencil, (b) Gold edge masked by the TEM grid

the tip used to image the gold edge is slightly double, but the electrically connected region is clearly visible on the left as a blurring given by the change in potential.

The wire thickness was measured using either AFM or SEM, and the expected spacing between the sample and mask calculated using eqn 2.1, from the measured widths which are 40-330 nm larger than the stencil mask opening. As the stencil features are recessed from the mask face, this automatically gives a spacing of roughly the stencil thickness, typically 0.5-2 μm, but as shown in Fig 2.13, the actual spacing is often as much as several micrometers larger than this. The calculated distance is an overestimate, as it assumes no diffusion, and the measurement uncertainty is a result of both the SEM measurement, and the grain roughness at the wire boundary. Despite the large range in sample spacing, it is clear that the mask is within relatively close proximity to the sample, several micrometers at most, in virtually all cases and that the approach mechanism is working as intended. There are some outliers, not shown, with stencil distances as large as 30 μm or more, where the stencil forms no clear contact with the surface, but this is relatively rare with the current method. This is generally a result of a huge residual terrace on the corner of the sample after cleaving, as much as tens of micrometers tall, but sometimes difficult to resolve in the SEM image.

Outside of the central deposition region there is a large additional halo which has also been observed by other authors [65], this region extends significantly beyond

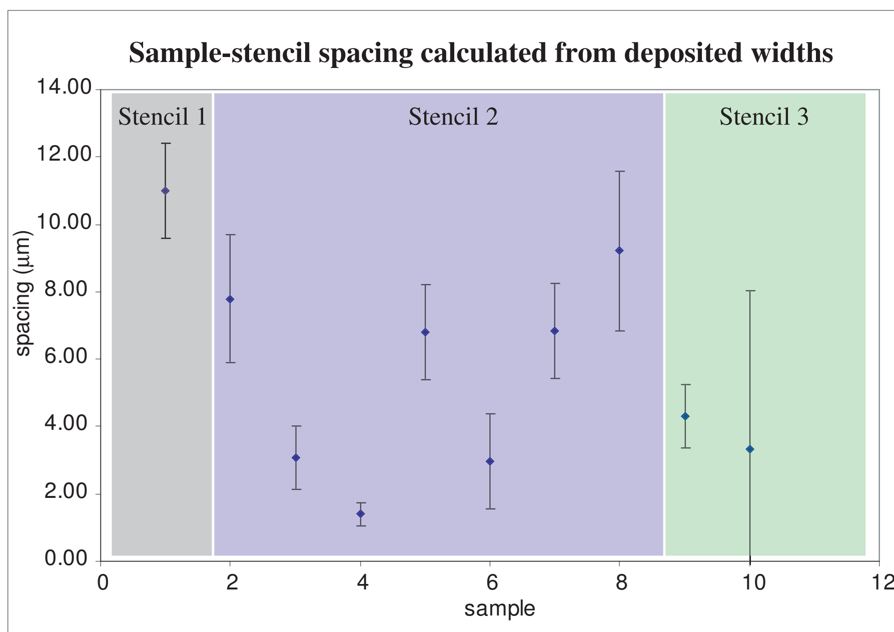

Figure 2.13: Calculated stencil-sample spacing for 3 different stencils. As the features are recessed from the surface, a minimum spacing of the membrane thickness (1-2, 1.2 and 2 μm for mask 1, 2 and 3 respectively) is expected. Surface diffusion is not taken into account

the strict geometric shape defined by the sample spacing and has not been fully explained. It is also noteworthy that for the mask labeled 2, also used to test the staircase structure, there was no visible systematic increase in the deposited feature width despite numerous evaporations, as would be expected if there was any visible stress induced deflection in the stencil by even tens of nanometers.

Assuming a successful evaporation, both macroscopic electrode films are connected by a single tantalum or gold stencil structure with a central wire 100-500 nm wide. The contact electrodes are then attached and measurements of the wire made during electromigration (Chapter 3) or used as electrodes for field-induced-deposition (Chapter 4), or both.

Some examples of successful deposition sequences are shown in Fig 2.14. The darkest regions are always given by the substrate, either KBr or silicon, with the lower electron yield in the SEM, then the Ta films, with the brightest regions given by the gold films. The tantalum films are 5-15 nm thick, with gold electrodes and wires 20-35 nm thick.

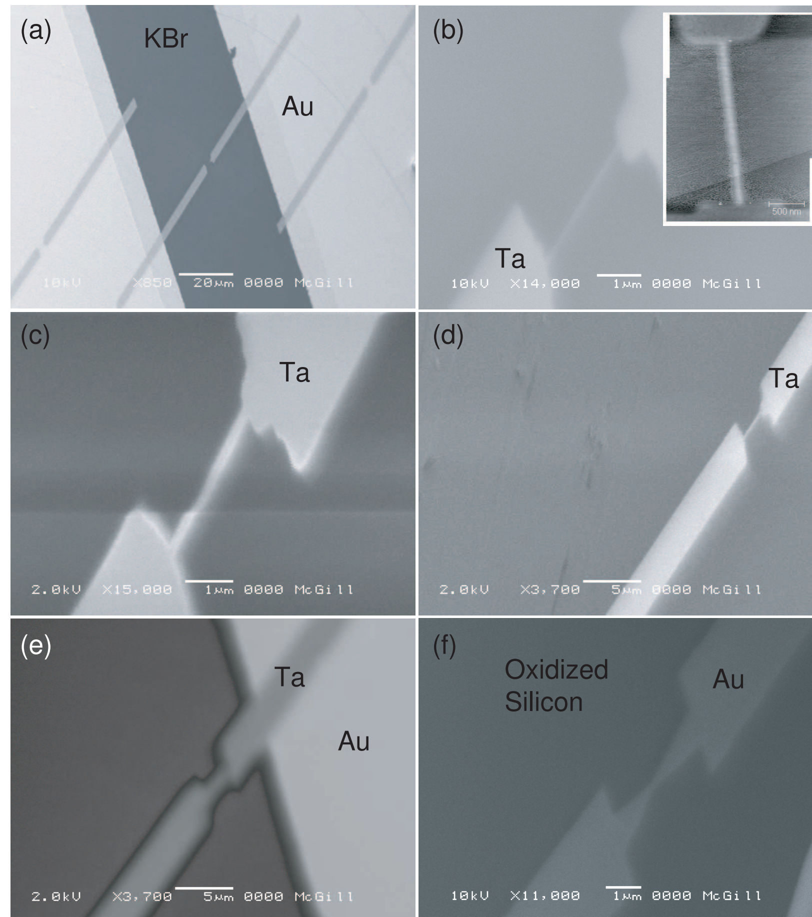

Figure 2.14: Deposited wires, all on KBr (dark areas) except (f), on oxidized silicon (a) Contact pad, electrode, wire, electrode, contact pad shown, (b) The same wire as (a) and also as shown in Fig 2.11(left) (inset) AFM image of the same wire, multiple images stitched to cover the full length of the wire, (c-e) Similar examples on different samples, mask used for (e) has an opening 200-1400 nm wide, edge features due to contrast adjustments for visibility, (f) Bow-tie structure evaporated ex-situ on silicon for electromigration, discussed further in chapter 3

What has been demonstrated thus far is the development of highly strain resistant silicon stencils, which are clearly able to deposit tantalum and gold films and can be positioned within several micrometers of the surface reproducibly, and capable of retaining pattern integrity over many evaporation cycles despite the high stress of the deposited films.

Chapter 3

Electromigration

3.1 Introduction

There have been many attempts in recent years to find ways of fabricating nanometer scale gaps in conducting wires for the purposes of molecular measurements. One of these techniques, electrically stressing the nanowires, or electromigration, involves passing enough current through the device to cause a high current density and to force the migration of metal atoms in such a way as to eventually break the wire. A significant amount of work has been done on electromigration which was originally understood as a primary failure mechanism for microelectronic circuits in the 1960's. Most of the work done in this community has been focused on understanding the mean failure time (MFT) for electrical interconnects [66] and how to prevent it from happening through a combination of different materials, barrier layers, and control of the maximum current densities. It was later realized in the molecular electronics community that these failures actually provide a route for the creation of near ideal gaps in nanowires for the creation of molecular devices [67, 68, 69, 70]. As the gap formation is critically related to the wire morphology and electrical stressing, it is possible to fabricate gaps ranging from the single atomic level to tens of nanometers or more, though the majority of the control over these gaps appears to be in the sub-5nm range. The main difficulties are controlling and understanding the process. The radically different driving interests in the two communities have given rise to

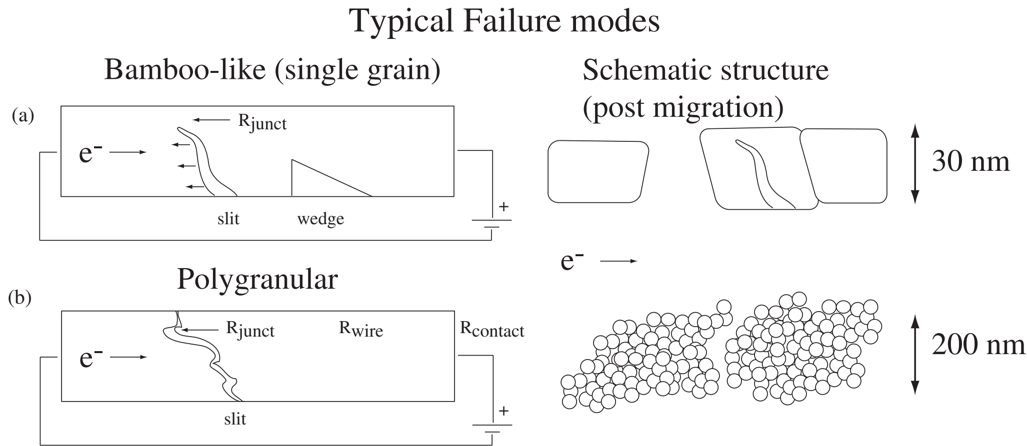

Figure 3.1: Typical electromigration paths. (a) Bamboo-like wire, migration is often transgranular and a single grain is shown for clarity, [2] (b) Polygranular wire, slits tend to follow the grain boundaries [3] (Right) Schematic structures at typical length scales for the gold wires discussed below.

very different approaches in both experimental and theoretical understanding of the electromigration process. Some of relevant details will be discussed below, as well as recent attempts to migrate devices on both KBr and oxidized silicon.

A full description of the morphological changes in metallic wires during electromigration is quite complex and not always well understood, there are some basic ideas which give insight into the mechanisms at play. These will also be discussed, as they give suggestions for the necessary criteria for both the wires and electromigration process in order to produce gaps at a variety of sizes, as well as why the process fails in other cases. The goal of this work is not to create a detailed description of the microscopic process of electromigration as this has been explored by many groups and can be found well summarized in several references by Scorzoni [71] or Durkan [1].

Electromigration is the movement of metal atoms in a solid through a momentum transfer from conduction electrons, it is also called an electron wind force. Ionic metal atoms moving in an electric field also experience a direct force due to the effect of the field on some effective charge per ion. This charge is often poorly understood, and may be negligible, in the same direction as the wind force, or overwhelm it entirely depending on the experimental conditions. The principle equation from which most electromigration results are derived is given by the following equation,

$$\mathbf{J} = \frac{N}{kT} D \left(Z^* e \rho \mathbf{j} - \Omega \frac{\partial \sigma}{\partial \mathbf{r}} \right) \tag{3.1}$$
$$D = D_0 e^{-E_a/kT}$$

where $\mathbf{J}$ is the ion flux, N the density of mobile elements, D_0 a temperature independent diffusion coefficient, k is Boltzmann's constant, T the temperature, Z^* the effective atomic charge number (taking into account both direct and wind forces), e the electric charge, ρ the resistivity, $\mathbf{j}$ the current density, Ω the atomic volume, and σ the mechanical stress [71]. This formula only strictly applies for the movement of interstitials in a crystalline lattice, for the movement of grain boundaries it can be modified by δ/d, δ the effective grain boundary width and d the grain size, but this too fails for complex orientations of the grain boundaries found in typical polygranular wires, discussed below.

The electromigration process is an activated one as shown, and the extent of the ion flow is controlled by both the wire temperature and the current density j. The wire temperature, raised by joule heating due to currents through the wire, is typically influenced by both the substrate and wire structure, including heat flow to the substrate. As the momentum transfer from electrons is the driving force causing the metal atoms to be displaced, typically voids and breaking points will open closer to the cathode side of the material [3], leaving mounds of deposited material to the anode side. During this process there is a competitive effect which occurs as the wire is heated, due to the increase in stress in the wire in the opposite direction. This is caused by both the variation in temperature across the wire, the differential expansion of wire and substrate, and the displacement of material by the electromigration process itself [72]. As mounded material accumulates on the cathode side the wire will gradually build up compressive stress which can eventually counter the force of migration on the atoms entirely.

Wires used for electromigration have a wide variety of characteristics, but generally fall under one of two general categories: bamboo-like or polygranular, with typical failures in the modes schematically shown in Fig 3.1. Bamboo wires have a width comparable to or less than the grain size and consist of end-to-end grain structures whereas polygranular wires are more irregular and may have many grains across the

width of the wire. While these sizes can vary significantly, an approximate width scale is from 1-100 nm for bamboo-like wires, and 100 nm and up for polygranular. Annealed gold wires can retain the bamboo-like structure with grains as large as 120nm on Si(100) [73]. Most of those discussed here will be polygranular with a few exceptions. In general the electromigration process in either case tends to take place with the formation of voids in the material which are perpendicular to the current direction. As the voids form they can be mobile and evolve with time but generally small voids with a size below some critical threshold form but remain constant with time until a critical void starts and propagates across the wire. Significant experimental and theoretical work has been done in modeling the evolution of these voids, most recent examples [74, 75, 76, 77, 78, 2] focus on bamboo-like wires, though there has been significant work done on polygranular wires as well [71]. The primary difference in the two cases lies in the diffusion processes involved. Polygranular wires have many more grain boundaries, and the principle diffusion tends to take place along void surfaces, grain boundaries, or from grain boundaries to the bulk [71]. Bamboo wires are restricted to surface diffusion and across grain boundaries and tend to have consequently higher failure current densities. The reason the void tends to propagate perpendicular to the current is thought to be the increase in current density adjacent to the slit, as well as increased surface diffusion along the slit boundary, similar to the effect of a parallel array of resistors, each failing in sequence after the failure of the one random resistor, thereby increasing the load in all parallel elements.

The current density in the wire is the primary feature of interest, not the applied potential or absolute current. Electromigration tests for electrical interconnects simulate higher than normal load conditions or temperatures in a variety of ways which can then be extrapolated to draw conclusions about the long term stability of structures. The formation of nanometer junctions requires a deliberate manipulation of this process in order to accelerate the failure in a controlled fashion. A direct current voltage ramp is applied to the wire until the resistance of the wire begins to sharply increase, typically corresponding to the formation of the gap and in some cases quantum conductances as the remaining wire shrinks to several atoms wide. Counter to the typical intuition, the presence of a current limiting resistor (or significant contact resistance) has been shown to significantly increase the final gap size in the created nanostructures [79, 80, 81, 82] rather than protecting the device. This can be simply understood by realizing that the junction resistance increases quickly during elec-

tromigration, and if there is a large series resistance external to the wire then the voltage fraction across the junction, as well as the power dissipated there, will increase sharply as well, independent of the controlling electronics. This can cause a runaway process and break the wire catastrophically, with huge gaps of micrometers and very high temperatures (close to the melting point of the metal itself).

In order to control the breaking of the wire, as well as maintain a relatively constant temperature in the gap, a feedback controlled electromigration technique is used [83]. The voltage across the wire is increased in a gradual fashion (1-10 mV/s) until the resistance increases by some percentage or discrete amount, the applied power (or voltage) is then reduced, dropping the temperature across the gap abruptly and ceasing electromigration. The voltage is then ramped and the process repeated until a target size is reached. The gap size is typically estimated from the tunneling resistance, with a resistance of 1 GΩ in a gold junction for a nanometer gap with an exponential decrease in conductance below this point[84]. This method has been used by many authors to create well controlled gaps ranging from multi-atom contacts with a quantized conductance to large breaks of 10 nm and up. There is evidence that active control of the electromigration process is not crucial as long as the series resistance is very limited [81] however in the experiments presented here it will always be used. An example of the active feedback control is shown in Fig 3.2(a), each vertical jump represents an electromigration cycle where the power is reduced after some increase due to migration in the wire.

Lastly, estimations of the temperature of the wire are useful, but difficult in practice. As will be shown below, during the initial stages of electromigration there is a gradual increase in resistance in most samples due to Joule heating of the wire. In practice the resistance increases between a few and tens of ohms for a temperature increase of tens to hundreds of degrees. The resistance increase is due to electron-phonon scattering, and at these temperatures is linear,

$$\frac{\Delta R}{R_0} = \alpha \Delta T \tag{3.2}$$

where α is the temperature coefficient of resistivity (or resistance), R_0 is the reference resistance for which the measurement is taken, and δT the different in temperature from the reference value. This can be used to estimate the temperature change in

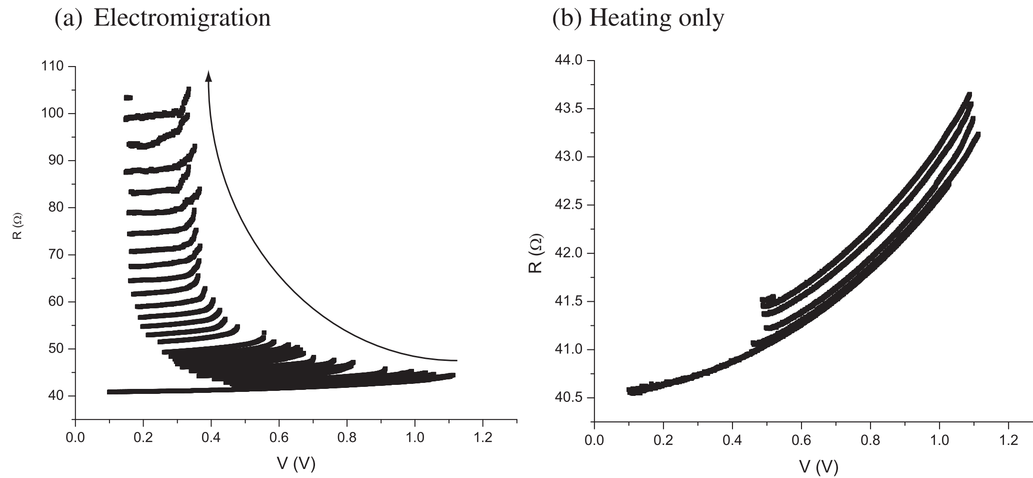

Figure 3.2: Active feedback controlled electromigration, (a) Electromigration cycles for gold on silicon, time sequence indicated, (b) Pre-migration joule heating of the wire, several cycles shown. Slight increases at the start of each cycle are residual temperature effects that typically relax with a full cycle. (all electromigration data for gold and palladium measured with D. Stoeffler)

the wire up to migration, if the wire structure is not significantly changing and if the initial resistance of the wire alone is known. The difficulty lies in knowing this initial resistance without knowing the contact resistance, which in many cases is unknown unless a four point measurement of the wire is performed. A partial solution to this problem is to calculate the temperature with the predicted bulk or thin film resistivity rather than the observed contact resistance, this will be discussed for each material below.

Aside from the temperature, the current density is the primary measurement parameter. Typical voltages are 0.5-10V for these geometries, with observed current densities between 10^{10} and 10^{12} A/m^2.

In order to evaluate the merits of electromigration in creating suitable junctions for molecular measurements a series of wires created using e-beam evaporation on oxidized silicon, stencil deposition on oxidized silicon, or stencil deposition on KBr will be discussed. Wires fabricated from gold, tantalum, and palladium were measured, and the breaking process observed both before and after using a combination of AFM and SEM in UHV and under ambient conditions in an attempt to understand the process. No difference was observed for similar samples prepared or measured in or

out of UHV, suggesting that either surface diffusion effects are minimally important or the effect of potential contaminants are less important than electromigrative or stress induced effects. All e-beam prepared samples were created at the University of Karleshruhe in collaboration with Dr. Regina Hoffmann and Dominic Stoeffler, and measured in the JEOL system with D. Stoeffler.

3.2 Sample preparation and handling

Samples patterned on silicon were mounted on an alumina oxide base with silver epoxy H20E (Epotek) or glued directly to the sample holder, with the electrical contacts to the nanowires created using 50 μm gold wire and conducting silver epoxy cured in air at 150 ° C. Potassium Bromide samples were either cleaved and fully prepared in UHV, or cleaved in air and the metal evaporated in high vacuum using a thermal evaporator (Thermionics VE-90) to prepare gold electrodes or wires, or sputtered to prepare the Ta wires.

All electrical measurements were performed with a Keithley 2400LV sourcemeter controlled through a USB GPIB interface using one of the Labview 6036E NI-DAQ cards to both read the measured current and output the voltage to the device. The feedback control software for Labview was originally developed at the University of Karlesruhe in the group of R. Hoffmann, and then modified to improve the feedback conditions here by D. Stoeffler and S. Fostner.

Electromigration of wires with dimensions of several hundred nanometers or less, whether in air or UHV, presents several difficulties which can lead to the premature destruction of the wire or junction. A number of samples were destroyed at various stages of the electromigration process, both prior to measurement or during the electromigration process. The primary problem is that of random electrostatic discharges (ESD), even a relatively small voltage difference created during handling can create large current due to the very small wire sizes and resistance, typical cross-sections are 10^3-10^4 nm^2, $R = 1$-$100\ \Omega$. In order to try to minimize this, samples were transported with the two contact terminals shorted together directly. In the UHV system this means shorting the two contacts both in the preparation chamber and in the main chamber. During transfer into and between the chambers this was generally not a

problem.

While imaging in the main chamber samples were also sometimes destroyed by electrostatic discharge for unknown reasons. In order to characterize samples, they were imaged using AFM in FM or tapping mode in UHV before, during, and after electromigration though not while actively passing a current through the sample. This gives a better view of the local grains in the wires than SEM imaging but it was often observed that samples failed unexpected after the start of electromigration during imaging. It is reasonable to assume that in the partially migrated state the wires are both thinner and more sensitive to the local potential, the typical contact potential difference during AFM may cause a sudden spike in the local sample potential if not compensated and thereby destroy the junction. This might be compensated dynamically using kelvin probe AFM (KP-AFM) which uses a small secondary voltage oscillation to the tip to minimize the tip-sample potential difference. In other cases this failure was observed simply during the process of changing tips, potentially due to static discharges to the chamber itself.

The precise failure mode is difficult to determine, but typically one of several events can occur:

- a slit forming on the wire or significant mounding but a small gap similar to or smaller than the grain size

- a larger gap on the order of hundreds of nanometers with the wire totally destroyed in some cases

- a catastrophic failure with the wire gone and obvious local damage to the oxide or nearby leads

For the sake of clarity, all experiments will be referred to as electromigration, though in fact in some cases little or no actual migration may be taking place and the breaking process is entirely stress induced.

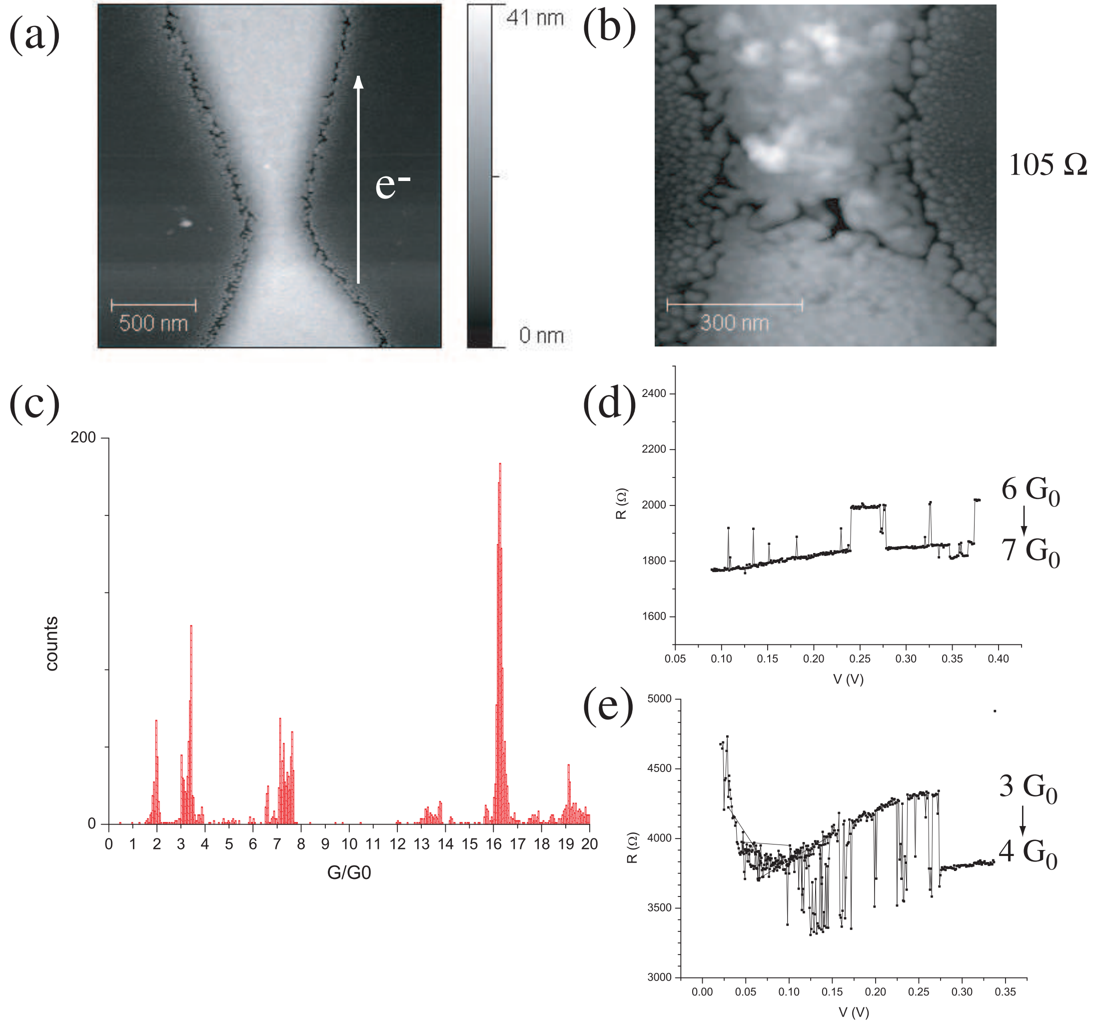

Figure 3.3: Gold wire evaporated on oxidized silicon ex-situ (in a high vacuum evaporator) with no adhesion layer, using a bowtie stencil, (a,b) Images taken using tapping mode AFM in UHV, before and after the first migration cycles, 41 to 105 Ω. Visible mounding on the downstream side of the electronic current is indicated (upper electrode). (c) Histogram of multiple migration curves, with the corrected resistance shown. Peaks in conductance near multiples of the fundamental conductance quantum are smeared out or shifted due to heating and other effects. (d,e) Resistance jumps for migration cycles close to the wire fully breaking, clear jumps between conductance regimes are indicated.

3.3 Gold wires

Gold is the metal of choice for electromigration experiments, it has a low resistivity, 2.214 $\mu\Omega$ cm at room temperature, low melting point, 1064.2 ° C [4], and is chemically inert which prevents the possibility of oxidation or other reactions occurring. The poor adhesion on both KBr and oxidized silicon means that as with contact electrodes the film thickness needs to be 20-30 nm or more. The low resistivity is actually a hindrance, as gold has in fact higher electromigration stability than many metals, but its common use in numerous research applications with its well known functionalization chemistries makes it attractive nevertheless.

Two particular types of gold samples will be discussed, large stencil deposited gold samples in a bow-tie configuration with polygranular wires (ex-situ thermal high vacuum evaporator at McGill, then transferred to UHV), and e-beam patterned gold samples close to a bamboo structure (prepared using standard e-beam microfabrication ex-situ in Karlesruhe, including wet and dry chemical processing, and then transferred to UHV).

First, a gold wire was deposited using the bow-tie silicon stencil described in 2.4.1 with 30 nm of gold onto an oxidized silicon sample, then moved into UHV and indirectly heated at 150° C for one hour to remove adsorbed water. The dimensions at the neck were 310 ± 20nm wide and 30 nm tall, with a total length of 5 um. The initial measured resistance of the sample was 40.9 Ω . Images were taken using the AFM in Tapping Mode [1] TMat intervals during the initial migration process, however the bulk of the slit formation in the structure took place in the first 60 ohm increase in resistance. Thereafter no visible alterations in the grain structure around the break or nearby was visible. The wire structure immediately before and after the migration process is shown in Fig 3.3, a clear crack propagates through the width of the wire largely along grain boundaries but through some grains in the center of the wire, where the temperature is expected to be maximum and direct diffusion of material within grains may become possible rather than along the boundaries.

The grain size of the sample is 22 ± 2 nm, which is consistent with the minimum film thickness required for continuity. The wire is clearly polygranular, and no visible

[1] Using electronic q-control damping as discussed in Chapter 1

thinning of the wire is observed except where the critical voids are formed. What is interesting to note is the complete lack of subcritical voids forming in the nearby regions of the wire. Typical electromigration measurements of similarly sized interconnects show signs of wear, with small voids forming as grains move but then remaining fixed as the slot is formed and propagates quickly across the wire [74]. The cause is likely the presence of the constriction in the wire, the current density is significantly enhanced in this region with a rapid falloff elsewhere. However, as will be discussed, this has also not be observed in wires with a rectangular cross-section, such as Pd. The measured current density at the neck of the structure was $2.6 \cdot 10^{12}$A/m^2 in good agreement with expected values, $1.25 \cdot 10^{12}$ A/m^2 [84] and $2.5 \cdot 10^{12}$ A/m^2[67]. The exact location of the junction is not clear from AFM images, even at much higher resolution it is impossible to resolve a gap of several nanometers for a 30 nm high film due to tip convolution effects.

If the bulk resistivity is assumed, using the simple temperature model in Eqn 3.2, the temperature of the wire at the start of migration is estimated to be 630 K higher than the substrate. This is a significant overestimate, but measurements of thin film and nanowire resistivities are typically 3-10 times higher than the bulk depending on the exact grain size and scattering [1] which gives an upper limit on the wire temperature increase of 235 K and a lower limit of 60 K. Both are consistent with other measurements, with electromigration temperatures from 70-250 K above the bulk [1, 85, 74, 81].

An examination of the junction resistance of the sample, assuming the initial resistance is contact or film resistance, reveals the presence of discrete conductance quantization, shown in Fig 3.3(c-e) as is typically observed in ballistic conductance measurements on 1D or 2D junctions. The peak positions are not centered on the conductance peaks precisely, this is a combination of the heating and stress increase of the wire which has a clear effect on the junction resistance, and well known shifts in the conductance quanta. Jumps between two different conductance quanta are clearly shown in (d) and (e), though in each case there is a clear but slight shift from one or the other of the respective quanta and fluctuations do not always reach either maxima.

The second type of gold sample was fabricated using e-beam lithography and sput-

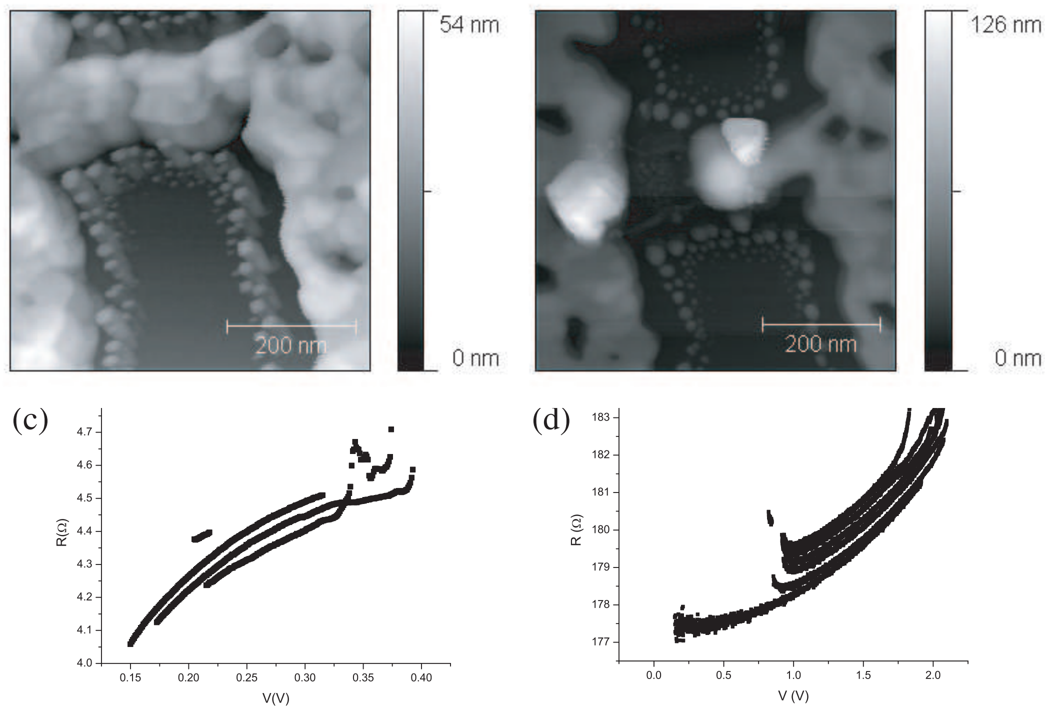

Figure 3.4: E-beam pattered gold on oxidized silicon, 31 nm thick, (a,b) Before and after migration images by tapping mode AFM, (c,d) Two of the migration cycle sets at with very different resistances are shown (same wire), large fluctuations observed are thought to be variations in the position of metallic clusters. Doubling of features in the vertical direction are a result of a clear double tip, a result of tip changes due to picking up metallic cluster which is a common problem while imaging small metallic features.

tered gold. As shown in Fig 3.4 (a,b), the bridge dimensions are considerably smaller, with a bulk wire of 108 ± 2 nm, a minimum bridge size of 62 ± 5nm and a thickness of 31 ± 2nm. The reduced bridge size means the geometry may be closer to a bamboo structure and thus more difficult to fully migrate. This agrees with the measured current density, $4.9 \cdot 10^{12}$ A/m^2, or 1.9 times larger than the polygranular wire. This current density is calculated using the nominal width at the right hand side of the wire, and could be as much as two times too small or large particularly as the wire broke on the left unexpectedly. The wire was not fully migrated, soon after a visible onset of electromigration an AFM image was attempted and the wire spontaneously broke, with a gap size of nearly 100 nm. However, the structure of the gap was relatively smooth, with little or no visible oxide damage and no residual gold grains in the middle. The gap is formed on the side of the wire opposite the regions which appear to have the smallest diameter in the AFM images though this determination is complicated by the clear tip convolution shown by the doubled features in the vertical direction. Post migration the wire appears smoother, and similar to SEM images (not shown), though this is partly due to the taller region created by mounding during the break as well as the presence of a different tip.

Due to the small resistance of the junction, very high currents are obtained at some points, as large as 90 mA, which are 10 times larger than the currents required to break the junction. This is thought to be a result of the dramatic changes in the positions of individual gold grains or atoms which make up the fine scale of the contact, creating significantly larger current paths at some points which are capable of sustaining larger voltages with a similar power dissipation. However, it could be an indication that the failure current is much larger than expected, and that which was observed near the failure point is an underestimate due to the wire having already changed its internal configuration.

The resistance measured during the migration process underwent frequent jumps, varying between 4 and 180 Ω generally. The final migration took place from 182 Ω , which is similar to another sample on the same wafer which began to migrate at 177 Ω . A resistance of 180 Ω , assuming a thickness of 31 nm and a length of 22 nm, close to a single grain wide, would require a width of 0.1 nm at bulk resistivies for agreement. While a gross estimate, even with an expected increase of the resistivity by two orders of magnitude this would mean a small connected neck of less than

half a single grain size. This is plausible, and may account for the nearly identical resistance immediately prior to breaking in each case.

The small size of the wire also supports the previous estimate and is likely the cause of the frequent fluctuations, with both the thickness and width comparable to the grain size in places, even small shifts in the position of atoms near the grain boundaries can cause dramatic changes in the resistance of the wire. Several examples of this are shown in Fig 3.4 (c,d), between jumps the resistance is reproducible from cycle to cycle. The dramatic resistance changes also make a firm temperature estimate difficult, but during the final cycles, shown in Fig 3.4 (d), the resistance increase of approximately 3 Ω would lead to a temperature of 1400 K. If the increase in bulk resistivity of up to ten times is taken into account, expected for a wire of this dimension, a temperature increase on the order of 140 K is obtained, though the uncertainty is difficult to estimate as the actual junction dimension cannot be readily estimated from the AFM images.

3.4 Pd Wires

As a further test of the electromigration process under these conditions, several Pd wires were patterned using e-beam lithography on silicon. The metal is not of particular interest for the junction measurements here, but some insight can be gained into the electromigration process. Of the samples examined, two showed clear evidence of electromigration, referred to as b2 and b4. In both cases the wires are rectangular, with dimensions 250 ± 10nm wide by 320 ± 20 long and 32 ± 2 tall for b2 and 360 ± 10nm wide by 270 ± 20 long and 35 ± 2 for b4. The initial resistance of the bridges was 525 and 407 Ω for b2 and b4 respectively. While the resistivity of Pd (10.54 $\mu\Omega$ cm [4]) is five times that of gold, it does not explain the significantly increased resistance in both samples, which may be a result of the contacts between external leads, electrodes, or the wire itself.

The result of the electromigration process in b4 is shown in Fig 3.5. Unlike the gold case, no clear conductance quanta are observed, instead the wire makes an abrupt break, first to 266 kΩ , then further widening to break completely. The structure of the breaking process is also dramatically different than with the gold wires. No large

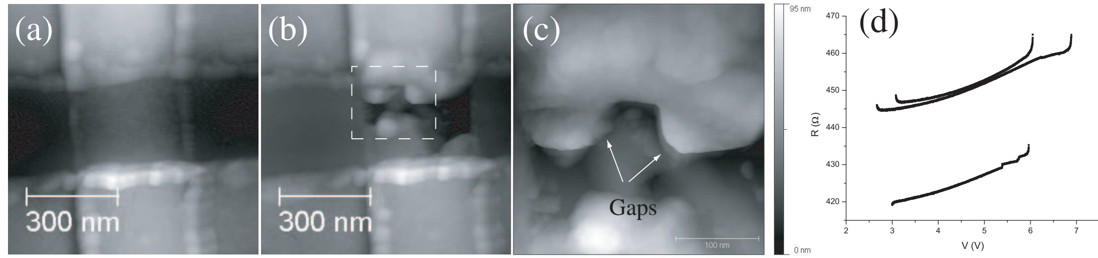

Figure 3.5: Pd wire electromigration (a) Unbroken wire, 35 nm tall, with ridges adjacent to the wire due to the patterning process, (b,c) Broken wire, with the near contact region shown right, arrows indicate the assumed junction points. (d) Final electromigration curves (truncated), with discrete steps showing but well above the quantum limit.

gaps are observed, and a minimal gap size of 3-5 nm at most can be inferred from the AFM images, but there is no clear slit formation. The gap instead forms a wedge structure, which is consistent with void formation in single crystal or bamboo like interconnects [86, 38]. The lack of void formation, and the presence of the slight side wall which is a result of the e-beam deposition lift-off process suggests that voids at the edge are unable to form in a gradual process and that minor imperfections in the sidewall of the wire rapidly propagate to form the opening. This is one advantage of the stenciling process, as no lift-off is required. The measured current density of 10^{12} A/m^2 is somewhat smaller than the gold case. Examining the failure region more closely with repeated afm measurements, it is again not obvious where the gap is formed.

Electromigration in b2 occurred in a similar fashion, a typical resistance increase due to the effective heating was observed over several volts applied potential, followed by a sharp rise in resistance with no quantization observed. No visible crack was observed in the wire despite careful AFM measurements, suggesting either a crack too small to be observed or that the crack lay close to either electrode. The latter seems mostly likely, but there is no visible mounding or notch formation. A measured current density of $4.6 \cdot 10^{11}$ A/m^2 was obtained. Unlike the previous case, there is no ridge to the side of the wire, and the lower current density may be a function of this. As well, the wire is 19% longer, and 31% thinner. Beyond a typical threshold width, generally 200 μm for gold wires, the failure current density saturates at a minimum, so this is unlikely to be a significant effect, however the failure current is inversely

proportional to the length which may account for part of the decrease in the failure current [1]. A lower failure current than gold is expected on general grounds, similar to studies done examining the failure current density for thin film interconnects [87].

Based on the resistance increase prior to the breaking point, the temperature as estimated from the bulk resistivity is 2000 and 4600 K for b4 and b2 respectively. Assuming the resistivity is 6 times higher than the bulk, estimated from the film thickness and wire length effects, it its not unreasonable to assume a temperature of just over 300 K above room temperature for b4, higher than gold but not excessively. The large increase observed for b2 is more difficult to explain. The discrete steps in the breaking curve for b4, Fig 3.5(d), are frequently observed well prior to the migration point but are not well understood, they are however a common indicator of the onset of electromigration and are thought to be associated with material rearrangement as the wire junction forms.

3.5 Tantalum wires

As discussed in Section 2.5, tantalum was originally chosen as a wire material due to the registry with KBr and the possibility of much thinner electrically connected films. From a deposition perspective this was attractive, but as a metal tantalum poses other difficulties, particularly in terms of creating small scale gaps. The bulk resistivity of tantalum at room temperature, 12.2 $\mu\Omega$ cm [4] is almost six times larger than that of gold but only slightly larger than that of palladium. As well, tantalum films are significantly stressed on deposition [5, 11] with typical film stresses of 1 GPa on silicon. The film stress as deposited on KBr has not be measured, but visible deformations and bending of the deposited wires suggests a significant film stress as well.

Deposited metal wires were created on ex-situ cleaved KBr samples using a sputtering source, or in-situ on UHV cleaved KBr samples using an e-beam evaporator and silicon stencils, typical results are shown in Fig 2.14. In both cases the wire morphology appears similar, with similar stress features visible under SEM, but the sputtered Ta samples are significantly larger, for wires 5 μm wide the deposited Ta structure can be as large as 25 μm . This broadening is not strictly geometric as in the UHV stencil

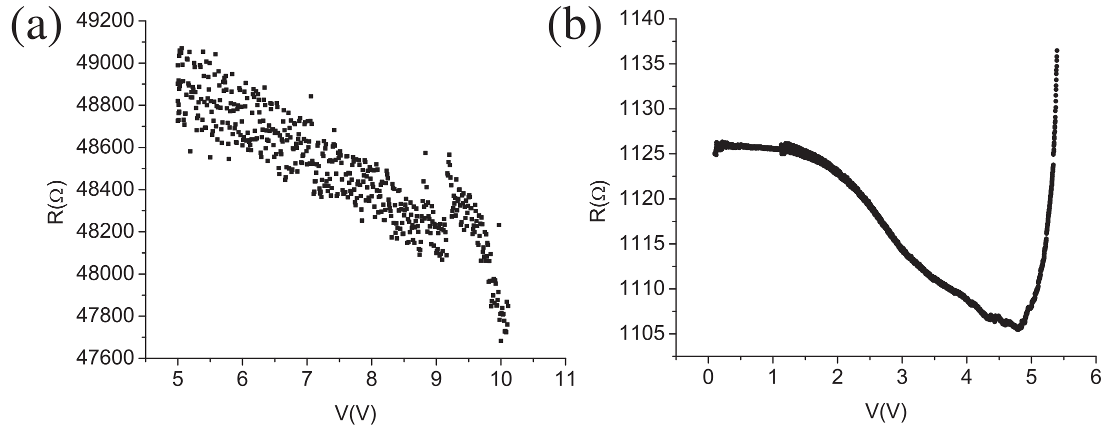

Figure 3.6: Ta electromigration curves, both show a similar decrease in resistance, (a) UHV deposited sample, high initial resistance leads to larger than usual fluctuations in the resistance (b) Ex-situ Ta wire, resistance spike is not the breaking point, but occurs at a similar voltage to the next break, and is likely the breaking of the first of two parallel wires (not shown)

case, but a result of the sputtering method itself which is much more sensitive to the stencil and sample spacing. This is a result of the residual gas required for sputtering which eliminates the purely ballistic trajectory of vacuum deposited materials. The sputtered samples were used as tests for the first electromigration experiments and later refined. Handling issues were even more significant than the silicon mounted samples described above, with at least half of the samples failing catastrophically due to ESD during handling, particularly stencil deposited samples on KBr.

Of those samples in which electromigration was attempted, no visible quantization was observed, much like the palladium wire measurements described above. As well, in all but a single case, the typical Joule heating curve was not observed. As shown in Fig 3.6, the resistance typically decreases with applied voltage, between 14 and 21 Ω . This makes an accurate estimate of the wire temperature impossible based strictly on the resistance variation.

The breaking characteristics of the tantalum wires also proved to be very different, the large Ta wires failed almost explosively, with films rupturing from the center outwards or along stress lines as shown in Fig 3.7. Initial wire resistances were also much larger, 1.1 - 2.8 kΩ , with the UHV wire much larger at 55kΩ (due in part to the smaller dimensions but likely also a weak film contact to the external electrodes).

Deposited films were 10-15 nm thick, significantly smaller than the gold films but fully connected. The mechanical wire integrity is nicely shown in Fig 3.8 where a 10nm UHV deposited Ta wire was pinned by an AFM tip crash to the surface and spontaneously broke free during transfer to the SEM. Measured current densities of the Ta wires were $1.2 - 1.6 \cdot 10^{10}$ A/m^2 in all but two cases, which were both $5 \cdot 10^{10}$ A/m^2. This is an order of magnitude lower than the Pd wires, and more than two orders of magnitude lower than gold. Expectations for Ta wires were actually that the electromigration failure current should be expected to lie between Pd and gold [87], but given the severe damage observed, despite the relatively low current densities, it is more likely that little to no actual migration is taking place. The sudden failure along stress lines suggests a stress relief in the films, or a sudden failure as the stress increases to the point of fracture with a moderate temperature increase. The UHV wire, shown in Fig 3.7(e,f) failed at $1.2 \cdot 10^{10}$ A/m^2, despite dimensions of 1.2 by 3.6 μm by 15 nm thick, which agrees well with the ex-situ tests. As before, no visible break was immediately obvious despite a resistance jump to MΩ , however before AFM imaging the wire failed completely.

In some cases, though there are no noticeable voids forming in the wire itself, there is a clear thinning of the exterior of the wire, shown in Fig 3.7(b). This may be a sign that some migration is occurring, strictly on the exterior surfaces of the wire, which is often the case when grain boundary and diffusion along grain boundaries is more difficult than surface diffusion. This effect is more common in bamboo wires, but the tantalum structure seem have an almost bamboo like structure in terms of the macroscopic domains.

The nature of the stress in the original deposited film appears to determine the final fracture point and also limits the size of the gap potentially available. The wire shown with horizontally oriented domains, much like a bamboo structure, failed in such a way that the gap lay between adjacent boundaries, yet several micrometers apart. Wires with a clear change in the film structure between the inner and outer regions of the wire fail quite clearly in the center in most cases, rupturing outwards.

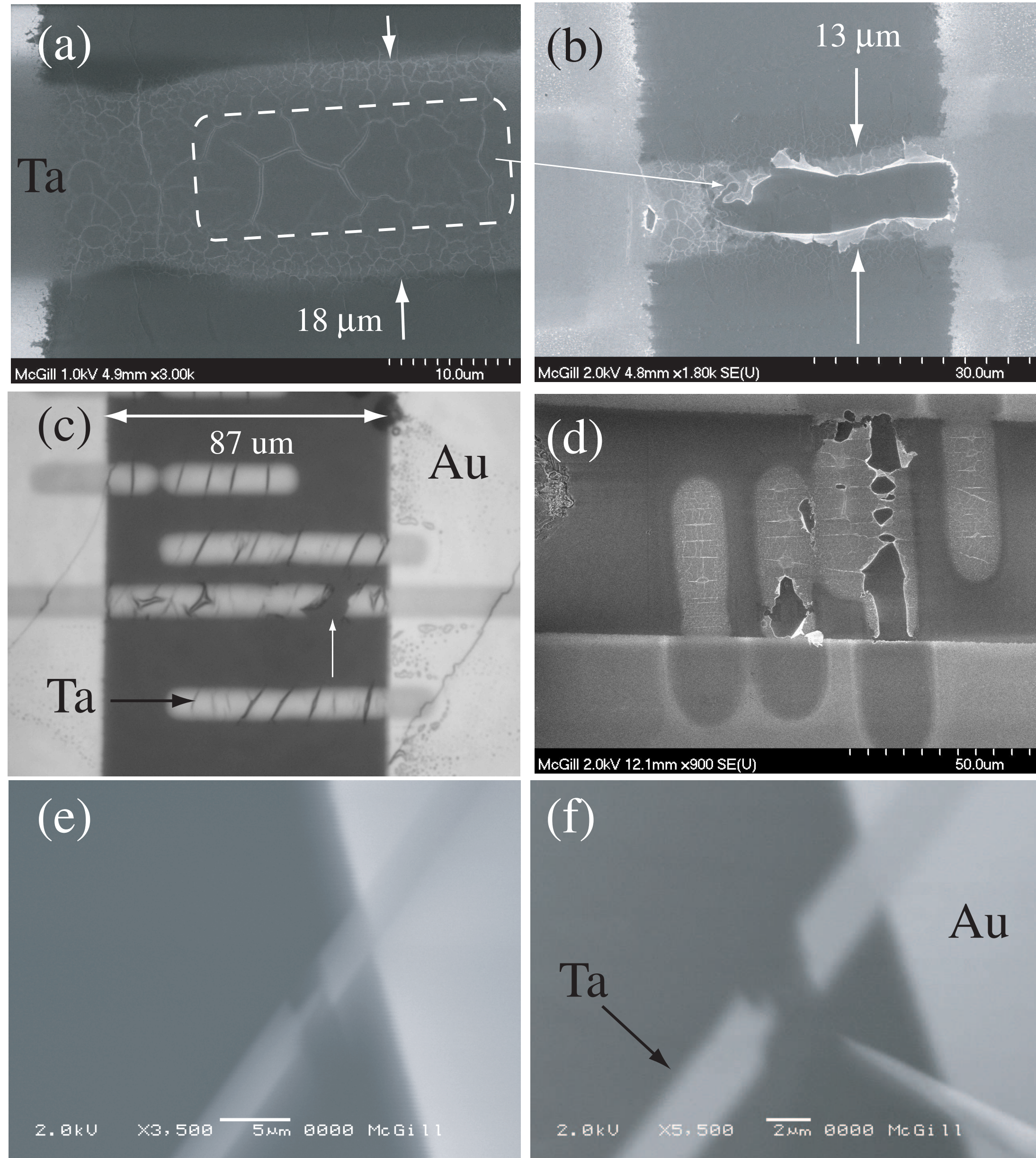

Figure 3.7: Ta electromigration samples, (a,b) Before and after SEM images, broad Ta wire broken from the center, width reduced as shown, (c) Wire with perpendicular stress lines, optical image, (d) Double Ta wire imaged at an angle, (e,f) UHV deposited wire before (e) and after complete failure (f)

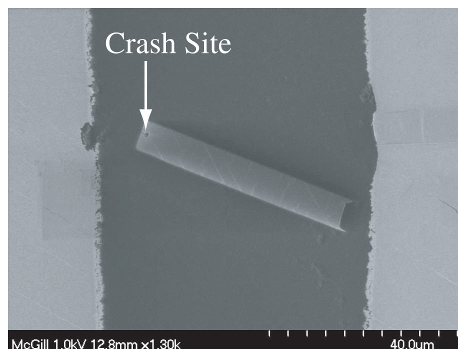

Figure 3.8: Freely rotating Ta wire lifted from the substrate but pinned by an AFM tip crash, shown left.

3.6 Discussion

It is important to consider the goal for these measurements, typical electromigration and molecular measurements employ nanometer size gaps such as those formed in the stenciled gold sample, however in this work a larger gap size would be advantageous in order to perform gold deposition in order to bridge leads and molecules as will be discussed. The gaps formed through electromigration such as slits or microscopic gaps, while suitably sized for molecules are inadequate for careful measurements of the local position and structure of the molecule and metals for structure-function calculations. Different sizes and positions of gaps are possible depending on the electromigration conditions, metals, and geometries.

The information presented above for different material and wire configurations is summarized in Table 3.1. The temperature increases are given but not corrected for the change from expected bulk resistivity values. In general a relatively modest temperature increase is observed, between 60-200 K (assuming 5-10x resistivity increase and if one discounts the upper end of the Pd temperature range), which is in agreement with the literature for similar structures. There is significant uncertainty as the actual film resistivity is typically unknown, but it is clear that the local temperature increase up to the onset of electromigration is well below the melting point of each metal as expected. Changes in the larger Ta wires make an accurate temperature estimate difficult or impossible as the resistance decreases with voltage but the temperature is expected to be similar to that of gold and palladium. The low temperature is important for samples deposited on KBr or similar insulators as the

melting point is 734° C, and damage of the surface will begin well below this point, with significant rearrangement at steps observed as low as 400° C.

Metal	Preparation	$J(10^{10}\text{A/m}^2)$	R_0 (Ω)	ΔT (K)	Failure Mode
Au	stencil(ex)	260	40	630	slit
Au	e-beam	490	4	1.35-1.44k	gap
Pd	e-beam	$50-100$	410-530	1.98-4.57k	slit
Ta	stencil(ex)	$1.3-1.6$	1.1-2.8k		break
Ta	stencil(UHV)	1.2	55k		not visible

Table 3.1: Summarized electromigration data, temperature given from bulk measurements, expected temperature changes are 5-10 times smaller as the thin film resistivity increases significantly, preparation given as e-beam (lithography), stencil (UHV or ex-situ), ρ_{bulk} = 2.214 (Au), 10.54 Pd, 12.2 Ta [4]

In each case, the failure current densities are consistent for each metal, though significantly different from metal to metal. As expected gold is the most difficult to migrate, followed by Pd then Ta, though Ta migration is thought to be dominated by film stress rather then electromigration of material. The significant gaps formed by the Ta wire failure in every case suggests it is unsuitable as a material for this purpose. Wire failure in Ta is observed even in partially connected wires, which cannot be due to a current directly through the wire and may be related to the applied voltage and its effect on the internal film stress.

The most suitable wire material of those examined is clearly gold, with clear microscopic gaps formed between 1-100 nm. Visible mounding supports the presence of electromigration. While electromigration may be easier to observe and cause in polygranular gold wires, a gap on the order of tens of nanometers is readily possible for wires with bamboo or nearly bamboo structure. The movement of a single 20-30 nm grain gives a suitably large gap, for deposition or the deposition of large molecules. Measurements on such small wires can be more difficult due to random oscillations as grains or atomic contacts shift under the high migration current densities. For most wires, particular polygranular ones, the resistance fluctuations that are measured are usually very small until the point of migration and are limited only by digitization effects in the measurement apparatus, on the level of fractions of an ohm for resistances of 10-100 ohms. However for smaller bamboo-like wires, fluctuations can be potentially much larger, with the resistance changing from 4 to 4000 Ω. While the electromigration failure current appears to be larger as expected, this

instability could be a problem for devices formed in small gaps($\approx$ 1 nm), for larger gaps this may not be an issue as long as the residual contact area is relatively stable. As well, smaller wires are quite sensitive to ESD, requiring care not only in handling but during the imaging process as well.

A second consideration on bulk vs thin film insulators is the poor thermal conductivity to the substrate. Measurements on oxidized silicon samples have significantly higher failure current densities with oxide thickness under 20 Å as significant heat is lost to the substrate. This suggests that bulk insulators in general should have little trouble, but if experiments move to MgO on iron then the failure currents may be significantly higher. However, the temperature distribution along the wire may be more uniform. Care will be required to strike a balance between sufficient heating and currents to force migration of the sample but at the same time not damage the thin insulating layer created by the MgO film.

Control over the positioning of the bridge may also be important, rectangular structures have a tendency to break closer to the contact electrodes but the bowtie configuration forces the highest current density at a chosen location in the center. It may also be possible to control the position of the breaking gap using an AFM tip to mechanically indent the surface, or an SEM to locally alter the heating profile directly as has been reported by Stahlmecke [88]. While a relatively small temperature increase was observed in that work, less than 0.025K, this was the result of scanning over the entire wire, 10 μm long and 1 μm wide. With a highly focused SEM beam on the region of interest, for example 100 nm^2, this would increase the dwell time over the region of interest by over 1000 times, potentially as much as a 25 K temperature increase which is enough to significantly affect the breaking of the wire.

In-situ monitoring of the migration process using AFM and SEM between migration cycles is necessary to give the greatest control, while there is some risk of ESD due to the AFM tip it does allow one to stop the migration process at the appropriate gap size. The active feedback control allows the formation of controlled gaps, but in order to create gaps tens of nanometers in size it may be necessary to deliberately stress the wire more than the usual by allowing greater resistance changes prior to the onset of the active feedback mechanism, the addition of a measurable series resistance, or actively increasing the substrate temperature or a nearby metallic tip.

A further advantage of these widely spaced gaps is the lack of possible metallic islands between the electrodes contaminating possible measurements. Such islands have been clearly observed in the past in many break junctions[80, 79] with clear coulomb blockade and Kondo effect signatures giving clear signs of contaminated gaps [89]. With more widely spaced gaps (>10nm), the possibility of anomalous I-V characteristics during molecular measurements is greatly reduced. The effect is noticeably reduced in controlled migration processes with minimal series resistance and mild breaking of the initial wire.

An obvious question of course is whether this process is necessary at all, as demonstrated in Fig 2.9 (d) it is readily possible to create silicon stencils which possess an integrated gap at the outset. Unless the broadening effect of the stencil is significantly less than the gap size, and edge effects and diffusion are minimal, then no gap will actually be observed. Given the edge roughness shown in Fig 3.3, this limits the gap size to the order of several hundred nanometers. Even if not actually bridged, the local gap is likely to be contaminated with many gold particles, similar to those discussed above, with similar effects on molecular conductance measurements. As well, it becomes impossible to measure the local conductance of such a wire prior to the molecular deposition (though connectivity checks are possible with the above methods), leading to significant uncertainty in the DC conductivity.

There are several issues which will need to be resolved in future work. Gaps larger than 5 nm are readily possible, but the best parameters for creating these gaps have to be explored, a time consuming process if done using UHV prepared samples with a week turnaround and no better than a 50% survival rate from ESD, sometimes much less in fact. Proper material choices are critical, gold appears to be the most effective choice despite relatively high migration currents. It is not clear precisely what debris is left behind from the migration process in the gap, for oxidized silicon samples this can be both very small amounts of gold, or more likely damage to the oxide. For bulk insulators like KBr, while the surface can be damaged there is no oxide to remove so residual gold is the primary fear. Imaging with a standard AFM tip may be sufficient to remove these clusters, given the strong affinity for metallic clusters to be picked up during imaging and sufficient time. At present, the few gaps observed appear to be much cleaner than those created through a catastrophic ESD break, with little debris visible by SEM, and a small amount, particularly around the

gap boundary by AFM.

The overall process of wire deposition, electromigration and tip deposition will be discussed further in the conclusions after all relevant experimental approaches have been described in detail.

The next challenge then becomes connecting these widely separated electrodes, for this purpose a series of local metallic deposition from scanning probe tips will be discussed in the next chapter as a possible solution.

Chapter 4

Tip based lithography

4.1 Introduction

Bridging the gap between the electromigrated gaps described previously, and immobilized molecules in nanoscale pits [28] requires a slightly different approach. Using sharp metallic tips it is possible to desorb metal surface atoms in a controllable fashion to deposit them directly under the tip, which can be controlled to within nanometer accuracy. In this fashion one can create wires, contact existing wires, or create metallic clusters on the surface of virtually any material. The only limitations to this process are the material of the tip, the applied voltage, and the tip and sample geometry involved.

The desorption of surface atoms under an applied electric field has been known since the discovery of field-ion-microscopy (FIM) by Muller in the 1950's. In FIM, a large positive potential, typically several kilovolts, is applied to a sharp metallic tip (<50 nm radius) which is cooled, under vacuum, and with a low pressure of an imaging gas. Under such high field conditions a variety of effects occur: the adsorbed gas atoms ionize and are accelerated to the screen thereby forming an image of the tip, atoms on the tip itself can ion ionize and then desorb from the tip in a variety of possible charge states, atoms from further down the shank can diffuse towards the apex of the tip under the influence of the high electric field produced as a result of the tip geometry and applied bias. The latter two cases are of primary interest here,

even in the absence of the rest gas and at room temperature it is possible for both to occur. This was first recognized by Muller [90], and later expanded upon by others including Gomer [91], and Tsong [92, 93, 94]. While efforts on this process continued in the context of the FIM community between the 1970's and 90's, it wasn't until the discovery of the STM by Binnig and Roher [95] that the true potential of field induced desorption was fully recognized. The precise distance control between tip and surface first made possible by STM allowed the desorption of clusters from either tip or surface at much lower voltages than those required for FIM due to the barrier lowering effect of surface and tip potentials, the high fields possible at relatively low voltages, and the increased barrier reduction due to the surface image potential. While some surface manipulation effects were immediately visible to STM users, the conditions for field induced deposition (FID) are not always compatible with typical STM imaging conditions, with higher applied voltages and compatible tip materials. Mamin et al [96, 97] first demonstrated the deposition of gold clusters in a repeatable fashion using electrochemically etched gold tips. This was followed by numerous others, and FID in both AFM and STM configurations has been demonstrated with a variety of metals.

The theory for FID first goes back to Muller in 1956 with what is known as the Image Hump model (IH), later expanded by Gomer, Tsong, and others as an extension of the Charge Exchange model (CE) in FIM. The image hump model assumes that atoms are first ionized and then later escape, with the potential barrier reduced by the formation of a Schottky hump. The charge exchange model later proposed that the desorption of atoms from the surface is ionic, with neutral atoms being simultaneously ionized from their bound atomic state and escaping as whichever ion possesses the lowest potential barrier at the current electric field. For gold this turns out to be the Au^{2-} state in most cases, but this will be addressed later. Both models give quantitatively similar predictions of the deposition conditions, often within 15%[93] of the experimentally observed conditions despite the simplicity of both models, but the CE model has been largely accepted as giving a more accurate picture of the physics of desorption and will be the one used here.

For the neutral bound atoms on both the surface and tip there is a binding energy Λ and a characteristic length scale (typically taken to be on the order of one angstrom). As the tip and surface are brought together, the binding potentials overlap and grad-

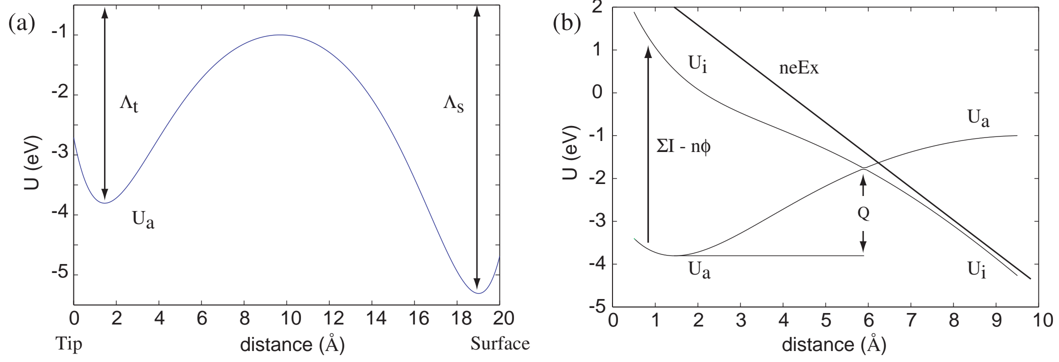

Figure 4.1: Binding energy curves, (a) Atomic binding energy curves, (b) Ionic and atomic curves for positive ions created at the surface of the tip in the charge exchange model, the cross-over point giving the effective potential barrier to desorption.

ually decrease the barrier height as shown in Fig 4.1(a). It should be noted that the overlap distance necessary for this to be a factor is less than 13 Å , with almost zero barrier at 5 Å [94], typical distances for STM deposition but not in the AFM configuration as will be discussed. The binding energy was first calculated by Muller in the IH model, though similar assumptions are used for the CE model, by assuming an Arrhennius distribution for the transfer rate

$$\kappa = \nu \exp(-Q_0/kT) \tag{4.1}$$

where Q_0 is the barrier height and ν the attempt frequency, taken to be $10^{13}s^{-1}$, giving a transfer rate of 1 s^{-1} at 300K for $Q_0 = 0.772$ eV. In practice significantly higher transfer rates are possible as the observed rate is a function of the applied voltage, but this is taken as a typical benchmark for observable deposition rates. The binding energy for gold on gold is typically taken to be 3.78 eV[93], however the specific binding energy of gold on whatever substrate is in use can vary significantly and may in fact be smaller. In the absence of an applied potential the process is entirely thermal, and can occur in either direction with a rate determined by the proximity of the tip and the binding energy. In order to create a specific directionality to the process it is necessary to apply a bias between the tip and sample, similar to FIM.

To determine the evaporation barrier height it is necessary to consider the action of the ionized metal atoms. In order to do this the ionic curve must be considered, as

shown in Fig 4.1(b). In order to evaporate, an atom must first overcome the barrier to ionization, then travel along the ionic curve to the substrate, this occurs at the intersection of the ionic and atomic curves, U_i and U_a at zc. This new barrier height does not correspond to the barrier on either the purely atomic or purely ionic curves, but the energy required to make the transition to the lower energy curve. The ionic potential curve is given by

$$U_i(z) = U_{im}(z) + U_{rep}(z) + \sum I_i - n\phi - neV(z) \tag{4.2}$$

where U_{im} is the image charge potential created by the creation of an ion just outside the tip, U_{rep} the potential of the ion surface interaction, I_i the ionization energy per atom, n the charge state, and ϕ the work function of the material as the ionized electrons are regained by the tip. The energy needed to create the ion just outside the surface of the tip is independent of the applied field, which is represented here in terms of the external potential applied to the tip, but is conventionally given by $neEz$, where E is the applied electric field. As the tip distance d is much smaller than the radius for the STM case, it is conventionally taken to be a simple parallel plate capacitor. In this work that will not be the case as the geometry and distances are very different from STM cases. However, even for AFM distances of several nanometers, that approximation can sometimes still hold. The image charge potentially takes a variety of forms. The simplest approximation, originally used by Tsong, Muller, and Gomer is to again assume a parallel plate capacitor with a point charge a distance z from the surface of the tip and $(d-z)$ from the surface of the substrate. Considering a single image charge on each side, and integrating to find the potential gives the Schottky image potential

$$U_{im} = -\frac{n^2e^2}{4z} - \frac{n^2e^2}{4(d-z)} \tag{4.3}$$

where the first term is the contribution due to the tip, and the second the contribution due to the sample. This neglects secondary contributions from the infinite array of image charges present, but depending on the distances involved the difference is minimal. A more complete form of this is given by Binnig [98]

$$U_{im} = -\frac{(ne)^2}{d}\left((ln2-1) + \left(\frac{z-d/2}{d}\right)^2 + \frac{d^2}{d^2-4(z-d/2)^2}\right) \tag{4.4}$$

and later used by Tsong[94], and Mamin [97].

From Eqn 4.2 and the atomic potential, assumed to be strictly a repulsive potential similar to that in Eqn 4.2 one can calculate the barrier for desorption as the intersection of the two curves. The intersection is typically taken to be one atomic radius as the validity of this model does not hold well for distances smaller than this. Similarly, the repulsive potential is replaced by a the binding energy of the metal, Λ, assumed to be the same magnitude at the intersection point. Putting these together gives the barrier for desorption in Eqn 4.5.

$$Q = \Lambda + U_{im}(z) + \sum I_i - n\phi - neV(z) \tag{4.5}$$

The theory given above discusses strictly the case of positive ions, but an analogous form is possible for negative ions, replacing $\sum I_i - n\phi$ with $n\phi - \sum E_a$ where E_a is the electron affinity for the metal as electrons are removed from the surface and the atoms must be reduced instead of ionized.

It has been assumed until now that the desorption process is taking place between two metal surfaces in close proximity, originally motivated by the FIM configuration and later STM. In order to account for the presence of an insulator, critical for situations such as AFM where the deposition may be over either and insulator or metal, or in many cases over an insulator covered metal, modifications are required. This was first described by Hosaka and coworkers [99], in which the conventional Schottky image potential is modified by the presence of a dielectric ϵ over the surface of the substrate. As a result the image potential becomes

$$U_{ins} = -\frac{n^2e^2}{4z} - \frac{n^2e^2}{4(d-z)}\frac{\epsilon - 1}{\epsilon + 1} - \frac{n^2e^2}{t} \tag{4.6}$$

where t is the thickness of the insulating layer (assumed $\gg d$), and the second term is the image potential in the insulator itself. The electric field is similarly weakened, but in the case given here a different approach will be used.

In the case of a geometry where the metallic counterelectrode is not under the overlayer, see Fig 4.2, the geometry and fields are much more complicated. For instance, a metallic electrode with a tip above an insulating surface but not necessarily directly over the electrode is of primary interest in these experiments. This poses a number

of complications. First, the image charges are no longer readily calculable, in order to use simple image charge methods a degree of symmetry is required. As will be discussed in the next section, this may not prove to be a significant problem, only the tip and insulator image potentials become relevant. Secondly, the parallel plate approximation is no longer sufficient to calculate the electric field, and in fact there are no simple analytic forms for this sort of geometry that the author is aware of. As a result, numerical methods, specifically the finite element method, have been used to calculate the potential difference between the tip and surface. In this way one does not even require the electric field, typically in such configurations the potential is well known but the electric field much less so. The major difficulty with such methods is the degree of confidence in the simulation, a sufficient mesh density will eventually converge to the exact solution but for a non-infinite mesh results can off in such a way as to be difficult to quantify. Hence the results in the following section will be at best a guide, giving the approximate variation in potential between tip and surface and the rough electric fields for comparison to cases in the literature.

4.2 Electrostatic Modeling

A complete description of the finite element method (FEM) is unnecessary here, but a brief introduction will help to motivate this discussion. A better description is giving in a number of sources, for instance Agbezuge [100]. The essence of the problem is taking a partial differential equation, in this case Poisson's equation,

$$-\nabla \cdot (\epsilon \nabla V) = \rho_f \tag{4.7}$$

and discretizing it over some domain. In most cases discussed here, there are no free charges in the original conditions, however due to the vacuum solid interface it is necessary to account for the change in dielectric function between the two regions. This has a significant impact in both the potential distribution and the electric fields, even those far from the electrode edge.

The simplest such approach of course is to take the domain, and divide it into rectangular regions and use a simple finite difference to calculate the solution, which is a form of the finite difference method. Obviously, a simple linear division of the grid

becomes computationally unfeasible very quickly. In order to circumvent this problem, one needs to be able to discretize the mesh to a higher density over regions of particular interest and at the same time retain a low density mesh in other regions to keep computation time down. This notion of adaptive meshes is not limited strictly to FEM, but is especially useful as there are few restrictions on the boundary or mesh type. Typical 2D and 3D meshes are formed using triangular or tetrahedral meshes in a variety of methods, this being the simplest shape in which it is possible to decrease the mesh size between elements yet still form a continuous structure with single element boundaries between each triangle (unlike the rectangular grid). Each mesh element contains a specific value for the solution but adjacent nodes need not, and in fact cannot, be continuous. In order to calculate the solution on this grid, an approximate form of the differential equation is needed. The original equation is linearized by multiplying it with some weighting factor, and then rearranging and solving on some subset of the original problem. The resulting equation is linear, and gives the solution of the original PDE on the nodes of the discrete solution. In this form it is numerically possible to solve the system as it is reduced to a matrix problem, $KU = F$ with U the matrix of the grid values of the variable in question, in this case potential, and K and F related to the coefficients of the original equation.

At a user level, there are a number of both free and commercial packages created to solve a variety of FEM problems, either in isolation or in tandem. The initial mesh generation has been done using Gmsh, a free mesh generation software by C. Geuzaine and J.F. Remacle. The FEM solution was calculated using Elmer, an open source FEM multiphysics solution package created by CSC, a non-profit Finnish organization for academic support and research. Solutions calculated using Elmer were then examined in several ways. The most computationally effective solution was to take a direct 2D slice of the data using Paraview, an open source visualization package, and then analyze the resulting points from this plane in Matlab using the Delaunay triangulation tools and $Triscatteredinterp$ to interpolate the scattered data points to a rectangular grid for plotting or analysis. It is also possible to take the original data from the FEM solution directly into Matlab, however the size of the original dataset, typically one to two million mesh elements, means that interpolation of this full 3D data (rather than a 2D slice) becomes problematic. It is also possible to calculate the FEM solution of the 2D problem directly within MATLAB using the PDEtools toolbox. In this case it becomes possible to better discretize the dataset,

but much more difficult to account for asymmetries into or out of the plane of the original solution. For this reason, most of the simulations performed were done using the full 3D model. The basic geometry is shown in Fig 4.2 (left), the tip is modelled as a square cone with an apex sphere of 30-50 nm over a KBr surface with a 10 nm electrode. The electrode and tip are voids in the model with the potential fixed at the boundary of each, as well as the outer square region. The top of the tip geometry is formed with a gap at the top to maintain the boundary continuity.

In order to model the fields in the region near the tip apex, there are a number of fields defined in gmsh to locally force the mesh refinement level, the max mesh size is 0.25 nm within the apex region, 0.5 nm in the vicinity of the tip and 5 nm outside of this range. Regions in the simulation well away from the surface use a very coarse mesh, 50-100 nm, but this has little effect on the critical region. These mesh parameters were taken to give a fine mesh density in the vicinity of the tip (at least 4-5 points for a spacing of 1 nm which is the smallest used and much more for large gaps) but keeping the final mesh file size between 40-100 megabytes (larger fails to run correctly in elmer, likely due to limitations of the hardware). An example of the geometry and a full mesh is shown in Fig 4.2, however the final level of mesh refinement is not visible at this scale. The potential is taken to be 0 on the external boundary and the electrode, and -40 V on the tip (or $-40 \cdot 10^9$ V in the model to correct for scaling as the units are taken to be nanometers rather than meters). The dielectric constant of KBr at room temperature is taken to be 5.65 [101]. It is assumed that there are no free charges in the simulation, and any deformation of either tip or substrate is neglected. This is not wholly correct, at such high fields one would expect a slight deformation of the tip, but only fractions of an angstrom which is much less than the current tip sample separation.

The simulation procedure is as follows, the mesh is defined and meshed in gmsh using a predefined definition file. The resulting mesh file is imported to elmer, and all the physical variables, boundary potentials, and dielectric constants are defined along with the electrostatic equation. Upon meshing, the results are exported to a vtk file, for analysis as described above. The physical position of the tip is then changed in the gmsh definition file, and the process repeated for each tip position. Two tip sizes were modeled, 30 and 50 nm diameter, at distances of 1, 3, 5, and 10 nm from either the surface, or the top of the electrode. These distances are used as they are

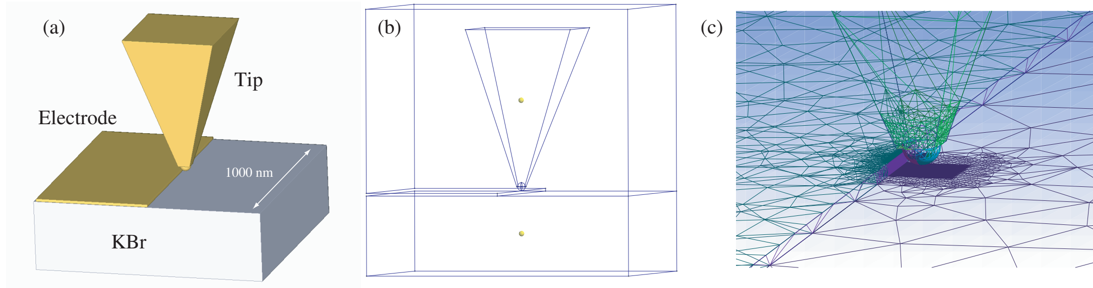

Figure 4.2: (a)Schematic geometry, (b) Model geometry in gmsh, full scale size is 1000 nm with a tip size of 30 or 50 nm. The rectangular void on the left forms the bounds of the electrode pad. (c) Sample 2D mesh near the tip and electrode edge. Three levels of mesh refinement shown (max element size, some are smaller), 100 nm, 5 nm, 0.5 nm (0.25 nm not shown, directly below tip)

the approximate range for which the process is typically attempted using AFM tips, larger separations have been used but the question in this case is whether there is a threshold for evaporation at these particular voltages near a pre-existing electrode.

To calculate the potential barrier as given by Eqn 4.5, it is necessary to have the potential as a function of distance near the tip. Using the models described above, the potential slice passing through the tip was used to calculate a line profile of the potential which is then evaluated at $r = 0$ (the tip) and r_0, the assumed point of desorption from the tip surface. As the tip sample distance in this case is much larger than the typical STM distances, nm vs Å , and given the lack of a clear counter-electrode below the tip, the potential is not simply a linear function in most cases and the electric field is not necessarily constant. In order to calculate the contribution due to the image potential for a tip over the insulator, a modified form of Eqn 4.3 is used, where the second term is scaled by $\frac{\epsilon-1}{\epsilon+1}$. Given the large distances between the tip apex and the electrode, typically on the order of a tip radius or larger (20-30 nm), there is assumed to be no contribution to the image potential due to image charges on the electrode itself. This is supported by a simple calculation of the form given in the first half of Eqn 4.3, with a distance of 200 Å we find a contribution of 0.07 eV. As discussed above, a desorption event is assumed to occur at r_0, which is also taken to be the minimum of the binding energy curve, or Λ_t. The binding energy for gold on KBr is not known, as far as could be determined, but it is a reasonable assumption that it will in fact be lower than the 3.78 eV used for gold. As long as the tip sample separation is large this is not a problem, the atomic curves for both tip and sample

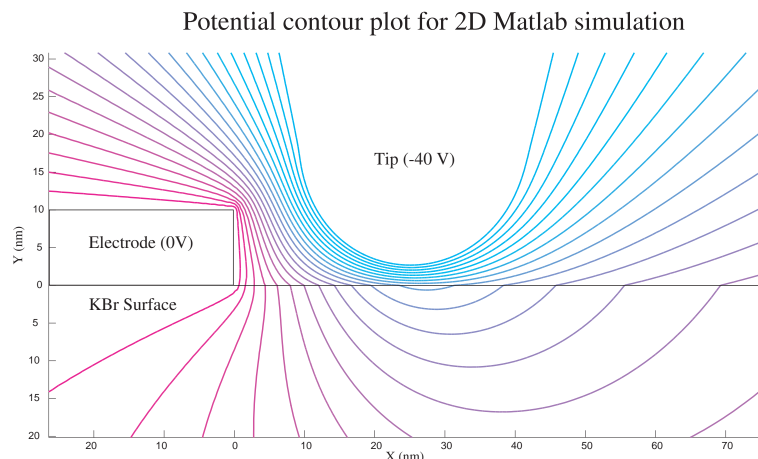

Figure 4.3: Contour plot of the electric field lines for a 2D model of the potential around a circular tip and 10 nm tall electrode (zoom near the tip, simulation area 1 μm across in both directions), -40 V applied to the tip.

will not overlap to any appreciable degree and the desorption process will be entirely determined by energetics at the tip. It should be noted though that this implies that the reverse process, removing gold atoms or clusters from the surface of the sample is not only possible but in fact highly probable with certain tip voltages. This has not been directly observed, though the removal of small metallic islands from surface to tip is common during imaging alone which would complicate the observation.

An example of both the potential contours and the approximate fields are shown in Fig 4.3 and 4.4. The electric field gradient is typically maximal at the apex of the tip between it and the surface, though as seen there can be high fields present at sharp edges such as that of the electrode. In practice the electrode edge will be significantly more rough than this, with large variations in the local structure as shown previously.

The potential drop and the one dimensional derivative is given in Table 4.1 as well as the various geometries attempted. The electric fields are not expected to be fully accurate but they give an order of magnitude of the the expected fields. These fields, between 0.6 and 5.4 V/Å are of the correct order of magnitude for deposition, in the normal geometry. Given the difference in geometry in our case this is not fully identical, but indicative. More telling is the barrier height Q, given in Fig 4.5, for all geometries with the tip 25 nm laterally from the electrode edge. The calculated Q

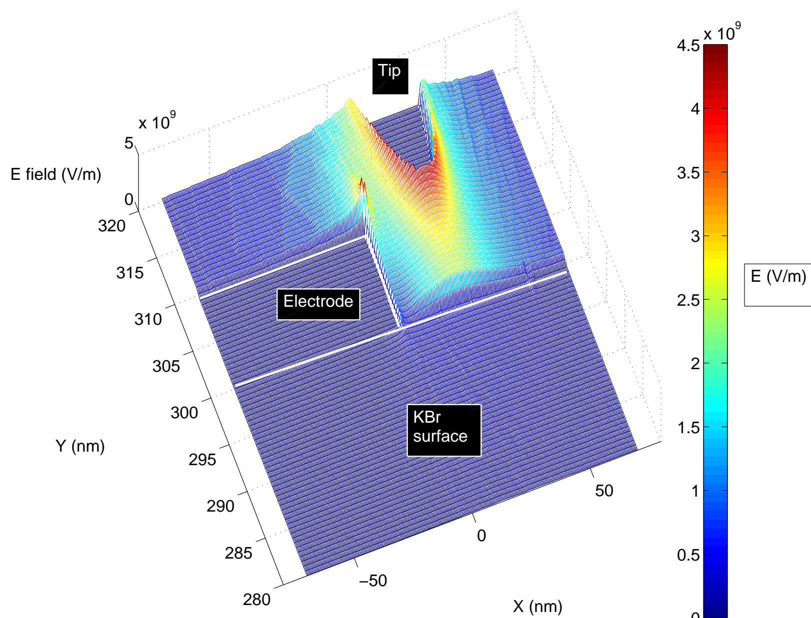

Figure 4.4: Projected electric field magnitudes calculated from a 2D slice of the original potential solution. Maxima are shown at both the edge of the electrode, and the tip apex, which is typical of the geometry.

values are below 0.772 eV in only those cases where the tip is between 5 and 10 nm or less from the surface for the Au^{2-} or less than 3nm for the Au^{1-} ion. The positive ions are also shown, though in this potential geometry would not be expected to evaporate even if the barriers were favorable which does not appear to be the case. These results suggest that the desorption process should be readily possible for the Au^{2-} state if the tip is less than 10 nm from the surface, which is similar to the conditions expected for typical geometries with a backside electrode and insulator. The lift heights for actual depositions will be discussed and compared to these projections. A similar simulation with a larger sample volume, 400 nm from the electrode edge, is also shown. The potential drop is slightly lower than that of the simulations nearby the surface at a similar height (1.0 V vs 1.3 V), but it is clear that the bulk of the variation is due to the tip lift height rather than the distance from the electrode, with the insulating surface acting as a virtual ground in itself, due to the large difference in dielectric constant.

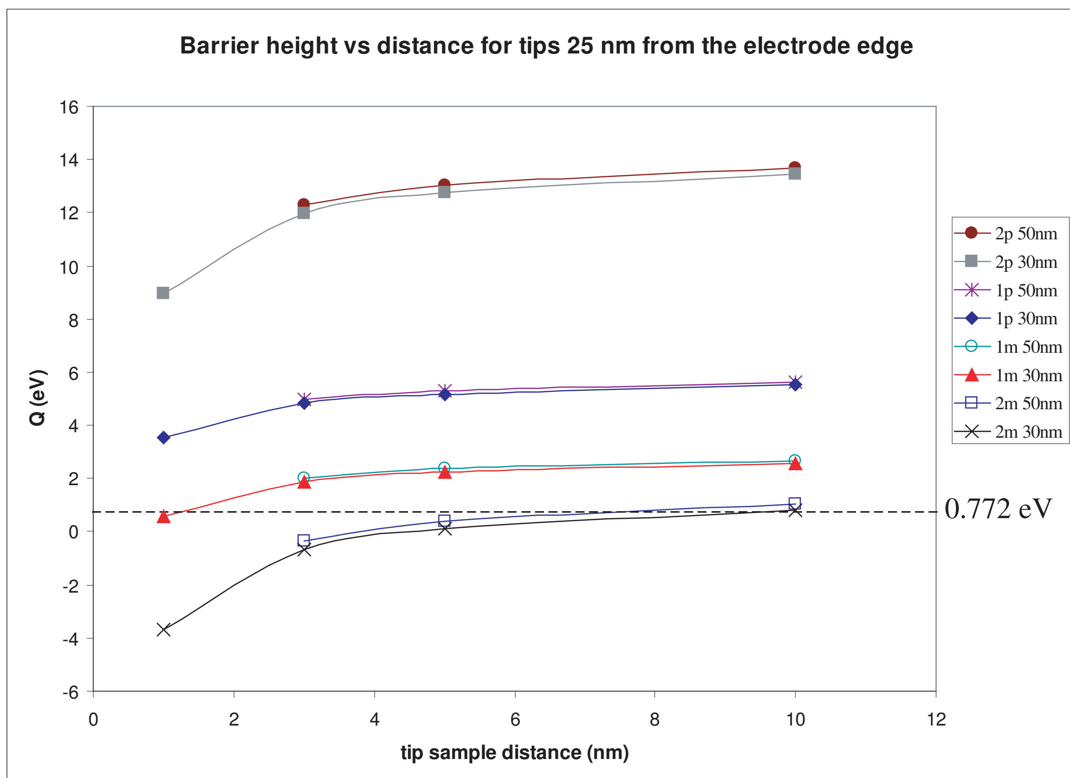

Figure 4.5: Barrier heights calculated for 30 or 50 nm diameter tips, 1, 3, 5 or 10 nm from the surface of the edge, 25 nm laterally from the edge. Similar calculations for a 30 nm tip, 20 nm laterally show similar characteristics but with a slightly reduced barrier (0.06-0.15 eV lower). The Au^{1-},Au^{2-},Au^{1+},Au^{2+} states are shown (1m,2m,1p,2p respectively). Lines shown only to readily differentiate the cases, not actual fits.

Model geometry	ΔV over r_0 (V)	Electric field (V/Å)
Over electrode edge, 1nm up, 30nm	5.1	5.4
Over electrode edge, 3nm up, 30nm	1.8	2.2
20nm laterally from edge, 1nm up, 30nm	2.5	1.7
20nm laterally from edge, 10nm up, 30nm	0.7	0.5
25nm laterally from edge, 1nm up, 30nm	2.4	1.7
25nm laterally from edge, 3nm up, 30nm	1.3	0.9
25nm laterally from edge, 3nm up, 50nm	1.1	0.8
25nm laterally from edge, 5nm up, 30nm	1.0	0.7
25nm laterally from edge, 5nm up, 50nm	0.8	0.6
25nm laterally from edge, 10nm up, 30nm	0.7	0.5
25nm laterally from edge, 10nm up, 50nm	0.6	0.4
400nm laterally from edge, 3nm up, 30nm	1.0	0.7
5 nm onto electrode, 3nm above, 30nm	2.1	1.4

Table 4.1: Potential drop within one atomic radii of the tip for 30 and 50 nm diameter tips, estimate of the electric field at the tip, both calculated for a -40V potential at the tip. Directions given with respect to electrode edge laterally and surface vertically.

4.3 Tip forces during deposition

One concern during deposition is the effect of the large electric field during the pulse itself. The application of a large bias to the tip and cantilever has a twofold effect; first, the AC amplitude of the tip will be damped due to the electrostatic force as the change in cantilever resonance shifts the amplitude off the peak position, and second, the DC height of the tip will decrease due to the capacitive force between the cantilever and tip assembly and the metal surface. The AC effect will tend to decrease the amplitude of the oscillation, increasing the average tip sample distance, but this is balanced by the effect of the attractive DC force. If the DC force is sufficiently large, the cantilever will deflect fully into the surface, followed either by an indentation of the surface or mechanical damage to the tip (depending on the relative stiffness of the surface), or a large current pulse will result as electrical contact is made with the surface, effectively creating a short at fixed voltage. The results of such a contact can be catastrophic, in the case of coated tips the gold coating can be entirely peeled away from the tip. In order to prevent this, it is necessary to understand the maximum forces created by the voltage pulse to the tip.

The first order approximation using a parallel plate capacitor model, gives a force of

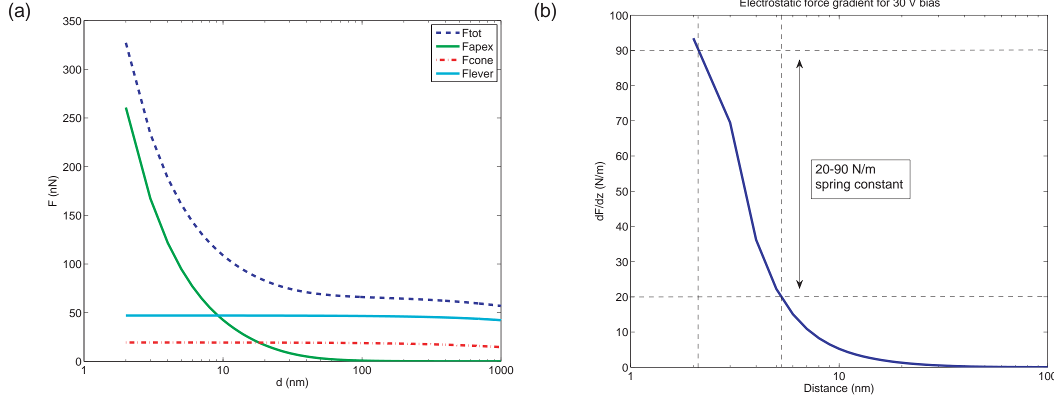

Figure 4.6: Electrostatic force vs tip sample distance for 30 V applied potential, (a) 10 μm tall tip, with different force contributions shown, (b) force gradient for comparison, with the spring constants and effect tip height at which snap in may occur indicated

$F = \frac{\epsilon_0 w L V^2}{2d^2}$. If a 10 μm separation between the sample and cantilever is assumed, typical for Nanosensors commercial cantilevers, and a 38 μm by 250 μm cantilever with 40 V applied potential are also used, one finds an attractive force of 670 nN. Comparing this to the maximum dynamic restoring force kA, 600 nN with a spring constant of 100 N/m and an amplitude of 6nm, it is clear that there may be a problem. This simple model does not take into account the attractive force due to the tip apex or cone, and also overestimates the cantilever force as the lever arm for the cantilever is elevated above the surface at some finite angle.

A more complete calculation of the contribution of the various components of the tip has been done by Colchero et al [102]. The contribution due to all three major parts of the system is calculated assuming a smooth conical tip with a truncated cone of radius r. In most tips used however the cone is generally pyramidal. The various components of the force are as given by

$$F_{lever}(d) = f_{lev}\epsilon_0 \frac{lw}{h^2} V^2 \frac{1}{(1+d/h)(1+(d+2l\tan(\theta_{lever}/2))/h)} \quad (4.8)$$

$$F_{cone}(d) = f_{cone}\epsilon_0 V^2 \Bigg[ln\left(\frac{d-\delta/2+h}{d+\delta/2}\right)$$

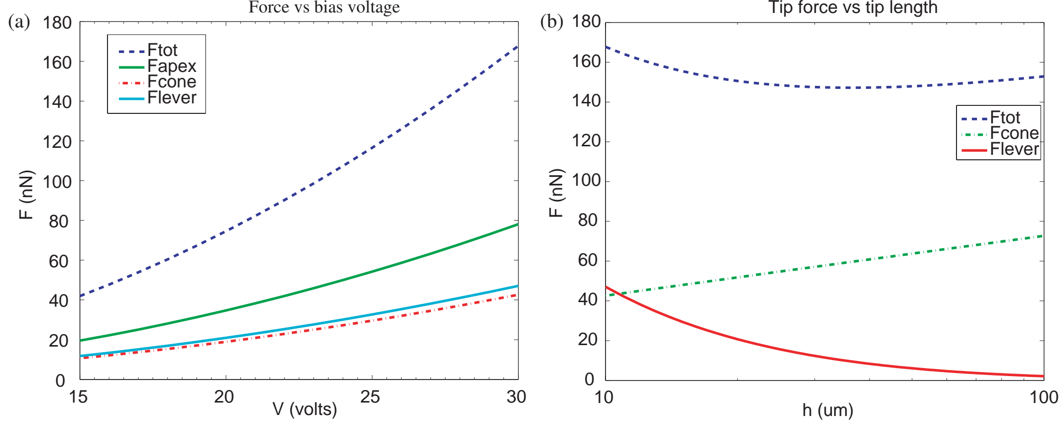

Figure 4.7: (a) Electrostatic forces vs voltage, 6nm lift height, 10 μm tip, (b) Electrostatic forces vs tip height for a 30V potential, apex force is constant at 78 nN and not shown

$$ - \sin(\theta_{tip}/2)\frac{h-\delta}{d-\delta/2+h}\frac{d-\delta/2}{d+\delta/2}\Bigg] \tag{4.9}$$

$$F_{apex}(d) \cong \frac{\pi\epsilon_0 V^2}{1+f(\theta_{tip})(d/r)^2}\left(\frac{r+d/2}{r-2d}\right)^2\left(\frac{r-2d}{d[1+2\tan^2(\theta_{tip}/2)d/r]} + 2ln\frac{4d}{2d+r+(r-2d)\cos(\theta_{tip})}\right) \tag{4.10}$$

with $f_{lev} = 2\tan^2(\theta_{lever}/2)/\theta_{lever}^2$, $f_{cone} = 4\pi/(\pi-\theta_{tip})^2$, $\delta = r/\tan^2(\theta_{tip}/2)$,$f(\theta_{tip}) = ln[1/\sin(\theta_{tip}/2)]/[1-\sin(\theta_{tip}/2)][3+\sin(\theta_{tip}/2)]$, h the tip height, l and w the cantilever length and width, V the applied potential, d the tip sample separation, and θ the tip and cantilever angles (with respect to the plane for the lever, and the full cone angle for the tip).

In these experiments Nanosensors PPP-NCLR cantilevers are used, coated as discussed below. The typical cantilever parameters are: k = 21-98 N/m, $t = 7 \pm 1\mu$m , l = 225 ± 10 μm , w = 38 ± 8μm , h = 10-15 μm , and h = 146-236 kHz. The normal resonant frequency of the gold coated cantilevers is typically 150-160 kHz. Using these parameters and a voltage of 30V, the tip sample forces are calculated and shown in Fig 4.6. At a distance of 6 nm, the tip experiences an electrostatic force of approximately 170 nN. Given a tip amplitude of 6 nm, and a 21 N/m spring constant, this is well within the range for a snap-in of the cantilever during pulsing. To avoid snap-in, and the possibility of a large current pulse or mechanical damage

to the tip, it is necessary to decrease this force. As shown in Fig 4.7(b), an increase in the tip height has only a moderate effect, as the increased cone forces compensate for the small change in height, whereas a reduction of the tip voltage has a much more significant effect. The difficulty is that the tip voltage is critical for the deposition process, this does however indicate that the safe procedure is to ramp the voltage slowly while searching for this minimum. Further reductions are possible to the tip voltage by decreasing the tip radius, the cone angle, and increasing the oscillation amplitude. Both of the first two are accomplished as discussed below in the tip preparation by the etching of long narrow tips using the FIB or chemical etching. An increase in the oscillation amplitude is also possible, but with the drawback that it also decreases the material emitted from the tip as the average time spent in close proximity to the sample decreases.

4.4 Tip Fabrication

To carry out the deposition discussed in section 4.1, it is necessary to have a sufficiently high electric field at the apex of the tip. The primary parameters determining this are: the potential applied between tip and surface (up to 40V, limited by the pulse generator), distance between the tip and surface, and the tip radius. Typical experiments of this type are carried out using commercial AFM tips coated with an evaporated layer of gold. The original tips have typical radii of 5-10 nm, depending on the specific type, but the final tip shape is largely determined by the deposited metal thickness, grain structure, and deposition parameters.

Initial depositions were carried out with gold coated tips, but due to significant difficulties depositing on KBr samples it was decided to attempt to find sharper tips. Focused ion beam etching of metal wire tips, in particular gold or silver [103, 104], can produce tips with radii of 5 and 9 nm. Similar tips were fabricated using 13 or 25 μm diameter gold wires and the approach described below, with slightly larger final tip radii (15 nm).

The primary limitation of this approach is the time required to attach a wire to the cantilever, then mill the tip structures using the FIB. The overall preparation time per tip can be as long as 3 hours, which is a significant limitation for fabrication

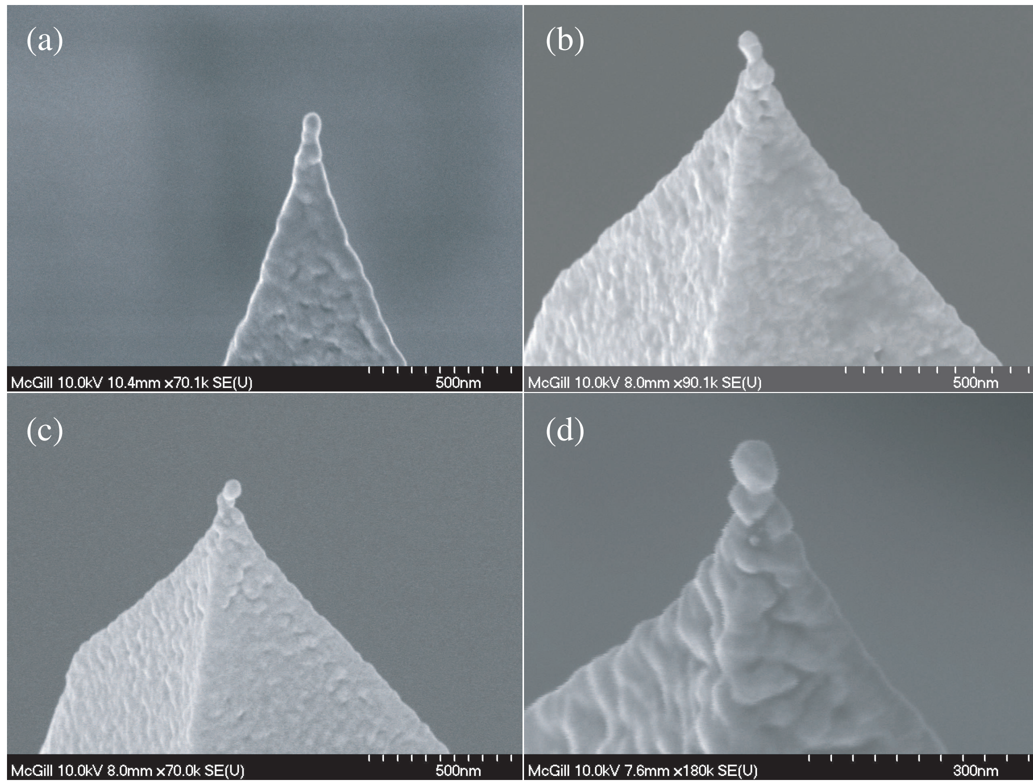

Figure 4.8: Gold coated tips with a 100 nm Au coating, all 2 nm Ti adhesion layer, barring (a) (10 nm Ti), tip diameters (nm)(a) 66±2, (b) 53±3,(c) 57±3,(d) 61±4

efforts. To increase the rate of tip production, an alternate approach was devised, using electrochemical etching of the gold wires in a solution of perchloric acid and NaCl under an AC bias. While the success rate of the tip fabrication from this approach is lower, the etching time is typically 5-6 seconds.

4.4.1 Coated tips

Commercial silicon cantilevers (Nanosensors point probe plus NCLR with a typical spring constant C = 48 N/m, resonant frequency f_0 = 190 kHz, and tip radius less than 10 nm) are used in all gold tips, both coated and using attached wires. The tips were gold coated in a thermal evaporator, Thermionics Lab. VE-90. A 2 nm titanium adhesion layer followed by 100 nm of gold were deposited at 0.4 and 1.4 Å/s respectively. The maximum cantilever temperature during deposition is $\approx 150°$ C, with a pressure of $2{\cdot}10^{-6}$ torr at the end of the evaporation cycle.

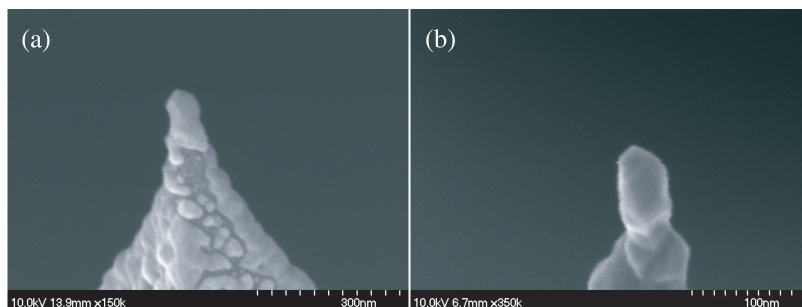

Figure 4.9: Faceted gold coated tips, uncertain (though small) Ti adhesion layer thickness and 100 nm gold layer

While this is the typical evaporation sequence used for gold coating, it may not be the ideal. Several tip batches were also prepared with 10 nm Ti layers, as well as one evaporation with little to no titanium due to a malfunction in the evaporator. Interestingly, the evaporation of titanium in the latter sample, where the titanium thickness is not well known but thought to be relatively thin, the gold apex of each tip possessed a strongly faceted point, rather than the usual spherical apex as shown in Fig 4.9. It is possible that the lack of an adequate adhesion layer led to the formation of oriented gold grains in the tip. Deposition characteristics using these specific tips were noticeably different, and will be discussed below.

During evaporation the cantilevers are held in place by copper beryllium fingers on the bottom third of the cantilever chip with the cantilever side up, and rotated at several hertz to provide relatively uniform coverage around the tip and cantilever beam. The evaporation rate is continuously monitored by a quartz crystal balance (Inficon). Metal is evaporated vertically from alumina coated or uncoated molybdenum boats, resistively heated. The cantilever resonance typically decreases from 160-170 kHz to 150 kHz as a result of the increased mass.

Tip apexes have a diameter of 50-60 nm and are spherical or oval in shape. In addition, the final gold grain at the apex of each tip is often slightly off center, and typically slightly larger than the final cone radius of the tip itself rather than a simple protrusion of the film, in most cases. The effect appears to be the most severe for smaller titanium adhesion layer thicknesses.

Cantilevers coated using no titanium adhesion layer have extremely poor gold adhesion. The coating, particularly near the tip apex, is highly variable, with voids,

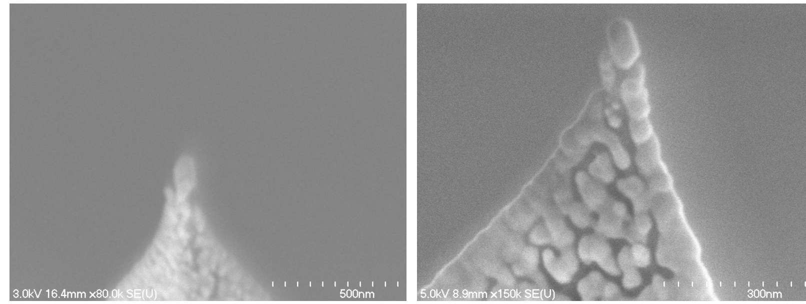

Figure 4.10: Gold coated tips with no titanium layer, 100 nm Au coating

different grain sizes, and variable structures, shown in Fig 4.10. It does not clearly show the faceted characteristics described above but is similar to the growth of gold grains on a flat silicon surface as expected. It is likely that either an intermediate thickness of titanium is required (between zero and two nanometers), or that other unknown factors play a larger role, including temperature, pressure, and rate. All three forms of tips, with an adhesion layer, without an adhesion layer, and strongly faceted tips have been successfully used to deposit gold clusters onto insulating InP heterostructures surfaces as will be discussed in the following sections.

4.4.2 FIB tips

As an alternative to simple coated tips, cantilevers have been prepared by attaching a gold wire vertically to the cantilever and then shaping the tip using the focused ion beam. Milled tips have a slightly smaller radius, but take significant amounts of preparation time. The preparation is described in Cockins [104] and Akiyama [103].

The cantilevers are coated as in section 4.4.1 to provide the electrical contact to the wire. In order to attach the wire, the cantilevers are mounted in the set up shown in Fig 4.11. A cut glass slide is scored to form a trench a few hundred micrometers deep using a rotating diamond saw, and used as a base to hold and select gold wires for attachment. The gold wires are cut using scissors, then trimmed if needed using a razor blade under the stereo microscope, at a viewing angle of $\approx 45°$. Typical lengths are 100-500 μm long. Ideally, the wire face should be as flat as possible, a steep slope on the initial cut makes attaching the wire to the cantilever significantly more difficult. Several wires are cut at a time, and deposited on the glass surface. One

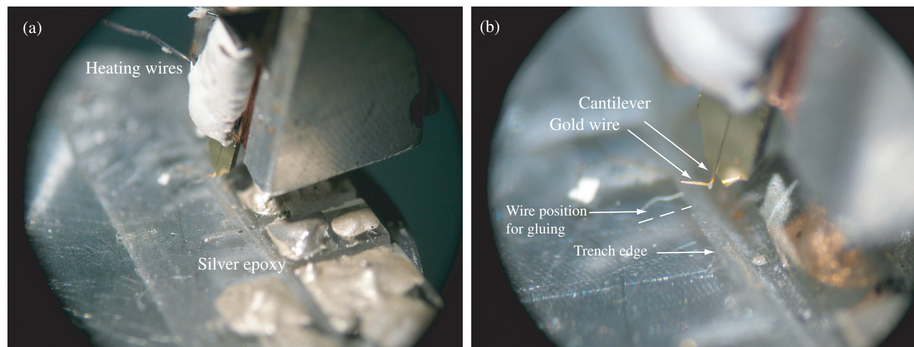

Figure 4.11: Tip gluing setup. (a) Manganin heating wires (left), cement epoxy setup coating, and cantilever chip shown above the scored glass slide with an attached wire (b) Close up, wire and cantilever lifted off the surface with the original wire orientation shown (dashed line)

wire is selected at a time, and positioned over the edge of the scribed trench using a needle.

A small mound of silver epoxy, H20E Epotek, is placed on the glass slide close to the scribe, and the apex of the cantilever is dipped into it using an XYZ micromanipulator. Less than one quarter of the cantilever is covered by the epoxy to avoid reducing the reflected laser signal from the back side during imaging. The cantilever is then approached to the wire, and moved into contact using the manipulator. As this particular epoxy requires elevated temperatures to cure, the holder and cantilever chip are heated to cure the epoxy by wrapping a coil of manganin wire (a high resistance alloy of copper, manganese, and nickel) around the clip holding the chip and surrounding it with a ceramic epoxy. The wire is then resistively heated, with temperatures on the clip reaching over 200 ° C, with the cantilever itself reaching the target temperature of 150 ° C, at which the epoxy cures within 5 minutes.

In order to fix the wire onto the cantilever, the temperature is gradually raised to 150 ° C, slowly over a few minutes, as the rapid heating can cause the cantilever to shift and pull away from the the wire. The wire will be fixed to the cantilever with strong electrically conducting bond for either FIB milling or chemical etching, described in section 4.4.3. The process takes ≈30 minutes per cantilever.

To create tips with the FIB the attached gold wires are shortened as described in Cockins [104], even wires 100 μm in length are far too long to adequately FIB in a

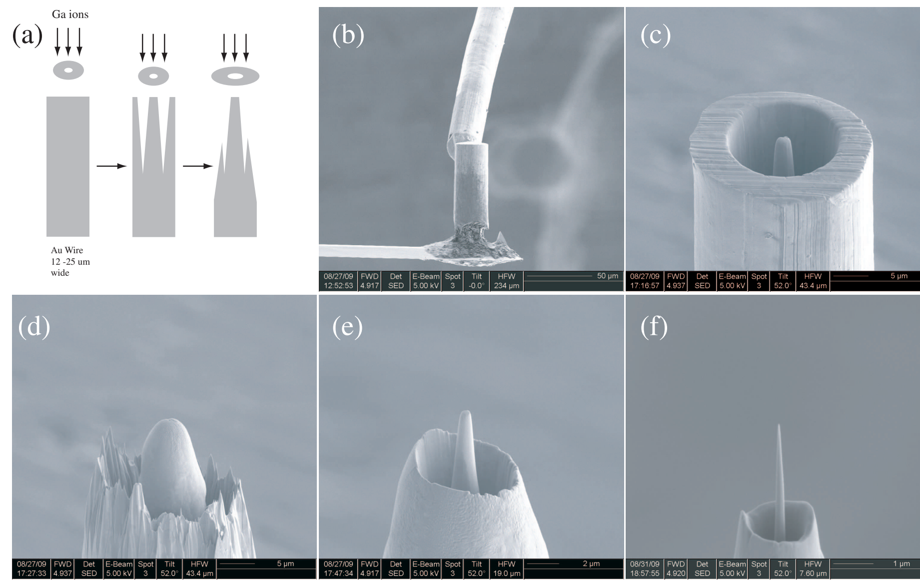

Figure 4.12: Tip milling process for gold wires attached to silicon cantilevers. Trimming stage is not shown, as well as subsequent narrowing stages.

reasonable time frame. The cantilever is mounted sideways using double sided copper tape to a raised aluminum square such that it protrudes from the edge horizontally with the tip parallel to the surface. The FIB is focused on the top of the wire and a trench is cut to remove the end of the wire, 5x30 μm for a 25 μm diameter wire, at 5-7 nA beam currents and with a depth of 4 um, based on silicon etch rates (6-7 times slower than gold). A specific calibration was not done for gold because the structures being milled have a large number of edges, which also significantly increases the milling time making an exact calibration ineffective. After cutting, the removed gold tends to adhere to the cantilever electrostatically, shown in Fig 4.12(b), until removing the cantilever to re-seat it with the tip facing up. Simple mechanical handling is sufficient jar the wire segment free.

In order to create the tip at this point, a series of milling steps are used at progressively lower currents to thin the wire, remove extra material, and gradually work down to the sharpest tip possible. The process is described in both Cockins and Akiyama, so only the important details will be discussed here. The process used by Akiyama involves milling out a donut shape to create a central needle, with the external rim removed afterwards. During the removal of the outer rim a large amount of material is redeposited on the central needle, unnecessarily increasing the overall milling time.

If the outer ring is removed first, then the inner and working from there, it is possible to avoid this redeposition. Positioning of the annulus for milling involves aligning the ion and sem beams at the very apex of the cut cantilever. The ion beam can be used to image as well though it removes material in the process. The alignment is critical for sharp tip milling, as well as the pre-alignment of the FIB itself for the different milling currents (allowing a shift in beam current with minimal shift in position). If the alignment shifts significantly while changing between currents it becomes difficult to maintain the correct position over the apex of the tip.

Milling time is on the order of 20 minutes for the initial needle at a beam current of 5 nA and with a size of 1.5 x 8.5 μm (inner and outer diameter), then 20 minutes to trim the outer rim. The milling process is shown in Fig 4.12(b-f). The second milling cycle uses 300-1000 pA currents and creates a 1 to 2 um needle, requiring another 20-30 minutes total. The final etching steps require a series of careful trims at lower beam currents 10 to 100 pA. The critical consideration in creating the final sharp apex of the wire is that the final annulus, which must not be too small. The ion beam profile, enhanced milling at edges, and slightly imperfect focus all contribute to actually etch slightly inside in the center of the annulus [105]. Empirically, the smallest center annulus possible at 10 or 30 pA is typically 100-150 nm. Even at this point the beam will begin to etch the central feature of the tip, but with a sufficiently long shank the tip can have a radius as small as 15 nm at the apex, with a cone angle of $7 \pm 3\ ^\circ$. As this angle depends strongly on the precise focus of the beam with respect to the tip, a factor which is extremely difficult to control at this stage as the ion resolution at these low currents can be very weak with respect to the apex of the tip, a spread of apex angles has been observed. If the length of the shank is insufficient prior to milling (<5-10 μm), or the central annulus too small, the tip will be milled away very quickly, with micrometers of tip shaft removed in seconds even at low beam currents. The tip then needs to be re-thinned and the entire process repeated. The total milling time varies, but is usually on the order of 1.5-2.5 hours per tip, not counting the time to cut the initial segment off, which is about 30 minutes. Care must also be taken not to inadvertently etch the gold coating on the cantilever while removing the outer annulus, else the electrical contact to the tip can be destroyed.

The length of the milled tips varies significantly based on the time of the final etch

and the length of the cone created by the final annulus. Typical values though are from 1-5 μm with an overall tip length from cantilever to apex of 10 to 50 μm .

4.4.3 Electrochemically etched tips

Production of sharp gold tips using the FIB is a time consuming and expensive process though the precise tip geometry is known from SEM and ion images immediately after fabrication. As an alternative, chemical etching can be used to fabricate sharp tips with nearly the same radius of curvature as the FIB, but in a vastly shorter time frame.

Gold is generally thought of as inert to chemical attack but it too can be etched by certain chemicals, particularly if an electrochemical bias is used to provide the additional energy. The most well known gold etchant is aqua regia, a mixture of strong hydrochloric and nitric acid which attacks gold and other noble metals. Nitric acid oxidizes the gold surface, followed by the reaction of the gold oxide with free chlorine to form chloroaurate anions ($AuCl_4^-$). Neither solution alone is sufficient to etch the gold surface alone.

Most tip etching processes are based on similar chemistry. Several successful etching methods have been demonstrated, including HCl based etchants [96, 106, 107], $CaCl_2$ [108], or NaCl and perchloric acid [109, 110]. Virtually all processes take advantage of the chlorine reaction to dissolve gold and form chloroaurate anions with an applied electrochemical bias. As gold can also be oxidized at the surface of the electrode, one of the difficulties in the preparation of sharp tips using these etchants is avoiding the passivation of the gold surface by an oxide as soon as the local chlorine population is depleted. Some of the methods used to avoid this effect involve additional solvents such as ethanol, AC voltages, or subsequent polishing steps in entirely different etchants (HCl then $CaCl_2$ [111]). Etching in chlorine free solutions may oxidize the tip,

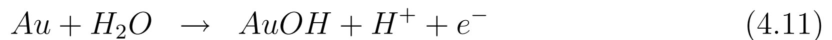

$$Au + H_2O \rightarrow AuOH + H^+ + e^- \tag{4.11}$$

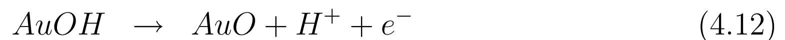

$$AuOH \rightarrow AuO + H^+ + e^- \tag{4.12}$$

at 1.3 or 1.5 V for the hydroxide anions [109]. With the addition of chlorine the gold

is attacked rather than oxidized,

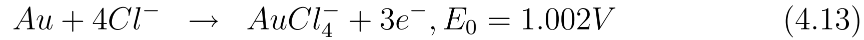

$$Au + 4Cl^- \rightarrow AuCl_4^- + 3e^-, E_0 = 1.002V \quad (4.13)$$

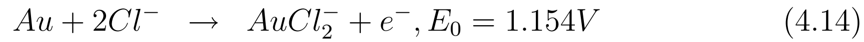

$$Au + 2Cl^- \rightarrow AuCl_2^- + e^-, E_0 = 1.154V \quad (4.14)$$

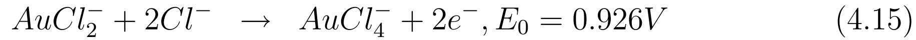

$$AuCl_2^- + 2Cl^- \rightarrow AuCl_4^- + 2e^-, E_0 = 0.926V \quad (4.15)$$

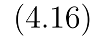

(4.16)

[106] with the consequent generation of large amounts of hydrogen at the electrode as well, leading to a significant amount of bubbling. The necessity of the perchloric acid is not well understood, it is assumed that it is primarily important for lowering the solution pH which appears to improve the etch process [109]. Etching of gold surfaces under perchloric acid with and without chlorine ions has also been investigated by STM, and it was suggested that the chlorine atoms act to stabilize particular step directions (211) due to preferential adsorption [112].

The choice of chemical etchant in this case was determined based on the suggested tip radii observed in previously published work as well as the difficulty and safety of the etching process as some of the chemical etchants used are highly toxic. For an improvement in the gold deposition process over simple coated tips it is necessary to have tips with 25 nm or smaller radii. Most tip etching procedures have tip radii well in excess of 50 nm, and often require multiple steps. The approach selected here was based on a simple AC etch in 3.0M NaCl in 1% perchloric acid ($HClO_4$) by Gingery et al[109] who reported tip radii of 15 nm, and relatively short etch times. Some changes were necessary to accomodate the smaller wires used in order to attach to AFM cantilevers (13-25 μm vs 250 μm use for STM tip etching). The solution was prepared using stock NaCl powder (Alfa Aesar) added to perchloric acid diluted from a 25 % stock solution. Perchloric acid can be extremely dangerous so care is needed in handling concentrated solutions, even vapors from the solution will attack organic compounds to form explosive salts. The etch process takes place at room temperature with no active temperature control on the solution, held in a teflon bath with a small volume.

The etching setup is shown in Fig 4.13. A holder was machined from stainless steel to mount the cantilever chips with a stainless steel clip to provide the electrical contact to the wire, not shown. As an added precaution against the tips moving, double

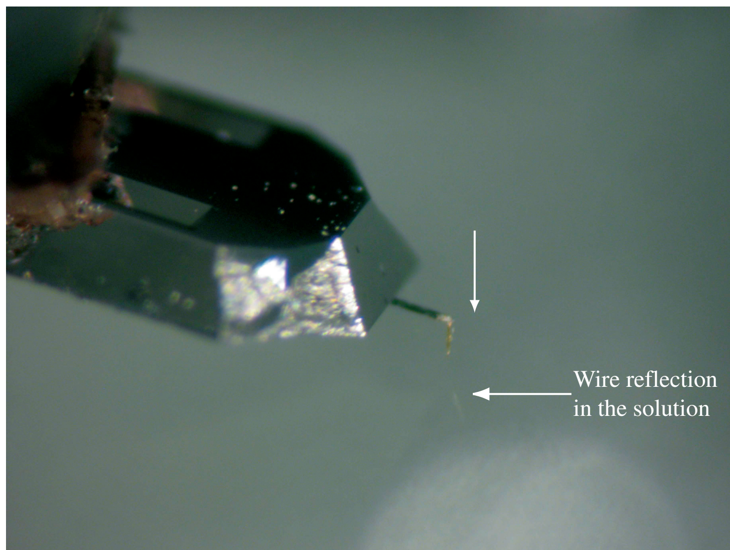

Figure 4.13: Tip etching setup above the perchloric acid solution. The reflection shown appears within 100-200 μm of the surface.

sided copper tape (3M) was used to provide an adhesive base for the cantilever chip. To minimize vibrations while moving the tip into and out of the etching solution, an electrical micromanipulator (SD MC1000e 4-axis controller) was used, with approach speeds of: 1.7 mm/second, 300 μm/second, and 2-50 μm/second. For a counter electrode, 25 mm x 3 mm tantalum rods were used. This is one of the few metals with a fairly good chemical resistance to the perchloric acid solution, though after several tip etchings the electrode was found to be coated and in need of rinsing in order to continue. The cantilever with the gold wire attached was fixed into the holder, attached to a long magnetic stainless steel rod with an attached magnet, and mounted into the holder. While observing using the stereo microscope, the wire was lowered into the etching solution at medium speeds to close proximity with the surface then advanced at 2-50 μm/s for the final approach into the liquid, with the etch voltages on. Etching was stopped manually just prior to the end of visible bubbling, just after the wire etched entirely above the surface of the liquid.

Several voltage and frequency combinations were attempted, based on the literature for similar etch processes. Boyle [108] uses a $CaCl_2$ etch process and compared the effect of frequency, voltage and concentration, and found 2kHz to be the optimum etch frequency. It was later learned that the etch was actually carried out with a simple rheostat at 60 Hz, with no offset (private communication). While various

frequencies were tried in optimizing this etch process, it is possible that the ideal etch frequency maybe be closer to this than the 2KHz used, as there is some evidence that higher frequencies sometimes lead to a blunting of the tip. A single test at this frequency and with no offset produced a much slower etch time, with extensive bubbling suggesting more gas formation and perhaps surface oxidation of the tip. The tip quality was significantly worse as well. For this work a Stanford Research Systems function generator (DS345) was used to apply a 2.5 V amplitude, 2kHz sinusoid to the tip, with a 3V offset to keep the voltage entirely positive with a 1 ohm series resistor as a current limit and to measure the tip current (1-6 mA). The greatest difficulty in approaching the tip to the solution is advancing the tip into the solution without the liquid snapping into contact to the cantilever, holder, and chuck. As the tips must be as short as possible to avoid mass loading the cantilever and due to a limited height clearance between tip and sample, the cantilever must be brought as close as possible to the sample, which in practice is between 50 and 100 μm . At this height if the solution bubbles too much or there are external vibrations it can make contact with the cantilever, this will then quickly etch the gold film over the entire surface. Using the stereo microscope one can observe the approach of tip and surface, with a visible reflection in the solution as the tip is within 100 μm, see Fig 4.13.

The etch process is observed and then stopped by hand both by turning off the etch and rapidly retracting the wire. As the wire is much thinner than those typically etched in the literature, the process is very fast, taking 5-6 seconds, and consumes the entire submerged part of the wire up to the meniscus. Even a slight overetch can blunt or deform the tip, so an electronic cutoff may improve the process. The use of an AC current and the lack of a precise drop-off are the major difficulties in implementing such a system, typical etch stop systems monitor the current or derivative current and stop the etch when the remaining material drops off. In this case there is no such clear event, and once the wire etches fully above the liquid level a blunt tip with an apex microns wide is left.

The overall success rate for good tips, as defined by any tips with an apex diameter of less than 50 nm is roughly 26% so far (11 out of 43 tips). This includes all tips, including several which broke prematurely, were deliberately overetched, or otherwise excluded, thus the actual success rate is closer to 30% (or 11 out of 37, though this also includes tips using 13 um wires, only one of which was usable). In general with

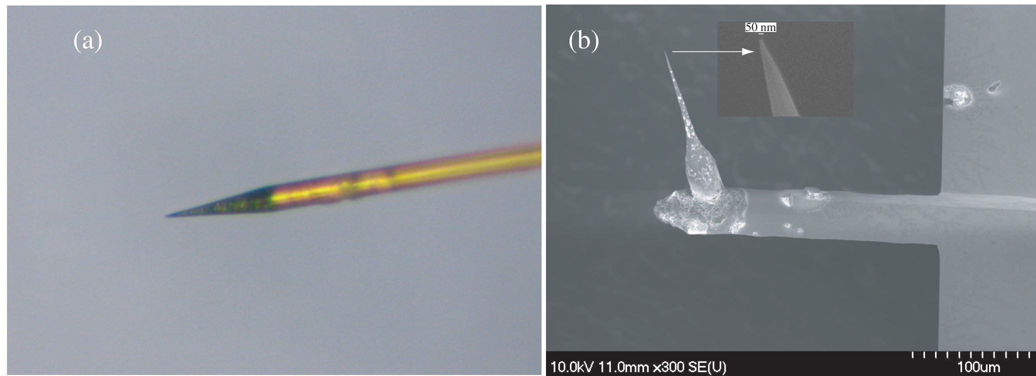

Figure 4.14: Etched gold wires (a) Optical image of bare etched wire, (b) Etched gold tip attached to commercial silicon cantilever using H20E silver epoxy

the procedure thus far the usable tip rate is around one third. Even tips which fail to etch correctly are potentially useful as secondary FIB tips, or for re-etching if the shank is sufficiently long.

A wide range of tip radii and angles is observed, but if one considers only tips with a diameter under 50 nm, the observed tip diameter is 35 ± 7 nm, which is comparable to the 15 nm mean tip radii observed by Gingery for similar etching conditions. The shank angle varies significantly, but a wide tapering shank to the tip of $20 \pm 10\,^\circ$ with a slightly narrower shank at the apex of $17 \pm 7\,^\circ$ is the most common structure. There are some exceptions to this, and the reason is not clear, in several cases the majority of the tip shank is extremely narrow, less than $10\,^\circ$, with a widening towards the apex.

The use of these tips for depositing gold clusters on several different surfaces, along with FIB machined, and coated commercial tips will be discussed in the following sections.

4.5 Deposition procedure

The deposition procedure followed herein is largely based on the method described in the PhD thesis by M. Pumarol [113]. Some variations were necessary in order to accommodate the system and electronics used. In particular: the tip amplitude is small for both imaging and deposition (instead of 100 nm or more) tip and bias

voltages are both added directly to the tip rather than the sample, lift heights are calculated from the piezo voltage, and Labview is used in lieu of a dedicated scripting software (present in the air AFM but not the UHV system).

The tip is operated in amplitude modulation mode (Tapping-mode $^{\mathrm{TM}}$) unless otherwise specified, with an electronically damped Q-factor using one of the metallic tips described above. An initial overview image of the sample region is taken, 300-1000 nm in size, with a typical tip amplitude of 6-10 nm, and a set point of 0.95 A_0, where A_0 is the free oscillation amplitude. This can also be done in frequency modulation mode, but with the presence of large metallic electrodes near the surface there are stability problems, where the tip oscillation can be disrupted leading to PLL unlock causing the feedback electronics to retract the tip briefly and ruin the image (due to rescaling of the levels during the line by line subtraction, an unfortunate property of our JEOL acquisition electronics).

A single scan is taken of the region and the tip is retracted using the amplitude set point and repositioned over the point of interest. Prior to this scan, the region is located either by large scale AFM scans, or the SEM. The former can scan regions out to 4 μm, the latter can position the tip between 100 nm and millimeters. Depending on the scan size, creep, and thermal drift (depending on the length of scanning time prior to deposition) the positioning accuracy of the tip can be anywhere from nanometer to tens of nanometer accuracy.

In order to lift the tip from the surface a DC bias is added to the tip, with the opposite polarity of the pulse bias. The lift height can be calibrated by doing a series of amplitude vs distance curves at varying voltages as described by M. Pumarol [113], however this forces the tip into near contact and potentially damages the tip apex. Instead what is done for each tip is to observe the Z-piezo voltage while varying the tip bias directly with feedback on. The z-piezo calibration for room temperature is 4.64 nm/V (scaled by 10x at the output).

A typical bias vs z-retraction curve is shown in Fig 4.15. The lift height for a given bias can vary up to a factor of two depending on the tip geometry, sample surface, and cantilever, but the general trends are shown. The lift bias is controlled by an external voltage generator (HP E3631A), added directly to the pulse using a Tektronix AM501 operational amplifier. A Tektronix PG505 is used to generate the pulses, externally

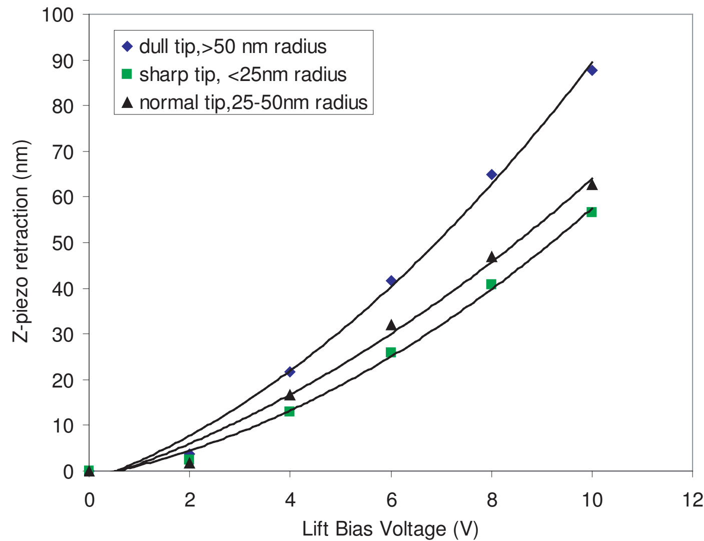

Figure 4.15: Voltage response for 3 typical tips over an InP substrate, estimated tip radii of <25 nm, ≈ 25-50 nm, or >50 nm (after a significant crash or pulse event). The amplitude set point is maintained at 0.95 A_0 and the tip retracted. The fits are a simple quadratic fit to demonstrate the dependence which does deviate from this simple model.

triggered by a square pulse generated using an NI 6036E DAQ card controlled using Labview.

After setting the desired lift height using the bias, the amplitude is set again to the desired set point as this changes slightly while adding a bias due to feedback imperfections. Labview is used to control the pulsing process, both by triggering the pulse generator, and moving the tip over the surface through the used of the external x,y, and z piezo voltage inputs. The feedback is turned off immediately prior to starting the pulse process, to avoid any small drift or creep before starting the pulses. The amplitude is recorded prior to starting, and the tip then retracted from the surface by 50-100 nm by adding a voltage directly to the piezo. Following this, the tip is moved back into the surface slowly, paused for 10-20 ms, then single or multiple pulses are triggered, one at a time. Typical pulse lengths are 1-5 ms, anywhere from 1-25 pulses at 5-10 Hz. This retraction process is unnecessary for single voltage pulses but its important while performing an array to allow the tip to move over the surface at a safe height but then re-approach to a similar set point. Following each set of pulses, the tip is lifted a similar amount, moved laterally in a

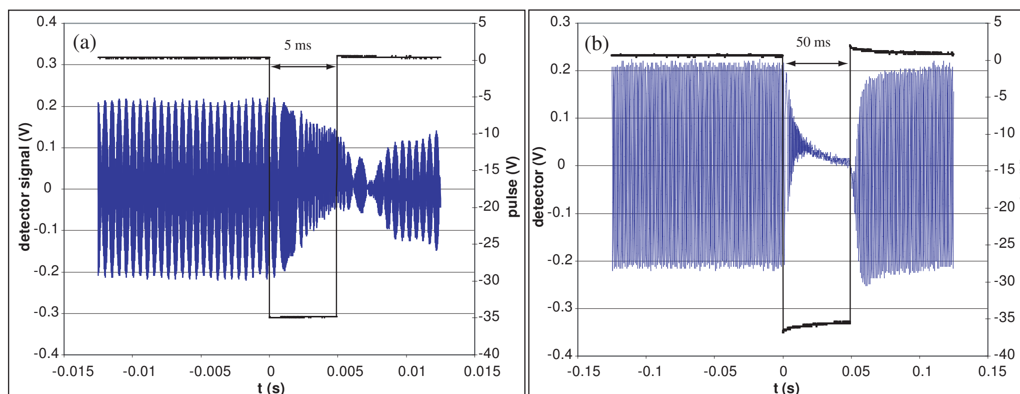

Figure 4.16: Recorded tip oscillation and pulse voltage for two pulse events, (a) 0.5 nm lift height, 5 ms pulse, (b) 5nm lift, 50 ms pulse. The oscillation amplitude in both cases is approximately 6 nm, with a resonant frequency of 150 983 Hz. The decrease in amplitude during the pulse is typical, though some features are difficult to quantify, such as the random tip amplitude changes after the initial decrease.

series of steps, then re-approached for the next pulse set.

During pulsing it is possible to externally record the tip oscillation amplitude using a digital oscilloscope (Tektronix TDS3014B) by observing the cantilever deflection signal. By this means one can verify that the tip is not making contact with the surface, given some known lift height and amplitude. During a pulse cycle the oscillation amplitude may drop to within a few percent of the free oscillation amplitude, but this does not necessarily imply contact with the surface, as this can be measured from the deflection signal.

The electronics setup is shown in Fig 4.17, a 1-50 MΩ resistor is used in series with the tip as a current limiter to protect the sample and tip to some extent in the event of contact during the pulse. Measurements of the time constant on the tip pulsing line were done to determine if the minimum pulse width would be an issue. The series resistor must be as close as possible to the chamber to minimize the capacitance delay on the pulse signal. The time constant, measured as the decay time for a single square pulse sent to the tip position with a tip present but not approached to the surface, was found to be 200 μs, with a 1 MΩ series resistor. This gave a total sample capacitance of 200 pF, typical for a thin 1m shielded cable present and attached directly to the chamber, but far too large for any limiting resistor larger than this. The original cable was removed and replaced with an unshielded cable

approximately 10 cm in length, reducing the capacitance to 12 pF. Given this, a larger limiting resistor is possible, 50 MΩ was chosen as a compromise between the pulse delay from the intrinsic capacitance such that the pulse has sufficient time to rise to the full amplitude, and the mitigating effect of the resistor. It is difficult to quantify the precise effect of a larger resistor, clearly for a 40 V applied bias, with a limiting resistor of 1 or 50 MΩ, the maximum observed current should be no more than 40 or 0.8 μA. On the microscopic scale of a tip, this is still quite large, potentially capable of damaging the tip in either case, but the damage observed in the latter case for destroyed tips is qualitatively less.

After each sequence of pulse events, an AM or FM mode image is taken of the surface to determine if any deposition has occurred. If a large and damaging event has occurred it is apparent as a large circular or oval shaped pit in the surface, between 100 and 1000+ nm in diameter and 10-50 nm deep. In many cases though, unless the precise threshold has been reached, nothing will have deposited, however the imaging conditions can still change due to movement of tip atoms or the desorption of material from the surface to the tip. It is often impossible to differentiate between the two events, however the imaging quality may change significantly in either direction. Assuming a lack of deposition, the tip is moved closer to the surface by reducing the lifting bias or the pulse voltage increased and the process is repeated until deposition is observed.

4.5.1 Gold cluster Deposition

Using the tips and methods discussed above, deposition tests have been carried out on several different substrates and with different tips. The primary goal is to be able to deposit metallic clusters on a fully insulating substrate such as KBr, but with a side electrode geometry, extending the contact across gaps created by, for example, electromigration. The calculations given above suggest the feasibility of this approach though reliability has not been fully realized as yet. Some of the deposition results on various substrates will be discussed as well as the areas of difficulty and how they might be avoided.

Individual clusters or small groups of clusters of gold have been deposited on bulk

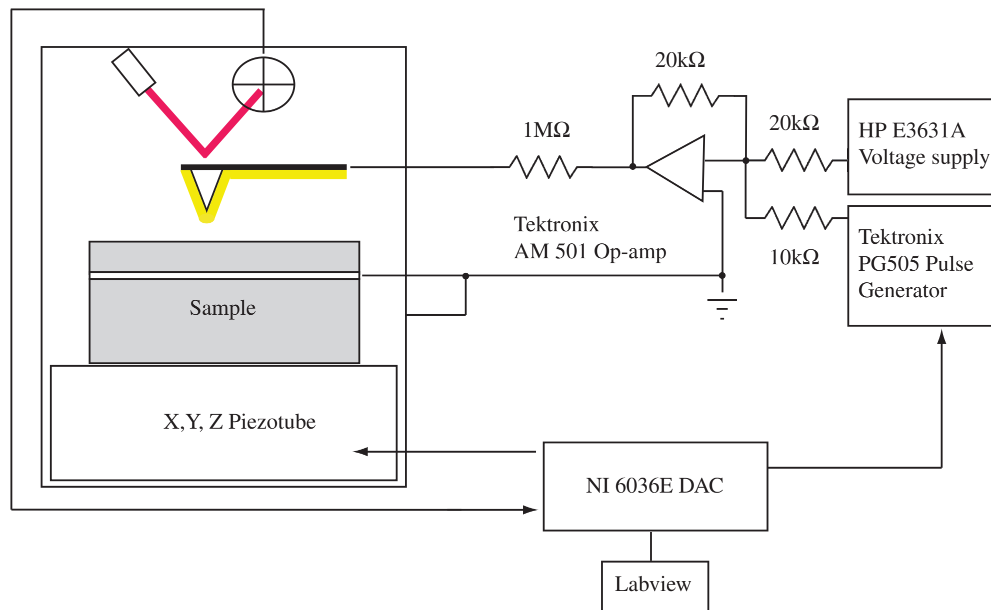

Figure 4.17: Electronics setup for the pulsing process. Pulse events are controlled using labview, with feedback during positioning from the cantilever deflection from the deflection sensor, using the amplitude measurement taken by the PLL.

KBr, on or adjacent to the metallic electrodes, and on an InP/InGaAs/InP heterostructure with a 2D electron gas as a back gate. The InP sample has been used as a test bed for the deposition process in UHV with this system. Some of the problems involved have been understood and resolved over time, such as the tip snap-in forces described above, or made redundant by a refinement of the deposition process, but there are still issues that prevent the technique from being fully effective. The primary problem is the creation of an initial deposition event safely, both sharpening the tip apex and possibly removing adsorbates and contaminants in the process. Given the large fields required, it is difficult to reach the necessary field thresholds while at the same time avoiding both the snap-in, or even a simple contact formation between the surface and tip. As the threshold is sensitive to changes of the separation in nanometers or less, and the feedback is typically turned off both before and during deposition, this can lead to small variations in the tip height and hence the deposition characteristics.

After the creation of an initial deposition event, the deposition conditions change slightly and will need to be carefully determined (in particular the tip sample lift

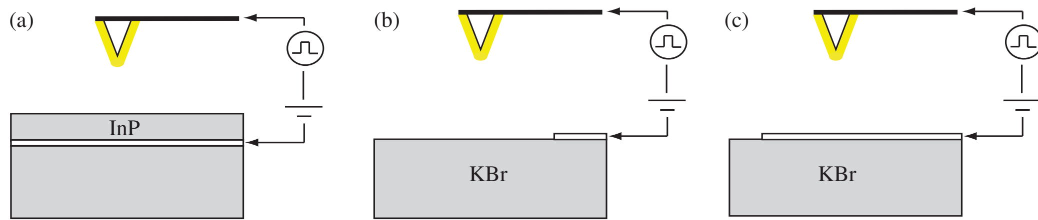

Figure 4.18: Sample deposition geometries: (a) InP heterostructure, with a 2D electron gas as the back electrode, (b) KBr substrate, depositing over the KBr surface near the metallic film electrode, (c) over the metallic electrode

height). It is reasonable to suggest that this initial event is necessary for cleaning the tip of adsorbed contaminants from the air or etching process and expose a clean gold surface, as well as a self sharpening process in which a small apex or protrusion is created and can then enhance the deposition process. The thresholds necessary for deposition change as a result of this, and a higher lift height or lower voltage is possible than previously observed. If the original lift bias is used the tip is often observed to suffer a massive pulse or crash which locally destroys the tip and surface. It is assumed that this event is a result of a local sharpening of the tip by some small protrusion which is not reflected in the lift bias. This will be discussed subsequently. In the following sections, the attempts to understand the deposition process under 3 separate regions of the surface will be discussed: over an InP heterostructure with a 2D electron gas as the back electrode, over bulk KBr with the ground applied to a surface electrode and the tip either far from the electrode or in close proximity to the metallic edge, and over the metal electrode itself, typically thin films of either gold or tantalum, the reasons for which are discussed previously.

InP surface deposition

As an initial proof of principle it was decided to use the InP substrate with a 2DEG as described above as an test bed for the deposition tests in UHV. At present there are relatively few demonstrations of UHV tip based deposition using STM techniques [114, 115, 116, 117, 118], and none in a fully UHV system using AFM deposition technique of which the author is aware. The primary advantages of this geometry over the side contacts are a much better tip voltage geometry (between tip and back gate 20 or 30 nm away vertically), less catastrophic principle events as the top surface

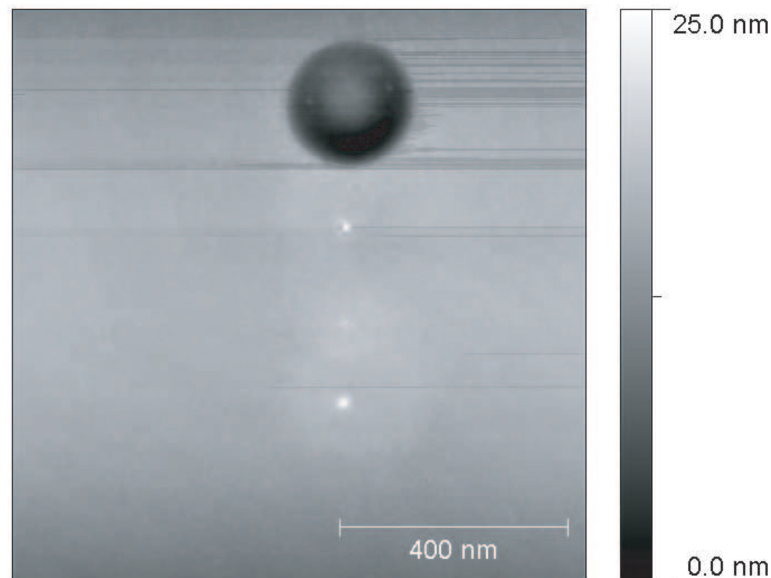

Figure 4.19: Initial tip event (top), with several subsequent depositions. The large hole is 230 nm in diameter and 11 nm deep, with the smaller clusters varying from 19-33 nm wide and 6-7 nm tall. The inital event occurred at a lift bias of 5V, as well as 2 of the subsequent clusters, the second followed at 6V and showed a more symmetric dot.

is largely insulating and even in the event of tip contact there is less risk of a massive pulse, and a flat geometry with a surface roughness of 1-2 nm.

The samples were contacted by the diffusion of an indium dot through the top surface to the 2DEG at elevated temperatures, typically 800 ° F using a soldering iron. The 2DEG was then externally connected to the ground of the tip deposition electronics as shown in Fig 4.17. Later measurements on the InP surface were done as described above, using Labview control, but the initial depositions were accomplished using a function generator to manually trigger the pulses at a low frequency, typically 5 Hz, for 5s, giving a large number of pulse events. The tip lift was also accomplished using the bias voltage, but the process was less controlled at this point, and the exact lift height is not known, only the bias voltage. From the previous curves given it is possible to estimate lift heights, but difficult due to variations from tip to tip.

The initial event for one of the most successful tips is shown in Fig 4.19, produced at a lift height +5 V with a pulse voltage of -38V. The next two clusters immediately

below were produced at a similar lift height but are asymmetric, suggesting that they may in fact not be fully field induced but at least partially due to a tip contact with the surface during the deposition process, similar to that suggested by Zhang [119]. This is also supported by the deposition of the following dot at 6 V lifting bias, which is significantly more regular at 19 ± 1 nm wide and 7.0 ± 0.1nm tall. Following these depositions the tip was moved to a fresh area and a new image taken. A series of clusters were then deposited, several at a time to examine the various parameters including pulse voltage, number of pulses, pulse length, and rows or chains of pulses. The results of these tests are shown collectively in Fig 4.20. The tip seems robust, depositing many times and with different numbers and lengths of pulses without a noticeable drop in efficiency, though there is some variation from point to point in terms of the dot size or geometry which may be indicative of the local surface structure. Similarly, the total gold volume of these depositions, and subsequent ones to be discussed below are close to the total volume possible with the grain or grains at the apex of a standard coated tips, which supports the suggested movement of gold material from the shank to tip apex in a self replenishing fashion as has been previously reported.

There are several features to note. First, while there is a definite dependence of the dot size on the voltage, there is also a definite lower voltage threshold as expected. The threshold appears to be between 20 and 24V for this lift height and tip, and deposition attempts at 20V and lower had no effect. The threshold for positive deposition is significantly higher as expected, voltages as high as +30V produced no deposits at this lift height. There is a trend towards wider depositions with higher voltage, though the height does not continue to increase which may be limited by the lift height of the tip. Deposition with pulses of 10 and 15 ms appear asymmetric, possibly due to the tip making contact with the gold islands as the length of the pulse allows the tip more time to move closer to the surface. All clusters appear to be limited to a height of less than 10 nm (in some cases there is a slight halo in the vicinity of the tip which is likely charge related and complicates the height measurement slightly), this is consistent with the tip height for this particular lifting voltage. At this point the width of the clusters appear to increase significantly more than the height, also indicative of a physical limit in the height that is given by the tip position. For the typical cluster used in this experiment, 25 pulses, 5ms long, +6V lift, -30V pulse, the cluster size is 16 ± 3nm wide by 8 ± 3nm tall. The height variation is

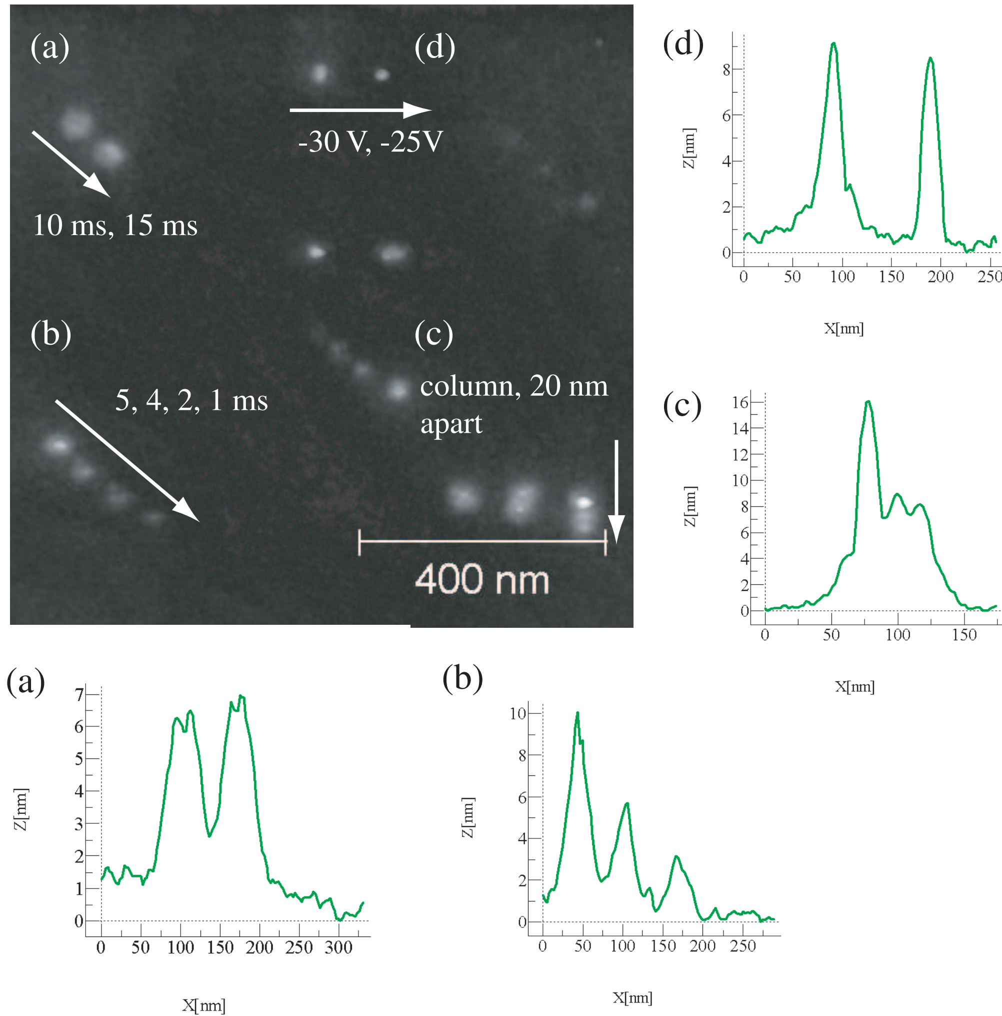

Figure 4.20: Dots deposited with a variety of pulse lengths, number of pulses, and voltages (profile direction is indicated by the adjacent arrow). (a) 10 and 15 ms pulses (x25 in each case), (b) 5,4,2,1 ms pulses (x25), (c) column of closely space pulses, 20-22 nm apart, the taller initial pulse is sometimes observed for multiple pulses (d) Pair of depositions at different tip voltages. The central diagonal series of pulses varies the pulse number (5,10,15,25 pulses).

significantly larger than that given by the width, both uncertainties are the standard deviation of the measured values, but the average uncertainty in the measured width is also 3 nm, whereas the height uncertainty is typically much less, 0.1-0.4 nm for a given measurement. This largely reflects the tip convolution difficulties in measuring the cluster size using afm.

Depositions using a 6V lift bias, -30V pulse height, and 25 pulses per point, were placed in close proximity to form lines are shown in Fig 4.21. Spacings of 10 and 20 nm were desired for most of the above depositions but the exact spacing appears to be intermediate to that in most cases, attributed to the method of tip positioning. Similar to the previous case, in several of the lines, typically those with clusters more than 20 nm apart, the midpoints are often missing and instead the endpoints increase in height. The increase is not generally double, but rather between one and two times the height of the other clusters. What is likely occurring is that the spacing of the dots is close to that of the tip radius itself, and similar to the electrode edge shown in Fig 4.4, the maximum field point is no longer under the tip but rather between the tip and the existing dot. The difficulty with this theory is that it is hard to imagine why this would not in fact increase for smaller spacings unless the effect is heavily modified by the presence of the other dot (as the electrode is actually under the surface, the dot is simply modifying the potential) or the theoretical protrusion under the tip apex which will compare in dimension to the deposited clusters.

As shown, it is possible to deposit lines of clusters. The effect of the tip proximity on the intermediate dots in a given sequence is important but not a limiting factor, as the tip can be positioned at small intervals to create the series of dots and if necessary interdigitated to create well connected structure. This is crucial for the deposition of wiring features to nearby electrodes, as will be discussed shortly there are other considerations when operating in close proximity to a metallic electrode. Similar deposition results have been explored previously by M. Pumarol [113], and these results show that the essential process is unchanged while operating in a UHV environment and using a modified form of the previous deposition procedure.

The deposition size as a function of pulse length is shown in Fig 4.22(a) and as a function of the number of pulses in Fig 4.22(b). With respect to the pulse length, both the width and height increase at approximately the same rate as the aspect ratio

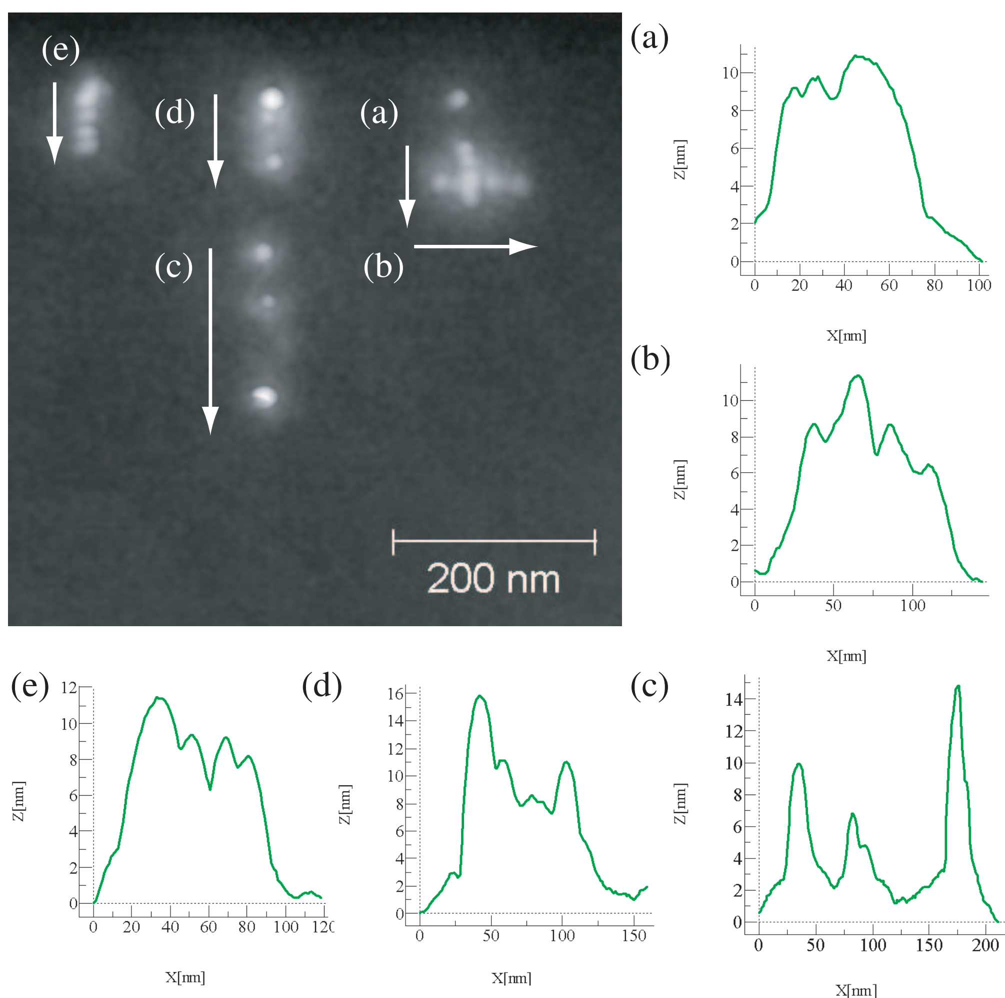

Figure 4.21: Au clusters deposited using +6V lift, -30V pulse, 25 pulses (profile direction is indicated by the adjacent arrow). Intended spacings of 10 or 20 nm, though there are variations depending on the tip placement (manual placed at each point). Again, some lines show significantly enhanced deposition at the endpoints at the expense of the middle of the line.

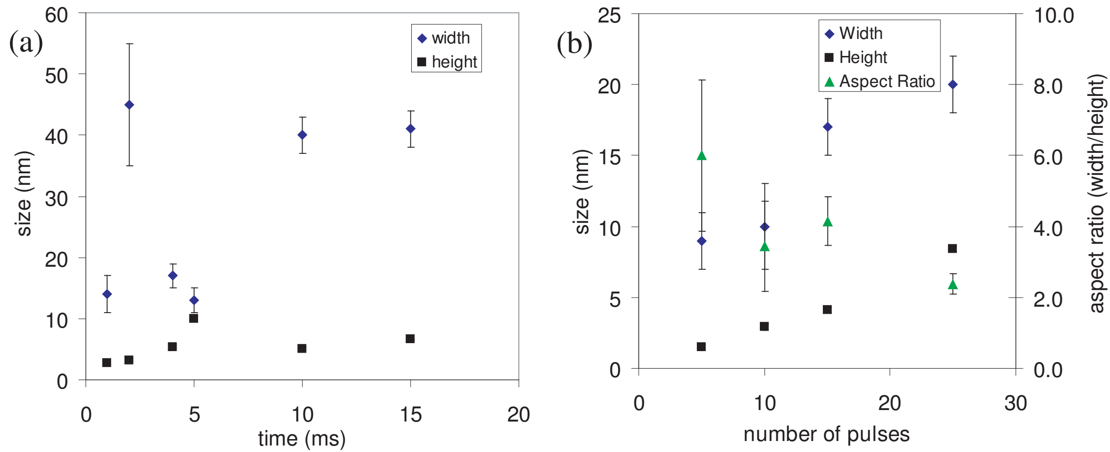

Figure 4.22: Deposition results for the same tip in a series of depositions over several areas (error estimates based on the afm measurements), (a) Cluster size as a function of the pulse length, (b) Cluster size as a function of the number of pulses over the same location

remains constant to within error. What is also telling is that the effect of the pulse length suggests the tip truly is in field deposition rather than contact mode with the surface. It also suggests that the tip position is not significantly changing during the length of the pulse event or the deposition would quickly saturate. While an increase in the deposited cluster height is expected and has been previously observed, the increase in width is unexpected and may be a result of the relatively small statistics. Similar observations [113] suggest a weak dependence on the width, with a moderate decrease. The deposit size as a function of the number of pulses shows a similar trend but the aspect ratio, actually decreases with the number of pulses as shown. The effect of both the number of pulses and pulse length should have a similar effect in fact, though the change in the oscillation amplitude with time will affect longer pulse depositions and decrease the amount of material deposited.

Depositions were also performed with the tip operating in FM mode, shown in Fig 4.23. The results were quantitatively similar to the previous cases, but the deposition quality was much more irregular over the course of a number of depositions, which may be related to precisely how hard the tip was pressed into the surface prior to performing the depositions (to ensure contact with the surface before lifting the tip a relatively large frequency shift is used, -30Hz to -300 Hz, which may affect the tip apex quality though the tip is not in fact in contact with the surface). Initial lift

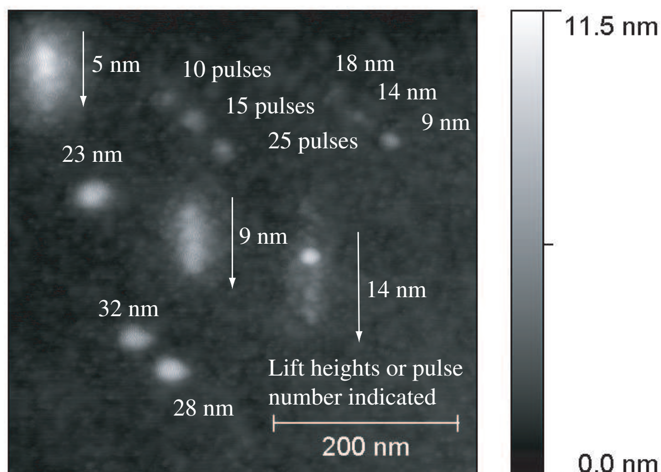

Figure 4.23: Gold clusters deposited on the same sample using an FM operating mode (same tip as previously), with the lift height based on the z-piezo voltage, pulse number, or pulse length are given.

heights were as high as 20-30 nm initially, but ended with the tip as close as 4.6 nm from the surface, based on the z-piezo voltage measured prior to applying the lifting bias. The tip was placed close to the surface at frequency shifts of 10-20 Hz, and after applying the lifting bias the frequency shift set point was used to move the tip closer to the surface again at some fixed distance based on the z-piezo voltage (unlike the amplitude modulation case, a very large frequency shift can be needed to re-approach the surface with a lifting bias applied). Islands sizes ranged from 10-25 nm wide and 0.8-7.5 nm tall. It is likely that attempting depositions at very small sample separation significantly degrade the tip apex structure, and subsequent attempts with the same tip deposited little to nothing. Also of interest to note, the lift bias used in this case was 2.4 V, giving a lift height of 23 nm, whereas a similar lift bias with the same tip in tapping mode amounted to a 23 nm lift at 5-6 V. This is a fairly large lift height, but likely mitigated by the formation of a protrusion from the tip apex under some circumstances, and could explain the discrepancy between the actual lift height for deposition and that predicted by the theoretical model.

Similar depositions were later carried out on this sample, with the sample stored under a nitrogen atmosphere in the interim. Two tips were able to deposit limited amounts of material, an example of which is shown in Fig 4.24. Over the course of the depositions the pulse number was increased significantly but the islands decreased in

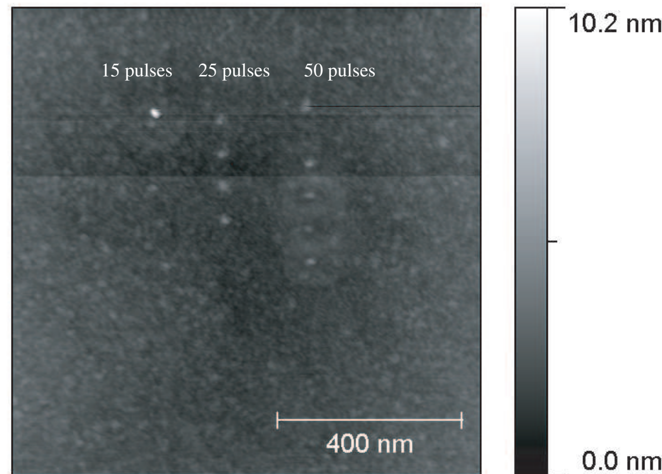

Figure 4.24: Subsequent depositions on the same sample after removal to air and reintroduction (new coated tip) with a lifting bias of 3V, which is typically very close to the surface and the threshold for a catastrophic tip failure.

both width and height, from 19±2 by 7.5±0.2 nm, to 15±2 by 2.8±0.4 nm, 12±1 by 2.0 ± 0.1 nm. The lift height for both the initial event, the left most deposit, and the subsequent events, was approximately 3V, which is typically close to the bias which causes the tip to crash into or make contact with the surface. As well the clusters are slightly asymmetric, and the speed at which the tip material runs out suggests that the tip is not replenished. No further depositions were observed after this point.

Other InP samples had varying degrees of success. One particularly interesting case involves an InP sample with a 30 nm buffer layer that was to be used for low temperature experiments. Several tips were used to deposit a series of dots on the sample surface, in each case the tip did little or nothing until within several nanometers of the surface, followed by a large current pulse, somewhat more irregular than that previously shown. After this, the tips would deposit at slightly higher lift heights, which is expected for tips with a sharp protrusion after the initial surface changes. What was of interest here was that the images taken after every deposition showed significant multiple tips, manifesting as extra dots in the sample image, later images taken with a good tip showed these were in fact single depositions as expected[1]. The

[1]Tip positions during deposition were carefully recorded with the SEM at the approach point and used to reposition later tips to within several micrometers. The gold clusters themselves are too small to be visible by this SEM and lack contrast on the insulating surface

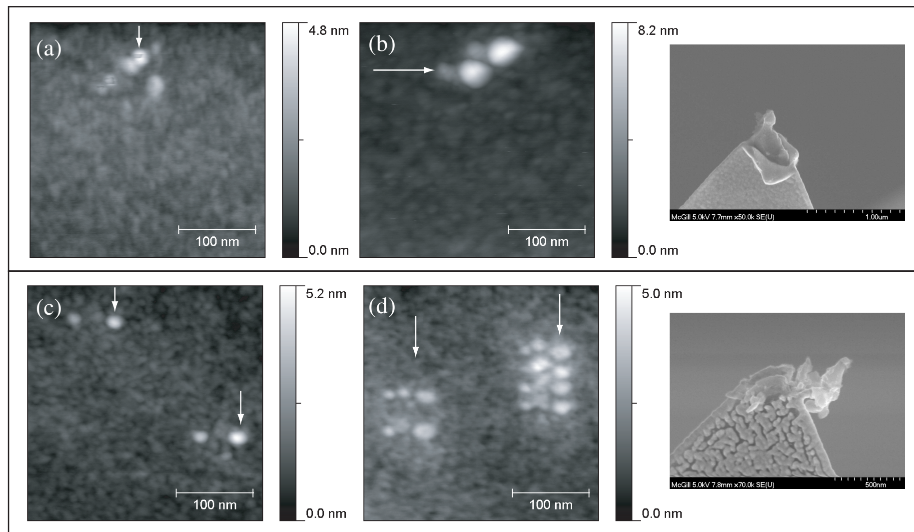

Figure 4.25: Deposited structures imaged used two strong multi-tips, arrows give the actual direction of deposition (for multiple dots). The post deposition tip images are shown to the right in each case.

reason for these multiple tip artifacts was the tip structure, after the initial pulses the tip apex was badly damaged, with the gold film badly damaged as shown in Fig 4.25 along with the deposited structures. Despite this damage the tips were quite capable of depositing on the surface, similar to imaging with STM the very apex structures of even a very ragged tip are capable of imaging the surface and in this case depositing metal, a number of dots and small collections of dots. This seems a clear indication that the critical part of the tip deposition process is the fine apex structure near the surface.

The InP samples demonstrated the ability to deposit clear structures on the surface, that the tip sample separation is typical of that expected for the thresholds calculated previously, and that the electronics and methods work largely as expected. The main difficulties are finding a way to quantify the tip apex, what is still needed is a way to estimate the precise size of the tip protrusion, if any, and a way to control the migration of material to the tip more effectively.

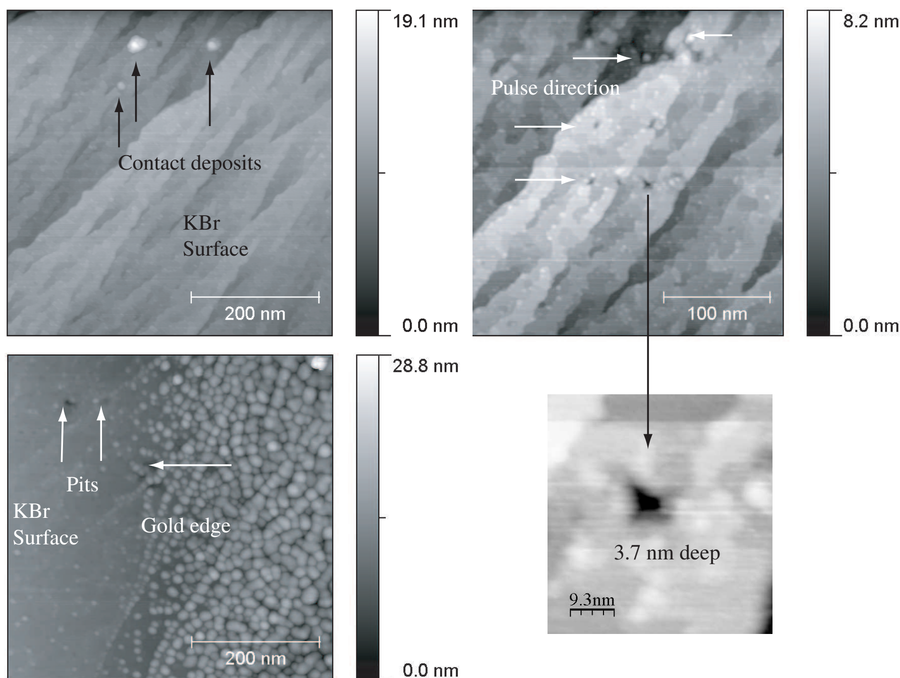

Figure 4.26: Deposited clusters and pits over 2 different KBr samples. Arrows indicate either pit, cluster, or direction of the pulse sequence (rows of 4 or 5 horizontal pulse sequences) where indicated. (top) KBr120, initial deposits, 3 in total, and the subsequent attempts are shown, the tip lift bias was 2V for the initial clusters and as low as 1.5 V for the pits, (bottom) similar uncontrolled pits on KBr118 with no deposition apparent

4.5.2 KBr surface

Samples for deposition at the edge of a metallic film or on bulk KBr are prepared using the method described in Chapter 2. A number of attempts were made to deposit on the KBr directly or near the metallic edge using the methods described in previous sections. Some of the observed depositions will be discussed and the challenges in depositing gold in this geometry. First, depositions on the bulk KBr surface will be examined, those more than a few hundred nm from the electrode edge. After this the depositions taking place either at the very edge of metal pads or over the metal surface itself will be discussed.

Deposition using electric field ionization on a bulk KBr surface seems unlikely given that the electric field and potential drop is usually generated between the tip and a

counter-electrode. Nevertheless, as has been shown in the electrostatic models given above, even some finite distance from the KBr surface the field will change sharply at the surface interface. This is not entirely surprising, conventional FIM experiments are done without a surface nearby, as the tip is far away from a counter electrode it requires kilovolt potentials for desorption to occur. The sharp change in dielectric constant at the insulating surface as well as the sharp metallic tip means that there is a non-negligible potential variation at the surface itself, making deposition a possibility but by no means guaranteed. Several attempts to deposit in this way did in fact produce a small series of dots, but only at lifting biases of less than 3 nm, and immediately followed by the creation of small holes in the surface. This suggests that in fact field desorption is not the mechanism here, but rather direct contact with the surface. It is also possible to create pits through the diffusion of charge centers in the bulk but the observed pits in this case were not rectangular and showed clear signs of mounding nearby, suggesting an indentation mechanism. The effect of a large bias is likely to cause sufficient deflection of the cantilever to create these clusters by just touching the surface, but without mass flow of gold atoms to the apex of the tip the effect is short lived, with subsequent attempts pressing the tip into the surface and creating small pyramidal holes. Examples of both the deposition and pit creation are shown in Fig 4.26.

From both samples shown in Fig 4.26 as well as other depositions it is clear that while it is possible to create gold clusters on the surface, the tip life is relatively short. After several clusters either the apex is depleted of available gold or coated in another material which increases the difficulty of the desorption process. The size of the deposited clusters from this contact process is comparable with the average tip size of the apex point on the tip, typically 50-60 nm. What this also demonstrates is that it is readily possible to create small pits in a controlled fashion, smaller even than typical indentations performed with force-distance spectroscopy. As the KBr surface is quite soft, it gives one the ability to form holes in another fashion for molecule traps, to remove extra electrodes, or shape electrodes existing on the surface.

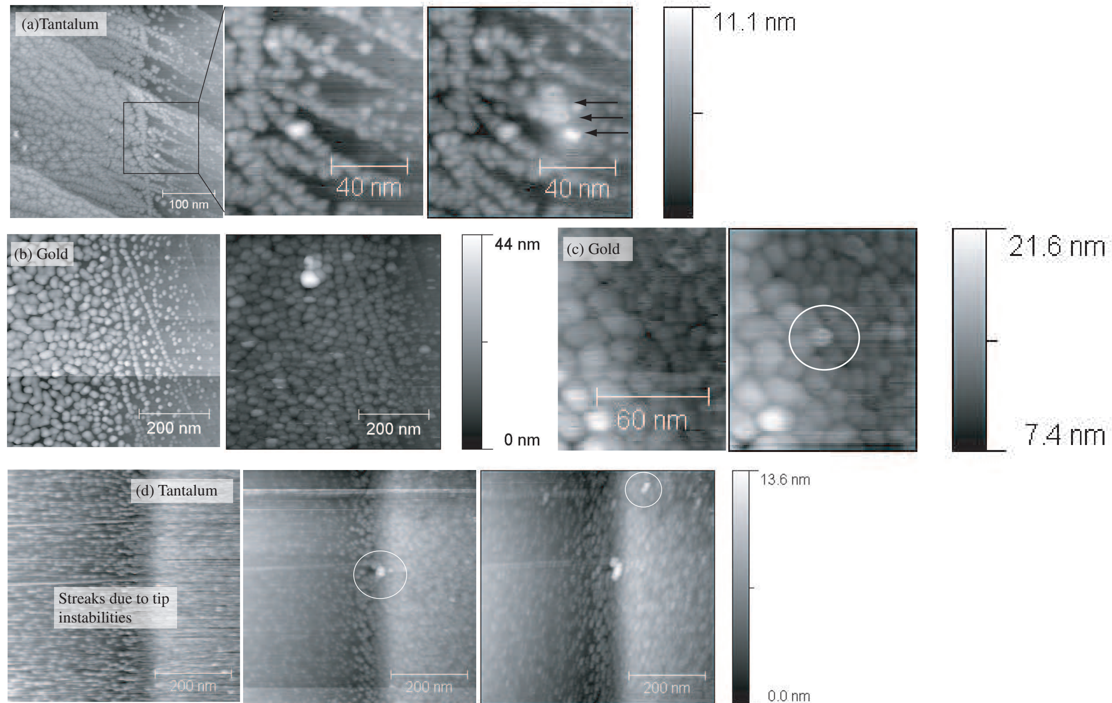

Figure 4.27: Gold clusters deposited near the metal film edge or directly over the metal itself (a) 3 depositions near the Tantalum edge, (b) Large deposition over the gold edge, (c) Small deposition on the edge of the gold film, gold also to the right but in a disconnected film, (d) Two separate depositions over a Tantalum film edge, after both the first and second deposition there is a noticeable change in the tip quality, initially improved as demonstrated by the increased stability (reduced streaks) and then worsened with a clear double tip

4.5.3 Metal electrodes

In order to use this technique to create connected metallic electrodes for transport measurements it is necessary not only to deposit on the fully insulating surface but adjacent to it and onto the nearby gold. As the previous sections have shown, it is possible to deposit on thin film or bulk insulators depending on the electrode geometry in vacuum with this technique. Modeling demonstrated the feasibility of this approach near metal film electrodes as well, in this section the experimental feasibility of this approach will be explored

Several representative deposition events are shown in Fig 4.27, over the metal film

itself and on the KBr nearby. In most cases the depositions were not repeated due to subsequent tip crashes in these regions, after depositing the increase in tip sharpness caused a significant change in the deposition threshold (+2-3V lift bias or 10-20 nm z-piezo retraction distance). Over metal electrodes this is much more sensitive than the previous insulating case. This increase in the effective applied potential due to a small protrusion in an otherwise spherical tip apex has been examined previously [113], and is consistent with previous observations. Gold films, as previously observed, have a large halo of partially connected islands between the bulk KBr and the bulk film. Tantalum films have a much sharper electrically connected edge in contrast to this. Deposition results also confirm this, with deposition attempts near the periphery of connected gold films less likely to occur. However, when the demarcation between the bulk gold film and the edge islands is known it is possible to deposit in a connective fashion to this region, as a means of both sharpening the tip and building a wire out of the bulk, Fig 4.27(b,c).

A common problem in the deposition of these clusters over metal edges is the stability of the deposit, during imaging immediately following deposition there are frequently a tip jumps over the deposition area, this is usually indicative of the tip picking up or putting down an adsorbate. In order to preserve the metal structures, for example the tantalum wires, the tip would typically be tested near either the gold edge or an unconnected tantalum wire to attempt to provoke an initial deposition event without destroying the tip and wire.

Deposition over the KBr edge but relatively close to the gold or tantalum edge was also attempted. Desorption of gold atoms under these conditions proved to be the most difficult scenario for two reasons, the field thresholds appear to be on the edge of what is possible for this cantilever geometry and electronics, and the proximity of the metal film boundary means that even a slight contact with the surface will result in a large current, destroying both tip and surface. The maximum pulse voltage currently possible is approximately 40 V, which can create significant tip-sample forces with tip sample distances of less than 5-10 nm. Two examples are shown in Fig 4.27(a,d). In proximity to the gold edge this was never successfully observed because of the large gold edge halo (thus making it difficult to deposit close to a connected metal but on KBr itself), though this can be avoided as discussed above. The advantage of beginning deposition over the metallic edge lies in the smaller voltage threshold and

larger lift heights potentially available.

Deposition on top of, or adjacent to, the edge of the gold or tantalum films on top of KBr is considerably easier, but at the same time presents different problems. Even a slight contact between tip and surface with a large applied voltage is sufficient to cause a massive pulse event. These pulses can create holes in the film micrometers in size, and in the case of the deposited tantalum wires can even fracture the wire itself. The process is of course damaging to the tip, though the exact failure mechanism is unknown. This type of crash is found to occur generally for lifting biases of under 3V or <5 nm lift height depending on the tip geometry.

These pulse events are clearly visible even on the SEM at low resolution, as shown in Fig 4.28. The damaged area can range from less than 100 nm to 4 μm across and are more common over the Ta wire edge than the gold film. In two cases shown, Fig 4.28(c,d), the tantalum wire breaks micrometers from the crash site during this pulse event, in a similar fashion to the electromigration samples discussed earlier. Given the applied voltage and resistance this is possible though the current should be lower, with a 1MΩ resistor and 40V potential one would expect at most 40 μA DC.

As the preparation of each sample with the two stage mask process takes at a minimum 4-5 days, it becomes impractical to continue testing this approach in this method, particularly given the presence of other difficulties given by the stencil deposition, contacts, sample cleaving, and other factors. With all factors taken into account, the success rate of the process becomes very low. As a result, different approaches are being examined at this point, including thin insulating films deposited in-situ such as MgO on iron.

4.6 Discussion

The preparation and use of multiple types of gold atomic force microscopy tips has been discussed in this chapter, as well as deposition results in several different geometries. Flat InP samples with a thin insulator and back-side metallic counter-electrode proved to be the most effective surface for deposition results in general, with a well defined geometry and readily imaged surface. Insulating KBr samples with metallic

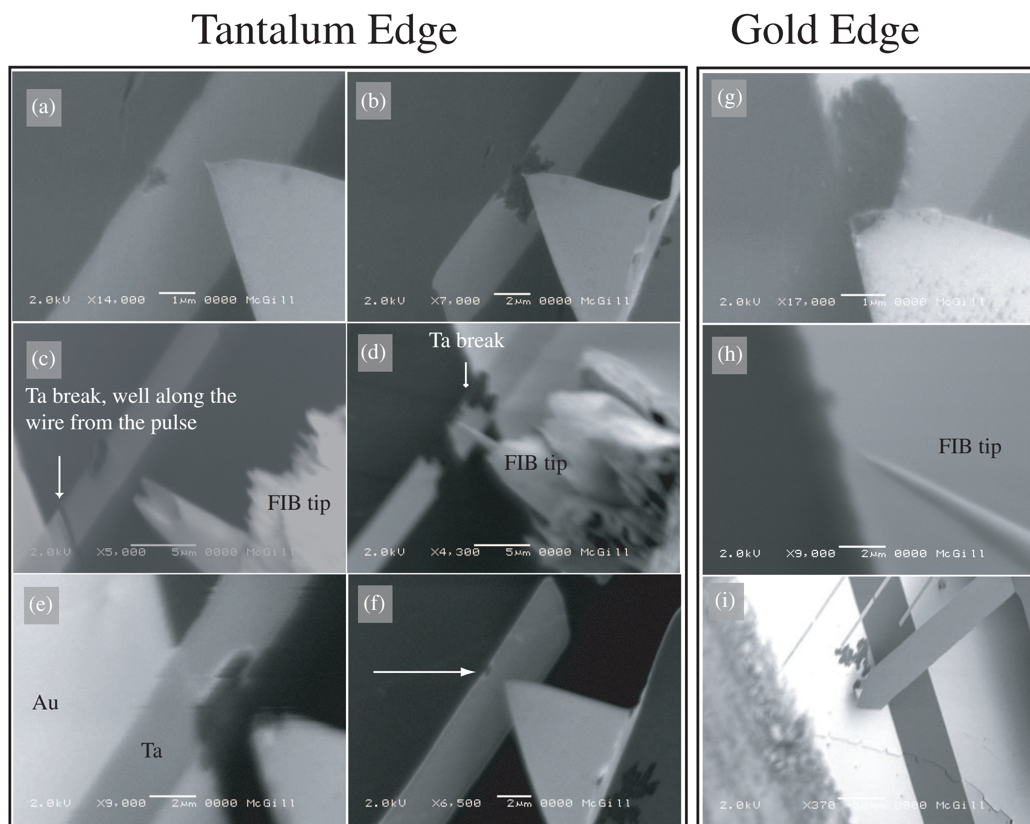

Figure 4.28: Major pulse events visible by SEM, (a-f) events over tantalum wires, (g-i) events over the gold film edge, in both (g) and (e) there is visible damage to the tip apex itself with the gold fully peeled away. In both metals the pulse event can range from sharpening the tip to fully destroying it.

films were also used to demonstrate the feasibility of this approach, with metallic clusters deposited near the electrode edge or on the KBr surface as well, with the tip in light contact with the surface. Modeling results also support the possibility of depositing directly from a metal pad in a continuous fashion though a more robust system would help to continue this process.

An attempt to lower the barrier heights through the preparation of sharper tips by FIB or electrochemical etching showed minimal differences in the deposition potential compared to coated gold tips. The most notable difference between the two was the ability of the tip to survive significant electrical crashes where a typical gold tip could have the entire coating removed. This is balanced by the significantly increases preparation time, and fragility of the etched tips during approach. The effect of a sharp apex was noticeable with gold coated tips with a clear facet at the tip apex, an area of further research.

Some challenges of the deposition process such as the tip sample forces on the cantilever were also addressed, both through the use of machined or etched tips with a long and narrow shank that may prevent excessive electrostatic forces and may prevent tip crashes at higher voltages, or by a combination of lower voltages and careful tip sample distance control.

Chapter 5

Conclusions and outlook

The fabrication of junctions suitable for molecular electronics measurements is a multi-scale process, particularly in ultra high vacuum. In the preceding chapters the preparation of these gaps by three distinct but potentially related methods has been discussed. Each of these approaches has strengths and weaknesses, all of which will be dicussed in the context of the overall goal.

Nanostencils fabricated using micromachined silicon membranes with reinforced mechanical openings have been demonstrated as capable of readily depositing features on the order of 100 nm. The stencil approach mechanism, using parallel piezo elements in a slip-stick walker with an adjustable mask mount, is capable of approaching masks repeatably to within several micrometers of a cleaved KBr sample face over several millimeters. As a result the spreading of evaporated material is limited to $\approx$ 100 nm. Further improvements of this should be possible by machining the staircase openings of the silicon stencil from the opposite side, reducing the sample-stencil spacing by up to 2 μm, which will reduce the feature broadening by approximately 50 nm. This should achieve a deposited wire width of 50-100 nm from an original stencil opening of 50 nm, while stencil depositions have been reported in the literature smaller than this it will be unlikely in this geometry as cleaved samples typically have small imperfections and steps which limit the mask proximity to within several micrometers.

Electromigration results on the deposited wires have demonstrated the formation of

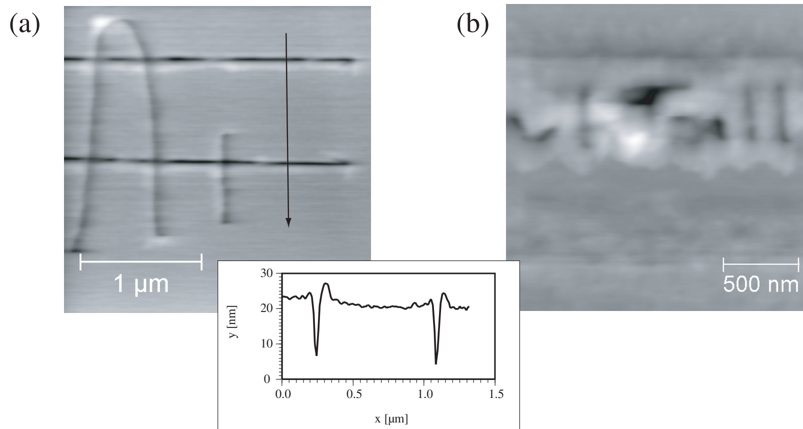

Figure 5.1: Gold and tantalum films (a and b respectively) indented using the lithography mode, JEOL WinSPM software. Inset: line profile, deposited gold film 35 nm thick

both subnanometer size gaps as well as significantly larger 10-100 nm gaps suitable for post migration deposition, as discussed in Chapter 4. Of the materials examined, gold is clearly the most suitable with clear signs of electromigration and a large grain size which is suitable for the creation of the larger gaps under slightly stressed migration conditions. One of the major drawbacks to the electromigration process on deposited wires in UHV is the need to move the sample from one position to another with uncertain electrical characteristics between the two pads at times. A proposed solution to this would be the creation of additional dummy wires in parallel with the nanometer scale ones to act as a current shunt if necessary. These wires could be removed prior to electromigration by mechanically scratching with the AFM tip, similar to Fig 5.1, which takes advantage of the inherently soft film and KBr substrate. Alternatively, parallel electromigration has been demonstrated by D. Johnston et al [120], and may be an alternative method to remove extra parallel beams in a controlled fashion. However, in order to offer sufficient ESD protection the additional beams would be required to have a significantly larger thickness, such that balancing the power load for electromigration would be difficult.

The gaps created using electromigration have been demonstrated to range significantly in size (sub-nanometer to micrometers), but as long as they are larger than some tunneling distance, typically 1 nm, they provide an effective break in the wire conductance. Even in the event that such a gap is too small for additional deposition or single molecules, using the field assisted deposition technique it will be possible to

bridge around the gap with a smaller electrically connected wire.

The field assisted deposition techniques described in the preceding chapter have been demonstrated in several different geometries, over InP substrates to demonstrate feasibility and explore the deposition parameters, over deposited metal films, and even (at first sight surprisingly) over the bulk insulating surface. This is the first time that field assisted deposition on a highly insulating substrate such as KBr has been demonstrated. In all cases the deposition process is possible with slightly different mechanisms. Over the bulk KBr the process appears to be possible at sufficiently high fields but in these particular conditions the required fields are sufficiently high as to cause a light contact between tip and substrate and force deposition in a contact mode.

From the results shown one can draw general conclusions about the deposition process. The formation of a sharp apex point on the tip is crucial, but requires the tip in close and dangerous proximity to the surface initially. With sufficiently long pulses this can lead to a risk of tip crashes quite quickly. The proposed solution lies in depositing with much shorter pulses but in greater number, to maintain the overall deposition time, allowing the tip atoms sufficient time under high field conditions to sharpen but without a catastrophic crash. The present limitation of this effect is the capacitance of the tip voltage feed through, however with a minimal series resistance to the tip, 1 MΩ or less, the pulse time constant will be limited to 10 μs, faster than the mechanical response time of the cantilever. There is some evidence that a larger series of pulses is more effective in shaping the tip so long as a crash is avoided. Similarly, significantly stiffer cantilevers such as those used in the Q-plus configuration with k = 1800 N/m [13] would be helpful in maintaining the tip sample distance at larger pulse heights.

Alternatively, one may envisage a lowering of the tip sample barrier by actively heating the tip or sample during deposition either directly through the stage or radiatively by heating the tip alone through the external viewport. This may also be accomplished through the use of the SEM, in a fashion similar to that discussed for locally enhancing the electromigrative process, both being thermally limited.

The use of the gap created during electromigration poses one other readily solvable problem, the previously discussed metal islands often left behind by this process. It

should be readily possible by reverse bias of the AFM tip to remove such defects from the gap and provide a clean base for the subsequent deposition process.

Considering all the preceding techniques together, it is clear that they offer a novel potential path to molecular measurements. The overall success rate of each stage after considering the limiting stages of each process is relatively low though the success rate of each stage of sample preparation is generally over 50%, encompassing but not limited to: stencil alignment with pre-existing electrodes, ESD prior to electromigration, inability to field deposit from a given tip, or tip or sample failure during the current pulse due to an excessively large pulse due to contact. Several of the suggestions discussed above can readily alleviate some of these difficulties, and further work is planned on this system using a thin film of magnesium oxide on single crystal iron whiskers. With a steady back electrode there is the possibility of a more uniform potential distribution for deposition, similar to that of the InP system.

Bibliography

[1] C. Durkan. *Current at the nanoscale: an introduction to nanoelectronics*. Imperial College Press, 2007.

[2] J.E. Sanchez Jr, Oliver Kraft, and Eduard Arzt. Electromigration induced transgranular slit failures in near bamboo Al and Al-2% Cu thin-film interconnects. *Applied Physics Letters*, 61(26):3121, 1992.

[3] C Durkan, M. Schneider, and M. Welland. Analysis of failure mechanisms in electrically stressed Au nanowires. *Journal of Applied Physics*, 86(1-4):1280, February 1999.

[4] R.C. Weast and Chemical Rubber Company. *CRC handbook of chemistry and physics*. CRC press Boca Raton, FL.

[5] S. Fostner, S.A. Burke, J. Topple, J. Mativetsky, J. Beerens, and P. Grütter. Silicon nanostencils with integrated support structures. *Microelectronic Engineering*, 87(4):652–657, 2009.

[6] J. Mativetsky, G. Pace, M. Elbing, M.A. Rampi, M. Mayor, and P. Samorì. Azobenzenes as Light-Controlled Molecular Electronic Switches in Nanoscale Metal- Molecule- Metal Junctions. *J. Am. Chem. Soc*, 130(29):9192–9193, 2008.

[7] O. Shaya, M. Shaked, Y. Usherenko, E. Halpern, G. Shalev, A. Doron, I. Levy, and Y. Rosenwaks. Tracing the Mechanism of Molecular Gated Transistors. *The Journal of Physical Chemistry C*, 113(15):6163–6168, April 2009.

[8] MA Reed, C. Zhou, CJ Muller, TP Burgin, and JM Tour. Conductance of a molecular junction. *Science*, 278(5336):252, 1997.

[9] Hyunwook Song, Youngsang Kim, Yun Hee Jang, Heejun Jeong, Mark A Reed, and Takhee Lee. Observation of molecular orbital gating. *Nature*, 462(7276):1039–43, 2009.

[10] J. Nara. Theoretical investigation of contact effects in conductance of single organic molecule. *Thin Solid Films*, 438-439:221–224, 2003.

[11] Shawn Fostner. Development of metallic electrodes on potassium bromide. Master's thesis, McGill University, 2006.

[12] G. Binnig, C.F. Quate, and C. Gerber. Atomic force microscope. *Physical review letters*, 56(9):930–933, 1986.

[13] S. Morita, R. Wiesendanger, and E. Meyer. *Noncontact atomic force microscopy*. Springer Berlin, 2002.

[14] R García. Dynamic atomic force microscopy methods. *Surface Science Reports*, 47(6-8):197–301, September 2002.

[15] TR Albrecht, P. Grütter, D. Horne, and D. Rugar. Frequency modulation detection using high-Q cantilevers for enhanced force microscope sensitivity. *J. Appl. Phys*, 69(September 1990):668–673, 1991.

[16] F. Giessibl. A direct method to calculate tipsample forces from frequency shifts in frequency-modulation atomic force microscopy. *Applied Physics Letters*, 78(1):123, 2001.

[17] S.A. Burke and P. Grütter. Comment on: Temperature dependence of the energy dissipation in dynamic force microscopy. *Nanotechnology*, 19:398001, 2008.

[18] T Sulchek, R Hsieh, J D Adams, G G Yaralioglu, S C Minne, C F Quate, J P Cleveland, A Atalar, and D M Adderton. High-speed tapping mode imaging with active Q control for atomic force microscopy. *Applied Physics Letters*, 76(11):1473, 2000.

[19] R. García and A. San Paulo. Dynamics of a vibrating tip near or in intermittent contact with a surface. *Physical Review B*, 61(20):R13381–R13384, May 2000.

[20] J. Aimé, R. Boisgard, L. Nony, and G. Couturier. Nonlinear Dynamic Behavior of an Oscillating Tip-Microlever System and Contrast at the Atomic Scale. *Physical Review Letters*, 82(17):3388–3391, April 1999.

[21] L. Nony, R. Boisgard, and J. P. Aime. Nonlinear dynamical properties of an oscillating tipcantilever system in the tapping mode. *The Journal of Chemical Physics*, 111(4):1615, 1999.

[22] R. Dianoux, F. Martins, F. Marchi, C. Alandi, F. Comin, and J. Chevrier. Detection of electrostatic forces with an atomic force microscope: Analytical and experimental dynamic force curves in the nonlinear regime. *Physical Review B*, 68(4):1–6, July 2003.

[23] J. Mativetsky. *Understanding and controlling the growth of metals and molecules on an insulating surface*. PhD thesis, McGill University, 2006.

[24] Sarah A. Burke. Buckminsterfullerene on KBr studied by High Resolution NC-AFM: Molecular nucleation and growth on an insulator. Master's thesis, McGill University, 2004.

[25] S.A. Burke. *Building foundations for molecular electronics: growth of organic molecules on alkali halides as prototypical insulating substrates*. PhD thesis, McGill University, 2009.

[26] L. Reimer. *Scanning electron microscopy: physics of image formation and microanalysis*. Springer Verlag, 1998.

[27] J. Mativetsky, Yoichi Miyahara, S. Fostner, S.A. Burke, and P. Grütter. Use of an electron-beam evaporator for the creation of nanostructured pits in an insulating surface. *Applied Physics Letters*, 88(23):233121, 2006.

[28] J. Mativetsky, S.A. Burke, S. Fostner, and P. Grütter. Nanoscale Pits as Templates for Building a Molecular Device. *Small*, 3(5):818–821, May 2007.

[29] S. Datta. *Electronic transport in mesoscopic systems*. Cambridge Univ Press, 1997.

[30] N. Ashcroft and D. Mermin. *Solid state physics*. Harcourt, 2002.

[31] K. Fuchs. The conductivity of thin metallic films according to the electron theory of metals. *Mathematical Proceedings of the Cambridge*, 157(1936):100–108, 2008.

[32] E. H. Sondheimer. The mean free path of electrons in metals. *Advances in Physics*, 50(6):499–537, September 2001.

[33] AF Mayadas and M. Shatzkes. Electrical-resistivity model for polycrystalline films: the case of arbitrary reflection at external surfaces. *Physical review B*, 1(4):1382–1389, 1970.

[34] C. Durkan and M. Welland. Size effects in the electrical resistivity of polycrystalline nanowires. *Physical Review B*, 61(20):14215–14218, May 2000.

[35] MC Salvadori, AR Vaz, RJC Farias, and M. Cattani. Electrical Resistivity of Nanostructured Platinum and Gold Thin Films. *Surface Review and Letters*, 11(2):223–227, 2004.

[36] YV Sharvin and NI Bogatina. Investigation of Focusing of Electron Beams in a Metal by a Longitudinal Magnetic Field. *Soviet Journal of Experimental and Theoretical Physics*, 29:419, 1969.

[37] BJ Van Wees, H. Van Houten, CWJ Beenakker, JG Williamson, LP Kouwenhoven, D. Van Der Marel, and CT Foxon. Quantized conductance of point contacts in a two-dimensional electron gas. *Physical Review Letters*, 60(9):848–850, 1988.

[38] D. Strachan, D. Johnston, B. Guiton, S. Datta, P. Davies, D. Bonnell, and A.T. Johnson. Real-Time TEM Imaging of the Formation of Crystalline Nanoscale Gaps. *Physical Review Letters*, 100(5):1–4, 2008.

[39] H. Ohnishi, Y. Kondo, and K. Takayanagi. Quantized conductance through individual rows of suspended gold atoms. *Nature*, 395(October):2–5, 1998.

[40] A. Linklater and J. Nogami. Defining nanoscale metal features on an atomically clean silicon surface with a stencil. *Nanotechnology*, 19(28):285302–285302, 2008.

[41] J. Mativetsky, S. Fostner, S.A. Burke, and P. Grütter. High-resolution investigation of metal nanoparticle growth on an insulating surface. *Physical Review B*, 80(4):45430, 2009.

[42] MG Cattania, V. Penka, RJ Behm, K. Christmann, and G. Ertl. Interaction of hydrogen with a palladium (110) surface. *Surface Science*, 126(1-3):382–391, 1983.

[43] A.A. Tseng. Recent developments in nanofabrication using ion projection lithography. *Small*, 1(6):594–608, June 2005.

[44] Mandar M. Deshmukh, D. C. Ralph, M. Thomas, and J. Silcox. Nanofabrication using a stencil mask. *Applied Physics Letters*, 75(11):1631, 1999.

[45] J Brugger, JW Berenschot, S Kuiper, W Nijdam, B Otter, and M Elwenspoek. Resistless patterning of sub-micron structures by evaporation through nanostencils. *Microelectronic engineering*, 53(1-4):403–405, 2000.

[46] C. Gärtner, R. Hoffman, F. Pérez-Willard, M. Sauter, C. Sürgers, and H. Löhneysen. Fully ultrahigh-vacuum-compatible fabrication of submicrometer-spaced electrical contacts. *Review of Scientific Instruments*, 77:026101, 2006.

[47] GM Kim, MAF Van Den Boogaart, and J. Brugger. Fabrication and application of a full wafer size micro/nanostencil for multiple length-scale surface patterning. *Microelectronic engineering*, 67:609–614, June 2003.

[48] J Köhler, M. Albrecht, CR Musil, and E. Bucher. Direct growth of nanostructures by deposition through an Si3N4 shadow mask. *Physica E Low-Dimensional Systems and Nanostructures*, 4(3):196–200, July 1999.

[49] V. Blech, T. Nobuyuki, and B. Kim. Nanostenciling through a cm[sup 2]-wide silicon membrane. *Journal of Vacuum Science & Technology B: Microelectronics and Nanometer Structures*, 24(1):55, 2006.

[50] R. Luthi, R. Schlittler, J. Brugger, P. Vettiger, M. Welland, and J. Gimzewski. Parallel nanodevice fabrication using a combination of shadow mask and scanning probe methods. *Applied Physics Letters*, 75(9):1314, 1999.

[51] H. Guo, D. Martrou, T. Zambelli, J. Polesel-Maris, A. Piednoir, E. Dujardin, S. Gauthier, M.A.F. van Den Boogaart, L.M. Doeswijk, and J. Brugger. Nanostenciling for fabrication and interconnection of nanopatterns and microelectrodes. *Applied Physics Letters*, 90:093113, 2007.

[52] S. Egger, A. Ilie, Y. Fu, J. Chongsathien, D.J. Kang, and M.E. Welland. Dynamic shadow mask technique: A universal tool for nanoscience. *Nano letters*, 5(1):15–20, 2005.

[53] P. Zahl, M. Bammerlin, G. Meyer, and R. Schlittler. All-in-one static and dynamic nanostencil atomic force microscopy/scanning tunneling microscopy system. *Review of Scientific Instruments*, 76(2):023707, 2005.

[54] L. Didenko, J. Melngailis, H. Loschner, G. Stengl, A. Chalupka, and A. Shimkunas. Analysis of stencil mask distortion in ion projection lithography. *Microelectronic Engineering*, 35(1):443–446, 1997.

[55] Zhengwei Pan, Sheng Dai, David B. Beach, and Douglas H. Lowndes. Temperature Dependence of Morphologies of Aligned Silicon Oxide Nanowire Assemblies Catalyzed by Molten Gallium. *Nano Letters*, 3(9):1279–1284, September 2003.

[56] M. Asheghi, YK Leung, SS Wong, and KE Goodson. Phonon-boundary scattering in thin silicon layers. *Applied Physics Letters*, 71(September):1798, 1997.

[57] M.J. Madou. *Fundamentals of microfabrication: the science of miniaturization*. CRC, 1997.

[58] G. Guisbiers, O. Overschelde, M. Wautelet, Ph Leclère, and R. Lazzaroni. Fractal dimension, growth mode and residual stress of metal thin films. *Journal of Physics D: Applied Physics*, 40(4):1077–1079, February 2007.

[59] GG Stoney. The tension of metallic films deposited by electrolysis. *Proceedings of the Royal Society of London. Series A,*, 82(553):172–175, 1909.

[60] WA Brantley. Calculated elastic constants for stress problems associated with semiconductor devices. *Journal of Applied Physics*, 44:534, 1973.

[61] C.A. Klein. How accurate are Stoneys equation and recent modifications. *Journal of Applied Physics*, 88(9):5487, 2000.

[62] R. Knepper and S. Baker. Coefficient of thermal expansion and biaxial elastic modulus of β phase tantalum thin films. *Applied Physics Letters*, 90(18):181908, 2007.

[63] M. Lishchynska, V. Bourenkov, L. Doeswijk, J. Brugger, and J. Greer. Predicting mask distortion, clogging and pattern transfer for stencil lithography. *Microelectronic Engineering*, 84:42–53, 2007.

[64] MAF van den Boogaart, LM Doeswijk, J. Brugger, and E.P.F. de Lausanne. Silicon-supported membranes for improved large-area and high-density micro/nanostencil lithography. *Microelectromechanical Systems, Journal of*, 15(6):1663–1670, 2006.

[65] O Vazquez-Mena, LG Villanueva, V Savu, K Sidler, P Langlet, and J Brugger. Analysis of the blurring in stencil lithography. *Nanotechnology*, 20:415303, 2009.

[66] J.R. Black. Electromigration failure modes in aluminum metallization for semiconductor devices. *Proceedings of the IEEE*, 57(9):1587–1594, 1969.

[67] H. Park, A.K.L. Lim, A.P. Alivisatos, J Park, and P.L. McEuen. Fabrication of metallic electrodes with nanometer separation by electromigration. *Applied Physics Letters*, 75:301, 1999.

[68] F. O. Hadeed and C. Durkan. Controlled fabrication of 12 nm nanogaps by electromigration in gold and gold-palladium nanowires. *Applied Physics Letters*, 91(12):123120, 2007.

[69] J. Baik, S. Lee, and M. Moskovits. Polarized surface-enhanced Raman spectroscopy from molecules adsorbed in nano-gaps produced by electromigration in silver nanowires. *Nano letters*, 9(2):672–6, March 2009.

[70] M F Lambert, M F Goffman, J P Bourgoin, and P Hesto. Fabrication and characterization of sub-3 nm gaps for single-cluster and single-molecule experiments. *Nanotechnology*, 14(7):772–777, July 2003.

[71] A. Scorzoni, B. Neri, C. Caprile, and F. Fantini. Electromigration in thin-film interconnection lines: models, methods and results. *Materials Science Reports*, 7(4-5):143–220, December 1991.

[72] I. A. Blech. Electromigration in thin aluminum films on titanium nitride. *Journal of Applied Physics*, 47(4):1203, 1976.

[73] Y. Golan, L. Margulis, S. Matlis, and I. Rubinstein. Vacuum-Deposited Gold Films. *Journal of the Electrochemical Society*, 142:1629, 1995.

[74] B. Stahlmecke and G Dumpich. Resistance behaviour and morphological changes during electromigration in gold wires. *Journal of Physics: Condensed Matter*, 19(4):046210, January 2007.

[75] D. R. Fridline and A. Bower. Influence of anisotropic surface diffusivity on electromigration induced void migration and evolution. *Journal of Applied Physics*, 85(6):3168, 1999.

[76] VT Srikar and CV Thompson. Dislocation pile-ups as sites for formation of electromigration-induced transgranular slit-like voids in Al interconnects. *Scripta materialia*, 42(1):97–102, December 1999.

[77] M.R. Gungor and D. Maroudas. Electromigration-induced failure of metallic thin films due to transgranular void propagation. *Applied Physics Letters*, 72(26):3452, 1998.

[78] E. Arzt, O. Kraft, WD Nix, and JE Sanchez. Electromigration failure by shape change of voids in bamboo lines. *Journal of Applied Physics*, 76(3):1563–1571, 1994.

[79] T. Taychatanapat, K. Bolotin, F. Kuemmeth, and D. Ralph. Imaging electromigration during the formation of break junctions. *Nano letters*, 7(3):652–6, March 2007.

[80] R. Sordan, K. Balasubramanian, M. Burghard, and K. Kern. Coulomb blockade phenomena in electromigration break junctions. *Applied Physics Letters*, 87:013106, 2005.

[81] G. Esen and M. S. Fuhrer. Temperature control of electromigration to form gold nanogap junctions. *Applied Physics Letters*, 87(26):263101, 2005.

[82] M. L. Trouwborst, S. J. van der Molen, and B. J. van Wees. The role of Joule heating in the formation of nanogaps by electromigration. *Journal of Applied Physics*, 99(11):114316, 2006.

[83] D. Strachan, DE Smith, DE Johnston, T.H. Park, M.J. Therien, DA Bonnell, and AT Johnson. Controlled fabrication of nanogaps in ambient environment for molecular electronics. *Applied Physics Letters*, 86:043109, 2005.

[84] A. Mahapatro, S. Ghosh, and D.B. Janes. Nanometer scale electrode separation (nanogap) using electromigration at room temperature. *IEEE Transactions On Nanotechnology*, 5(3):232–236, May 2006.

[85] C. Durkan and M. Welland. Analysis of failure mechanisms in electrically stressed gold nanowires. *Ultramicroscopy*, 82(1-4):125–33, February 2000.

[86] M. Kaspers, A. Bernhart, F-J Meyer Zu Heringdorf, G. Dumpich, and R. Möller. Electromigration and potentiometry measurements of single-crystalline Ag nanowires under UHV conditions. *Journal of Physics: Condensed Matter*, 21(26):265601, July 2009.

[87] VM Koleshko and IV Kiryushin. Electromigration threshold of thin-film conductors. *Thin Solid Films*, 192:181–191, 1990.

[88] B. Stahlmecke and G. Dumpich. Influence of the electron beam on electromigration measurements within a scanning electron microscope. *Applied Physics Letters*, 90(4):043517, 2007.

[89] A. Houck, J. Labaziewicz, E. Chan, J. Folk, and I. Chuang. Kondo effect in electromigrated gold break junctions. *Nano letters*, 5(9):1685–8, September 2005.

[90] EW Müller. Field desorption. *Physical Review*, 102(3):618, 1956.

[91] R. Gomer. Field desorption. *The Journal of Chemical Physics*, 31(2):341, 1959.

[92] T.T. Tsong. On the mechanism of field evaporation. *Surface Science*, 10(1):102–117, 1968.

[93] T.T. Tsong. Effects of an electric field in atomic manipulations. *Physical Review B*, 44(24):13703–13710, 1991.

[94] NM Miskovsky and T.T. Tsong. Field evaporation of gold in single-and double-electrode systems. *Physical Review B*, 46(4):2640–2643, 1992.

[95] G. Binnig, H. Rohrer, C. Gerber, and E. Weibel. Tunneling through a controllable vacuum gap. *Applied Physics Letters*, 40(2):178, 1982.

[96] HJ Mamin, S. Chiang, H. Birk, PH Guethner, and D. Rugar. Gold deposition from a scanning tunneling microscope tip. *Journal of Vacuum Science \& Technology B: Microelectronics and Nanometer Structures*, 9:1398, 1991.

[97] HJ Mamin, PH Guethner, and D. Rugar. Atomic emission from a gold scanning-tunneling-microscope tip. *Physical review letters*, 65(19):2418–2421, 1990.

[98] G. Binnig, N. García, H. Rohrer, JM Soler, and F. Flores. Electron-metal-surface interaction potential with vacuum tunneling: Observation of the image force. *Physical Review B*, 30(8):4816–4818, 1984.

[99] S. Hosaka, H. Koyanagi, A. Kikukawa, Y. Maruyama, and R. Imura. Formation of nanometer-sized Au dots on Si substrate in air. *Journal of Vacuum Science \& Technology B: Microelectronics and Nanometer Structures*, 12:1872, 1994.

[100] L. Agbezuge. Finite Element Solution of the Poisson equation with Dirichlet Boundary Conditions in a rectangular domain. `http://www.cs.cornell.edu/Conferences/ASEE2006/ASEE%20Papers/Session%205/fea_poisson_Agbezuge.pdf`, 2006.

[101] Potassium Bromide. `http://www.korth.de/eng/503728952d091450d/503728952d0af4427.htm`, 2010.

[102] J. Colchero, A. Gil, and AM Baró. Resolution enhancement and improved data interpretation in electrostatic force microscopy. *Physical Review B*, 64(24):245403, 2001.

[103] K. Akiyama, T Eguchi, T An, Y Fujikawa, Y. Yamada-Takamura, T Sakurai, and Y Hasegawa. Development of a metaltip cantilever for noncontact atomic force microscopy. *Review of Scientific Instruments*, 76:033705, 2005.

[104] L. Cockins, Y. Miyahara, R. Stomp, and P. Grütter. High-aspect ratio metal tips attached to atomic force microscopy cantilevers with controlled angle, length, and radius for electrostatic force microscopy. *Review of Scientific*, pages 2007–2009, 2007.

[105] MJ Vasile, D. Grigg, JE Griffith, E. Fitzgerald, and PE Russell. Scanning probe tip geometry optimized for metrology by focused ion beam ion milling. *Journal of Vacuum Science \& Technology B: Microelectronics and Nanometer Structures*, 9:3569, 1991.

[106] B. Ren, G. Picardi, and B. Pettinger. Preparation of gold tips suitable for tip-enhanced Raman spectroscopy and light emission by electrochemical etching. *Review of Scientific Instruments*, 75(4):837–841, 2004.

[107] L. Eligal, F. Culfaz, V. McCaughan, N.I. Cade, and D. Richards. Etching gold tips suitable for tip-enhanced near-field optical microscopy. *Review of Scientific Instruments*, 80(January):033701, 2009.

[108] M.G. Boyle, L. Feng, and P. Dawson. Safe fabrication of sharp gold tips for light emission in scanning tunnelling microscopy. *Ultramicroscopy*, 108(6):558–566, 2008.

[109] D. Gingery and P. Bühlmann. Single-step electrochemical method for producing very sharp Au scanning tunneling microscopy tips. *The Review of scientific instruments*, 78(11):113703, 2007.

[110] T. Ito, P. Bühlmann, and Y. Umezawa. Polypyrrole-Modified Tips for Functional Group Recognition in Scanning Tunneling Microscopy. *Analytical Chemistry*, 71(9):1699–1705, May 1999.

[111] L. Libioulle, Y. Houbion, and J.M. Gilles. Very sharp gold and platinum tips to modify gold surfaces in scanning tunneling microscopy. *Journal of Vacuum Science \& Technology B: Microelectronics and Nanometer Structures*, 13(3):1325, 1995.

[112] S. Ye, C. Ishibashi, and K. Uosaki. Anisotropic Dissolution of an Au (111) Electrode in Perchloric Acid Solution Containing Chloride Anion Investigated by in Situ STMThe Important Role of Adsorbed Chloride Anion. *Langmuir*, 15(3):807–812, 1999.

[113] M.E. Pumarol-Crestar. *Gold nanodot and nanowire fabrication by Atomic Force Microscopy*. PhD thesis, McGill University, 2008.

[114] D. Fujita, Q. Jiang, and H. Nejoh. Fabrication of gold nanostructures on a vicinal Si (111) 7 x 7 surface using ultrahigh vacuum scanning tunneling microscope and a gold-coated tungsten tip. *Journal of Vacuum Science and Technology-Section B-Microelectronics Nanometer Structur*, 14(6):3413–3419, 1996.

[115] D. Fujita, Q. Jiang, Z. Dong, H. Sheng, and H. Nejoh. Nanostructure fabrication on silicon surfaces by atom transfer from a gold tip using an ultrahigh vacuum scanning tunneling microscope. *Nanotechnology*, 8:A10–A14, 1997.

[116] J.Y. Park, RJ Phaneuf, and ED Williams. Variation of threshold field in field induced fabrication of Au nanodots on ultrathin in situ grown silicon oxide. *Surface Science-Including Surface Science Letters*, 470(1):69, December 2001.

[117] H. Abed, H. Jamgotchian, H. Dallaporta, B. Gely, P. Bindzi, D. Chatain, S. Nitsche, D. Chaudanson, E. Cambril, V. Safarov, and D. Tonneau. Deposition of gold nanofeatures on silicon samples by field-induced deposition using a scanning tunneling microscope. *Journal of Vacuum Science & Technology B: Microelectronics and Nanometer Structures*, 23(4):1543, 2005.

[118] A. Houel, D. Tonneau, N. Bonnail, H. Dallaporta, and V. I. Safarov. Direct patterning of nanostructures by field-induced deposition from a scanning tunneling microscope tip. *Journal of Vacuum Science & Technology B: Microelectronics and Nanometer Structures*, 20(6):2337, 2002.

[119] HL Zhang, HL Li, and ZF Liu. Study on the delicate nanostructures formed on Au (111) by scanning tunneling microscopy (STM). *Microelectronic Engineering*, 63:381–389, 2002.

[120] D. Johnston, D. Strachan, and A. Johnson. Parallel fabrication of nanogap electrodes. *Nano letters*, 7(9):2774–7, September 2007.